ATMOSPHERIC IONIZATION BY PRECIPITATED ELECTRONS

A thesis submitted for the Degree of Master
of Science of Rhodes University

by

ANNEMARIE WULFF

April, 1972.

Acknowledgements

"A Masters thesis is but a test of endurance"!

I should like to record here my heartfelt thanks to each and every one of my friends for all their help in many different ways during the past few months.

I must thank especially Professor Gledhill who supervised the project and write-up with remarkable patience and humour.

Among my colleagues I am indebted to James Greener, Aubrey Haschick and Howard Williams for helpful discussions and assistance with computing problems. I am also grateful to Allon Poole for the permission to use a section of a computer program.

My grateful thanks also to Robin Johns without whose willing assistance in many different ways this thesis would never have been completed in the time available. Thanks also to Bevis Booth for typing and to Ray Haggard for checking the final copy.

Finally, I wish to thank the Department of Transport for financing the Rhodes University Antarctic Research Group and so enabling me to do this research.

TABLE OF CONTENTS

		Page
List of Tables		
List of Figures		
Chapter 1	Introduction	1
2	Background	3
3	The Computation of Ionization Rate Profiles	12
4	Electron Production in Different Model Atmospheres	17
5	The Effect of Different Dip Angles	25
6	Stations at Different Latitudes	27
7	Sanae - A Special Study	31
8	An Energy Spectrum of the Type $J_{>E} = J_o\ e^{-E/E_o}$	44
9	Conclusions	50
	Summary	52
	References	54
Appendix 1	Particle Fluxes by J.A. Gledhill	57
2	Average Density in a Lamination	61
3	AW 18	62
4	Program JACCHIA ATM	64
5	Program INTERATM	66
6	Program MAXHQ	67

List of Tables

Table 2-1 Rees Model Atmosphere page 9

4-1 Variation of q/F with T_{exo} in the F-region 21

6-1 h_m vs hour angle at Sanae/q_m/F vs hour angle at Sanae 34

7-2 Variation of q/F with hour of day at Sanae 35

7-3 Variation of q/F with Season in the F-region 37

7-4 Variation of q/F with $F_{10,7}$ in the F-region 39

7-5 h_m vs a_p (geomagnetic activity index) at Sanae/ q_m/F vs a_p (geomagnetic activity index) at Sanae 41

7-6 Variation of q/F with a_p in the F-region 42

8-1 $Q/\pi J_o$ Variation with T_{exo} for different E_o values 49

List of Figures

Fig. 2-1	log r_p vs log E	opposite page 10
3-1	λ_{IDH}	opposite page 15
3-2	Comparison of Results of Berger et al and AW18	following page 15
3-3	Comparison of Ionization Profiles of Rees and AW18	following page 15
4-1	Variation with T_{exo} (1 keV to 2 keV)	following page 18
4-2	" " " (5 keV)	" " 18
4-3	" " " (10 keV)	" " 18
4-4	" " " (20 keV)	" " 18
4-5	Variation of h_m with T_{exo}/Variation of q_m/F with T_{exo}	" " 19
4-6	Normalized curve for T_{exo} 900 K to 2100 K and E_i = 1, 2, 5, 10 & 20 keV	" " 24
4-7	Variation of H with T_{exo} for 1, 2, 5, 10 and 20 keV	" " 24
5-1	Variation with Dip Angle (1 and 2 keV)	" " 25
5-2	" " " " (5 keV)	" " 25
5-3	" " " " (10 keV)	" " 25
5-4	" " " " (20 keV)	" " 25
5-5	Variation of h_m with Dip Angle/Variation of q_m/F with Dip Angle	" " 25
6-1	Ionization Rate Profiles for Different Stations (1 and 2 keV)	" " 27
6-2	Ionization Rate Profiles for Different Stations (5 keV)	" " 27
6-3	Ionization Rate Profiles for Different Stations (10 keV)	" " 27
6-4	Ionization Rate Profiles for Different Stations (20 keV)	" " 27
	Figs. 1 and 4 from Cain and Neilon	opposite page 28
7-1	Variation with Hour of Day (1 and 2 keV)	following page 35
7-2	" " " " " (5 keV)	" " 35
7-3	" " " " " (10 keV)	" " 35
7-4	" " " " " (20 keV)	" " 35
7-5	Variation with Season (1 and 2 keV)	" " 37
7-6	" " " (5 keV)	" " 37
7-7	" " " (10 keV)	" " 37
7-8	" " " (20 keV)	" " 37
7-9	Variation of h_m with Season/Variation of q_m/F with Season	" " 37

7-10	Variation with $F_{10,7}$ (1 and 2 keV)	following page	39
7-11	" " " (5 keV)	"	39
7-12	" " " (10 keV)	"	39
7-13	" " " (20 keV)	"	39
7-14	Variation of h_m with $F_{10,7}$/Variation of q_m/F with $F^m_{10,7}$	"	39
7-15	Variation with Geomagnetic Activity Index a_p (1 and 2 keV)	"	42
7-16	Variation with Geomagnetic Activity Index a_p (5 keV)	"	42
7-17	Variation with Geomagnetic Activity Index a_p (10 keV)	"	42
7-18	Variation with Geomagnetic Activity Index a_p (20 keV)	"	42
7-19	Variation of h_m with T_{exo} for Sanae	"	43
7-20	" " q_m/F with T_{exo} for Sanae (1 and 2 keV)	"	43
7-21	Variation of q_m/F with T_{exo} (5, 10 and 20keV)	"	43
8-1	Ionization Rate Profiles for Different e-folding Energies (Vertical Incidence at the Pole)	"	46
8-2	Variation of $Q/\pi J_o$ with T_{exo} (2 and 5 keV)	"	47
8-3	" " " " " (50 keV)	"	47
8-4	Variation of $Q/\pi J_o$ with Dip Angle (2 and 5 keV)	"	49
8-5	Variation of $Q/\pi J_o$ with Dip Angle (50keV)	"	49
8-6	Variation of $Q/\pi J_o$ with T_{exo} at Sanae (2 and 5 keV)	"	49
8-7	Variation of $Q/\pi J_o$ with T_{exo} at Sanae (20 keV)	"	49
8-8	Variation of $Q/\pi J_o$ with T_{exo} at Sanae (50 keV)	"	49
8-9	Variation of $Q/\pi J_o$ with T_{exo} at Sanae (100 keV)	"	49

Chapter 1 Introduction

Precipitation of energetic particles into the upper atmosphere is known to cause aurora at high latitudes. Sanae is situated in the vicinity of the South Atlantic Geomagnetic Anomaly (Gledhill and Van Rooyen (1963)) where the magnetic field intensity is very low and it is felt that this phenomenon may enhance the loss of particles from the trapping zone into the upper atmosphere.

Previous work at Rhodes has shown that it is extremely likely that particle precipitation could be the cause of some ionospheric effects at Sanae. Gledhill and Torr (1966) found that a "disturbed" ionosphere at Sanae was linked with "high" fluxes of precipitated electrons in the area conjugate to Sanae. Later papers by Gledhill, Torr and Torr (1967), and Torr and Torr (1967a, 1968a) established that electrons are precipitated over a large part of the earth's surface and this phenomenon is probably responsible for an average of about 30% of F-layer disturbances. The frequency of precipitation and corresponding disturbances is most pronounced in the South Atlantic Geomagnetic Anomaly.

Several authors have used the idea of precipitated electrons as a cause of some ionospheric phenomena. These include Blamont and Chanin-Lory (1965), Ivanov-Kholodny (1965) Kamiyama (1966), Krassovsky et al (1965), Lauter and Knuth (1965), Maehlum (1967, 1968), Nesterov et al (1964), Oguti and Marubashi (1966), Ondoh (1966) and Yonezawa (1965a).

Nearer home Gledhill (1970) and Torr and Torr (1967b, 1968b, 1969a, 1969b, 1970) have taken account of electron precipitation to explain some ionospheric effects at Sanae and they have had reasonable success in each case.

Further work is being hampered by a lack of knowledge of the height distribution of the ionization caused by precipitated energetic electrons.

Ionization rate profiles produced by precipitated electrons have been used for the investigation of auroral phenomena, see e.g. Rees (1963, 1964b), Maeda (1965) and Berger, Seltzer and Maeda (1970). The ionization rate profiles have been calculated for the case of energetic particles precipitated vertically above the geomagnetic pole (vertical incidence). Sanae (geomagnetic

coordinates ($-63{,}62^{o}$, $44{,}13^{o}$)) lies outside the auroral zone and without thorough investigation we have no reason to believe that we will obtain the same results for Sanae as at the pole.

The aim of this thesis is to develop a simple and fast computer program which will reproduce the best results to date for electrons vertically incident at the geomagnetic pole and then to study the effect of changing the model atmosphere and other parameters such as latitude and dip angle of the magnetic field.

For Sanae in particular we will study hourly and seasonal variations and also the influence of solar activity, measured by the 10,7 cm solar flux ($F_{10,7}$), and the geomagnetic index (a_p) on the ionization rate profile. The 10,7 cm solar flux is an indicator of the x-ray flux which is responsible for increased ionization in the model atmosphere. (Gibson and Van Allen 1970).

In the above cases we will consider a monoenergetic beam of electrons of "IDH" pitch angle distribution. ("IDH" is an abbreviation for "isotropic over the downward hemisphere" - a term which will be described in the next chapter). Finally in Chapter 2 we look at the ionization rate profile produced by a flux of electrons with a typical integral exponential energy spectrum of the type $J_{>E} = J_o\, e^{-E/E_o}$ where

$J_{>E}$ is the integral directional flux of electrons with energy $> E$
J_o is the integral directional flux of electrons with energies greater than zero,
E_o is the e-folding energy and
E is any selected energy.

Chapter 2 Background

The question to be answered is: "If energetic electrons are precipitated into the upper atmosphere and lose their energy by ionizing collisions with heavier molecules, how is this energy loss distributed with altitude?"

From a study of the dynamics of charged particles in the earth's magnetic field we know that under collision-free conditions electrons are guided along field lines until they reach their mirror points and are reflected back along the field lines. Alfvén's equation tells us that the mirror field intensity is determined by the magnetic field intensity B and the pitch angle of the electron at some reference level. Some electrons are always lost from the trapping region i.e. those in the "loss cone" which either travel along the field line (with pitch angle $\theta = 0$) or have pitch angles such that they would mirror low down in the atmosphere where the likelihood is great that they will collide with heavier molecules and lose energy while also being deflected from their original path. Since the mirror point is determined by the magnetic field intensity we would expect a far greater supply of energetic electrons to regions of higher atmospheric density to occur when an anomalously low magnetic field intensity causes electrons to penetrate much more deeply into the atmosphere. This is the situation which arises in the South Atlantic Geomagnetic Anomaly.

Let us for the moment ignore the magnetic field and the complications to which it gives rise such as mirror points and the spiral motion of charged particles and consider a very simple situation. Assume a plane stratified atmosphere, decreasing in density with height, demarcated into horizontal laminations. We know the mass density at each level. Monoenergetic electrons are fired vertically downwards into this atmosphere. We want to know how much energy is lost by the "average" electron in each lamination. Energy is released to the surrounding medium when the electron collides with, and excites or ionizes, the atoms and molecules of the medium. The electron is very light and is expected to be deflected considerably from its original direction of travel as a result of collisions. It is thus very difficult to estimate the most likely path of the electron. So we may look to nuclear physics and the results of analyses of the penetration of β rays in air. These results represent a statistical average of many individual case histories. Experiments have been carried out and the results formulated as empirical range-energy relations. The relation is usually of the form

$R = m E_i^n$ where R (the range) is expressed in the units g/cm^2 when E_i (the initial energy) is in keV, m and n are constants found from experiment. The range, R, is the total "distance" the electron is expected to penetrate into the target medium before it has lost all its energy.

The units g/cm^2 may at first seem rather strange but it is actually a neat way of expressing the behaviour of an energetic electron under widely differing conditions. The distance an "average" electron will travel in a certain medium depends upon how quickly it gives up its energy to the surroundings i.e. on the number of collisions it undergoes. This naturally depends on the density of the medium. So we express range in g/cm^2 by multiplying the distance travelled in cm by the density of the medium in g/cm^3. We can now apply the same formula to the case of an "average" electron fired into another medium with a different density and find out the depth to which the electron is expected to penetrate the medium. This depth is measured in the conventional units of cm.

If the electron lost equal amounts of energy along equal intervals of the range the formula would simply be:
(Energy deposited per cm^3 per sec per unit flux at altitude h)
= (initial energy/range) (density at h).

Unfortunately things are a little more complicated than appear at first. Theoretical calculations by Spencer (1955) and experiments by Grün (1957) show that the amount of energy lost at any particular stage along the range is dependent upon the fraction of the range which has been covered. The normalized energy deposition function has been called the "Lambda function" $\lambda(z/R)$ by Grün and we shall refer to it in the same way. The diagram below shows the λ- function appropriate for the monodirectional case.

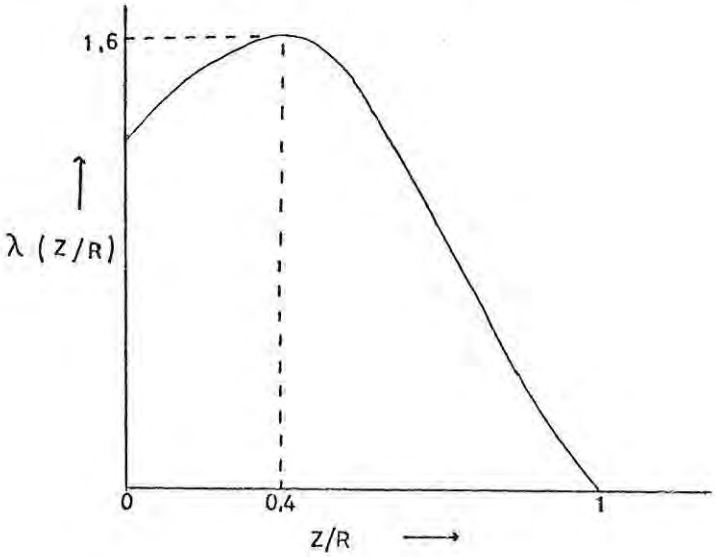

Our problem is now formulated:
(Energy deposited per cm^3 per sec per unit flux at h) =
(initial energy/range) (density at h) (λ-function at h)
in symbols:

$$e_h/F = (E_i/R)\ D\ (h)\ \lambda\ (z/R)\ \text{keV/el-cm} \qquad (2\text{-}1)$$

e_h/F is the energy deposited per cm^3 per sec per unit flux at height h
z is the total "path length" in g/cm^2 from the "top of the atmosphere" down to height h.
z/R is the fraction of the range travelled.
All other symbols have previously been explained.

To convert (2-1) to ionization rate or ion pairs produced per unit volume per unit time per unit flux we divide the right hand side of (2-1) by the average energy lost per ion pair formed whose value we take to be 35 eV/ion pair formed (Rees (1963)). If E_i is in keV this becomes

$$q_h/F = (E_i/0{,}035R)\ D(h)\lambda(z/R) = e_h/0{,}035F \quad \text{ion pairs/el-cm} \qquad (2\text{-}2)$$

(2-1) and (2-2) have been expressed in different notation by different workers in this field. Any difference in results usually lies in the choice of a λ-function and the model atmosphere (D(h)).

The λ-function also changes when the pitch angle of the incident electron changes (see Fig 3 from Berger et al (1970)). (Reproduced overleaf).

It seems unlikely that precipitating electrons would be monodirectional unless they were fired from a rocket (e.g. Hess et al (1971)). Normally we would expect some kind of distribution in pitch angle and it should be possible to find an appropriate λ-function for any pitch angle distribution by integrating over the λ's for the relevant pitch angles, weighted according to the distribution function. O'Brien (1962a) has measured fluxes of particles and found that during precipitation events they have a distribution which is isotropic over the downward hemisphere (IDH). The λ-function for the IDH case is also shown in Fig. 3 from Berger et al.

Although IDH fluxes are obviously very important the author has never yet seen a lucid treatment of the concept. Till now we have only considered a monodirectional flux which, as its name implies, travels initially along a

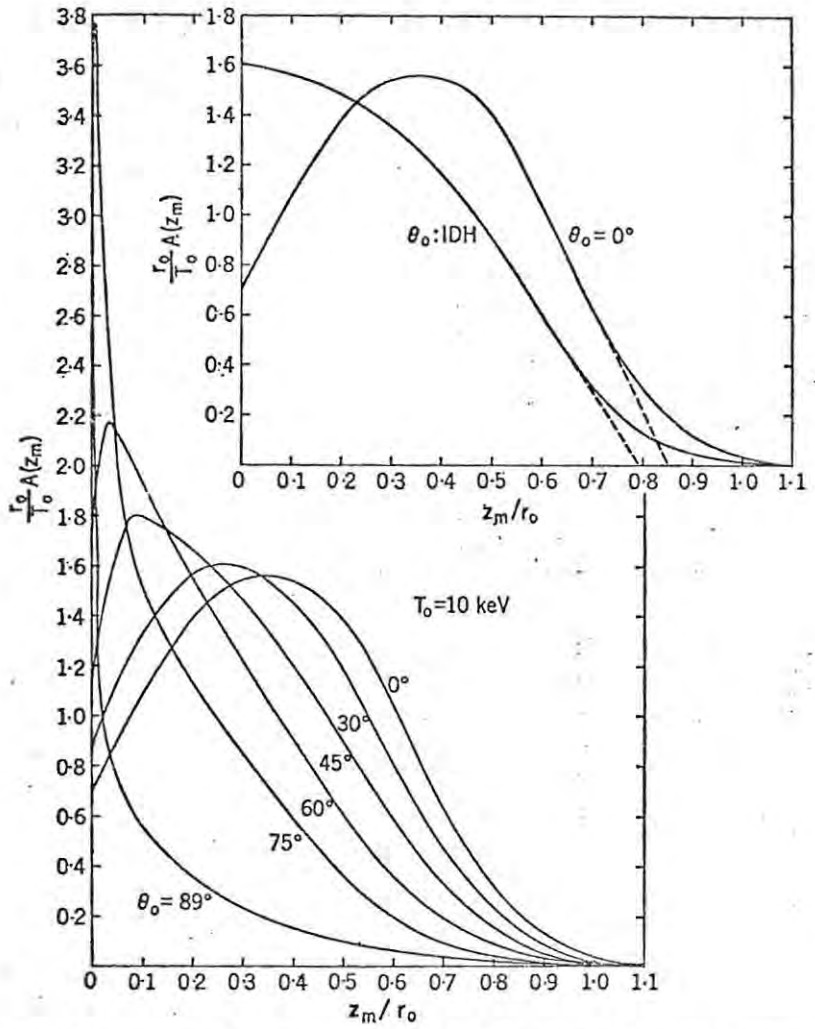

Fig. 3. Penetration function in a semi-infinite air medium, as function of the atmospheric depth for beams incident at various angles. The case IDH pertains to the initial pitch-angle distribution equation (3.4).

single direction. (Any later change in direction of travel as a result of collisions is taken into account in the λ-function.) The term "isotropic" means that particles are equally likely to come from any direction and if we are talking of a flux which is isotropic over the downward hemisphere we mean that particles are equally likely to come from any direction which has a downward component. If J_{mono} is the directional flux for a mono-energetic beam of electrons then the IDH flux $J_{IDH} = \pi J_{mono}$. This last statement is described clearly in a treatment of the concept of fluxes with special reference to IDH fluxes due to Professor J.A. Gledhill. He has very kindly permitted me to include his treatment in this thesis and it may be found in Appendix 1.

In this thesis we consider only ionization rates per unit flux and we denote the flux by F, whether it is monodirectional or IDH. Although (2-1) and (2-2) have been derived for a monodirectional flux the expressions remain the same

for an IDH flux provided the appropriate λ-function is used.

The results given in this thesis may be used to calculate the ionization rate for any given flux. If the directional flux value is given the corresponding IDH flux is π x directional flux.

Recent contributions to our knowledge of ionization rate profiles are the papers of Chamberlain (1961), Rees (1963, 1964b), Maeda (1965) and Berger et al (1970). Each has used the same basic formula ((2-1) or (2-2)) with slight changes.

Chamberlain (1961) used results of Spencer (1955, 1959a) in the calculation of ionization rate profiles from formula (2-2). Spencer used radiative transfer theory to calculate theoretical values of the range of β particles in air and also the λ-function (in his notation $J_\varsigma / J_{\varsigma\ o}$). His results did not take account of straggling. The formula Chamberlain used differs slightly from (2-2) by the subtitution of $(D(R)\ n(M)_z/n(M)_R)$ for $D(h)$ where

z refers to the total path length down to height h, R refers to the range. z and R have the same units of g/cm^2.

$n(M)_z$ = number density of ionizable constituents at point z in path ($= n(M)_h$)

$n(M)_R$ = number density of ionizable constituents at point R in path

$D(R)$ = the mass density "at the bottom of the atmosphere".

This is a reasonably valid way of scaling the atmospheric densities if the relative concentrations of the different molecules remains the same. However, above 100 km the atmospheric molecules separate out according to their relative molecular masses. This means that the mean molecular mass changes as we go from 90 km to 300 km.

The relation $D_{(h)} = D_{(z)} = D_{(R)}\ n(M)_z/n(M)_R$ (2-3)

implies that the mean molecular mass remains constant for the region from 300 km down to R as may be seen from the following reasoning.

The average molecular weight at the ith altitude

$$M_i = \sum_k n_{ki}\ M_k / \sum_k n_{ki}$$

n_{ki} = number density of molecules of species k with molecular weight M_k.

The mass density at the ith altitude $D_i = \sum_k n_{ki} M_k =$

$$\left(\sum_k n_{ki} M_k / \sum_k n_{ki} \right) \sum_k n_{ki} =$$

$$M_i \sum_k n_{ki}$$

Choose another altitude j ($j \neq i$)
with the mass density at the jth altitude $D_j = M_j \sum_k n_{kj}$ -(a)

For relation (2-3) to hold this implies

$$D_j = M_i \left(\sum_k n_{ki} / \sum_k n_{ki} \right) \sum_k n_{kj} = M_i \sum_k n_{kj} \qquad -(b)$$

Comparing (a) and (b) we see that this implies $M_j = M_i$.

The CIRA 1965 mean model atmosphere gives the mean molecular weight at 90 km as 28,94 and at 300 km as 18,87. We see that $M_{90} \neq M_{300}$ and the use of (2-3) in the scaling of atmospheric densities leads to an overestimation of density at greater heights.

Rees (1963) closely followed Chamberlain's method, differing only in the choice of a range-energy relation and the λ-function. For these he used experimental results of Grün (1957) who measured the luminescence radiation emitted by nitrogen when bombarded by monodirectional electron beams with energies between 5 and 54 keV. He obtained the λ-function by integrating the light output over plane slabs perpendicular to the direction of the incident beam. Grün found the range-energy relation to be $R = 4{,}57 \times 10^{-6} E_o^{1{,}75}$.

For a 32 keV beam of electrons Grün recorded a three-dimensional energy deposition distribution which he published in the form of contour lines of equal luminosity. Rees used this to obtain the λ-function for different pitch angle distributions viz. monodirectional, "isotropic" ($0^\circ - 70^\circ$), "isotropic" ($0^\circ - 80^\circ$) as well as the "cosine distribution" which is also known as "isotropic over the downward hemisphere". Note that Rees's use of "isotropic" is incorrect and does not conform to the usual definition.

The model atmosphere used by Rees is given in table 2-1.

Table 2-1

Rees Model Atmosphere

h(km)	D(g/cm^3)	n(M) (cm^{-3})
92	2,17 (-9)	4,37 (13)
96	9,93 (-10)	2,07 (13)
100	4,48 (-10)	1,04 (13)
108	1,32 (-10)	3,18 (12)
114	5,70 (-11)	1,43 (12)
120	2,61 (-11)	6,61 (11)
126	1,30 (-11)	3,40 (11)
132	7,05 (-12)	1,91 (11)
140	3,47 (-12)	9,70 (10)
150	1,70 (-12)	4,92 (10)
162	9,00 (-13)	2,66 (10)
192	2,94 (-13)	9,50 (9)
230	1,16 (-13)	3,89 (9)
252	7,60 (-14)	2,57 (9)
276	5,00 (-14)	1,72 (9)
300	3,42 (-14)	1,20 (9)

For 2,17(-9) read 2,17 x 10^{-9}. Likewise for all subsequent tables.

FIG. 2-1

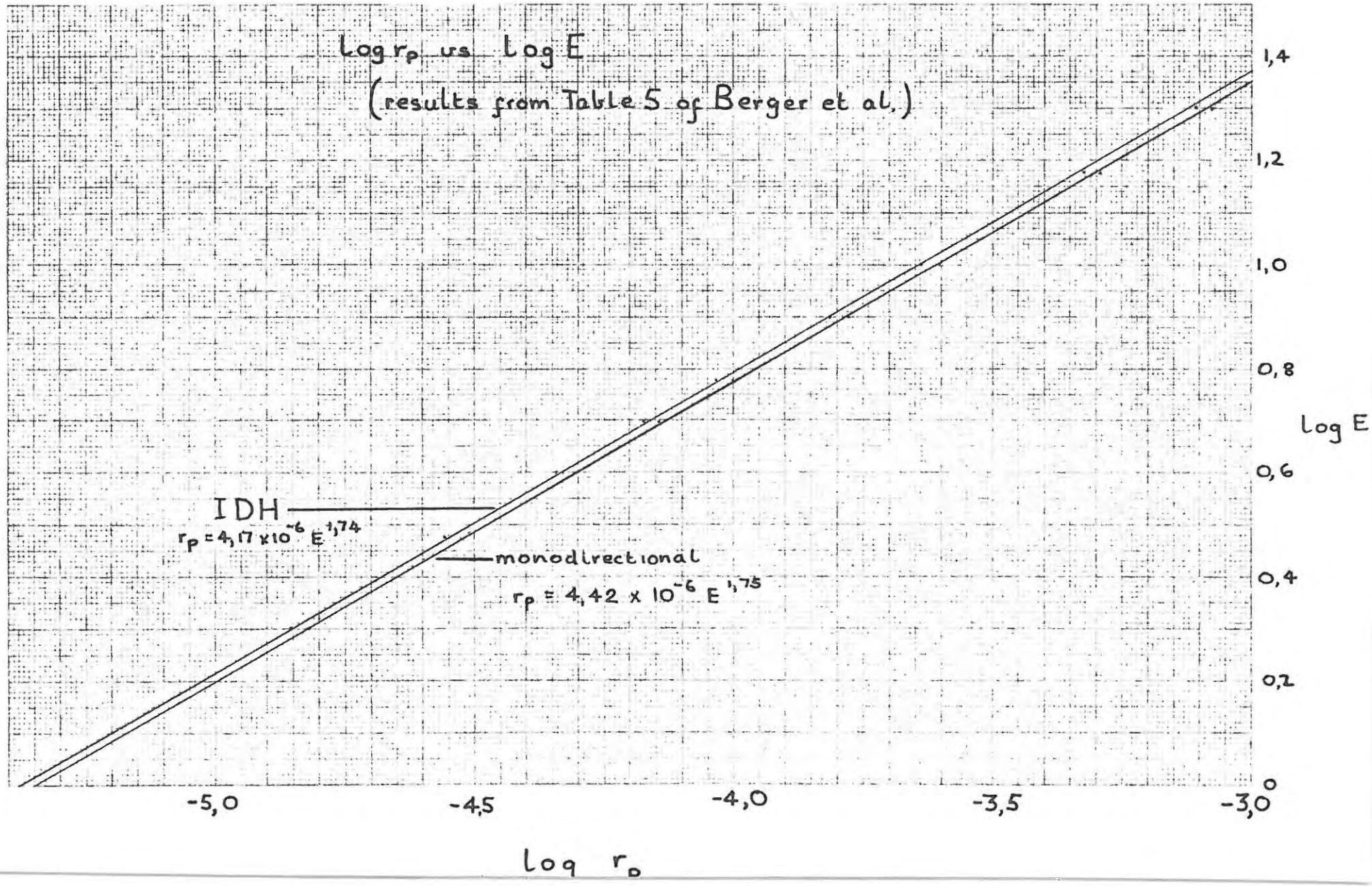
Log r_p vs Log E
(results from Table 5 of Berger et al.)
IDH
$r_p = 4,17 \times 10^{-6} E^{1,74}$
monodirectional
$r_p = 4,42 \times 10^{-6} E^{1,75}$
1,4
1,2
1,0
0,8
0,6
0,4
0,2
0
Log E
-5,0
-4,5
-4,0
-3,5
-3,0
Log r_p

In a second paper (1964b), Rees included the effect of the earth's magnetic field and concluded that any influence it had was very small.

Maeda (1965) used Monte Carlo type calculations i.e. studying the case histories of several thousand electrons undergoing Coulomb scattering and continuous energy loss in the CIRA 1965 mean model atmosphere. The basic formula is the same as (2-1) (although the notation is different). The Monte Carlo method calculates the λ -function and range using the Bethe theory for determining the mean energy loss, multiple scattering theory of Goudsmit and Sanderson (1940) and single scattering with Mott's cross section (Mott, 1929). Straggling is taken into account using the theory of Blunck and Liesegang (1950). Maeda studied IDH and monodirectional (vertical incidence) cases both with and without straggling for monoenergetic electron beams from 2 - 20 keV.

Berger, Seltzer and Maeda (1970) extended this work and took into account the effect of a magnetic field. The λ-function was calculated by the Monte Carlo method and gave good agreement with the experimental results of Grün. They published values of practical range for different energies for both monodirectional and IDH fluxes. Range-energy relations were derived from these published values and were found to differ in the monodirectional and IDH cases. (See fig 2-1 which shows the plot of log E vs log R for both cases).

Monodirectional: $R = 1{,}42 \times 10^{-6} E_i^{1{,}75}$ g/cm^2

IDH: $R = 4{,}17 \times 10^{-6} E_i^{1{,}74}$ g/cm^2

cf Grün (monodirectional): $R = 4{,}57 \times 10^{-6} E_i^{1{,}75}$ g/cm^2

The densities were used directly from the CIRA 1965 mean model atmosphere and not scaled from the greatest density as Chamberlain and Rees preferred to do.

While most workers have used formulae similar to (2-1) or (2-2), Gledhill and Van Rooyen (1963) proposed an entirely different method. They took account of the earth's magnetic field by using a monopole approximation to the dipole field. Then they could "unwind" the helical path of the electron to obtain the actual path length and use this in the residual range method to determine the energy lost in each lamination.

It was an interesting method but, although it takes account of electrons mirroring in the magnetic field, it assumes that electrons with a given pitch angle at "the top of the atmosphere" continue along the same path without being deflected by collisions. This is an assumption which oversimplifies the situation as the electrons are naturally deflected considerably from their original direction of travel as a result of collisions. The λ function takes account of this.

Chapter 3 The Computation of Ionization Rate Profiles

As we have mentioned before, the aim of this thesis is to produce a fast and accurate method of computing ionization rate profiles to fit the best available results to date.

For our standard we have chosen the results of Berger et al whose Monte Carlo type calculations are based on known interactions of atoms and electrons. The λ function calculated in this way gives good agreement with experimental results of Grün (1957). The Monte Carlo calculations also yielded values of the "practical" range of electrons in air which differ only slightly from Grüns result. For these reasons we believe the results of Berger et al to give a truer representation of the ionization produced by precipitated electrons than, for example, results of Chamberlain who used Spencer's theoretical λ's which have not been compared with experimental results, or results of Rees who used Grün's experimental values for λ but did not take into account the change of range with pitch angle distribution and also assumed constant composition of the relative constituents of the atmosphere.

Although we are interested mainly in the case of IDH incidence the modification from monodirectional to IDH is very easy so we shall first discuss the method of solution for the monodirectional case and indicate the conversions necessary for the IDH case.

The atmosphere from 300 km to 90 km is divided into horizontal laminations of varying thickness. We are not interested in the region below 90 km because we do not have ionograms for that part of the ionosphere and also because bremstrahlung begin to play an increasingly important part and this would complicate computations (G.J. Freyer III (1969)). This has the disadvantage that our results cannot be used to calculate the absorption of radio waves which takes place mainly below 90 km.

Let us now consider a monoenergetic, monodirectional beam of electrons with zero pitch angle (i.e. they travel along the magnetic field lines). We may represent the nth lamination diagrammatically.

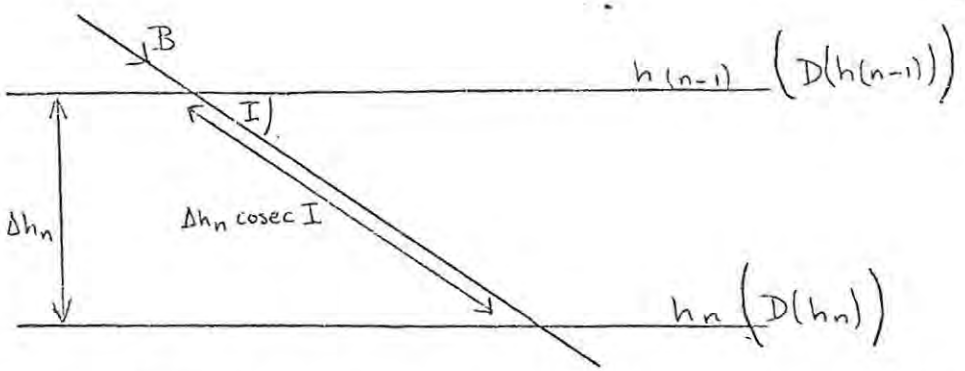

The two height levels are h_{n-1} and h_n with respective densities $D(h_{n-1})$ and $D(h_n)$. Δh_n is the thickness of the nth lamination. If the lines of force of the magnetic field have an angle of dip I then the distance an average electron will travel through a lamination is Δh_n cosec I. This "distance of travel" in the lamination must be converted to "path length" in the units g/cm^2. To do this we convert Δh_n to cm and multiply Δh_n cosec I by the average mass density in the lamination. To find the average mass density we assume an exponential distribution of density with height in the lamination.

$$D(h_n) = D(h_{n-1}) \exp\left[-\gamma (h_n - h_{n-1})\right] \qquad \gamma \text{ a constant}$$

and find that the average may be expressed in the following way

$$\overline{D}(\Delta h_n) = \left(D(h_{n-1}) - D(h_n)\right) / \ln\left(D(h_{n-1})/D(h_n)\right)$$

See Appendix 2).

The total path length down to the height h_n must now be expressed as a fraction of the range in order to find the value of the normalized energy deposition factor $\lambda (z/R)$ at the height h_n. The range is found from the range-energy relation for monodirectional electrons $R = 4{,}27 \times 10^{-6} E^{1{,}76}$ g/cm^2 (derived from results published by Berger et al).

The values obtained as above are substituted into the formula (2-2) viz

$$q_{h_n}/F = \left(E_i/0{,}035R\right) \lambda (z_n/R) \; D(h_n)$$

with E_i the initial energy in keV and $D(h_n)$ in g/cm^3

Note that here F refers to the monodirectional flux.

Note that $D(h_n)$ refers to the density at the height h_n and not to the average density in the nth lamination. This is because we are interested in the energy deposited per unit volume per unit time per unit flux at the heights selected and the resulting ionization rate profile will represent the vertical distribution with height even when the dip angle I is not 90^o. To illustrate this consider the diagram below.

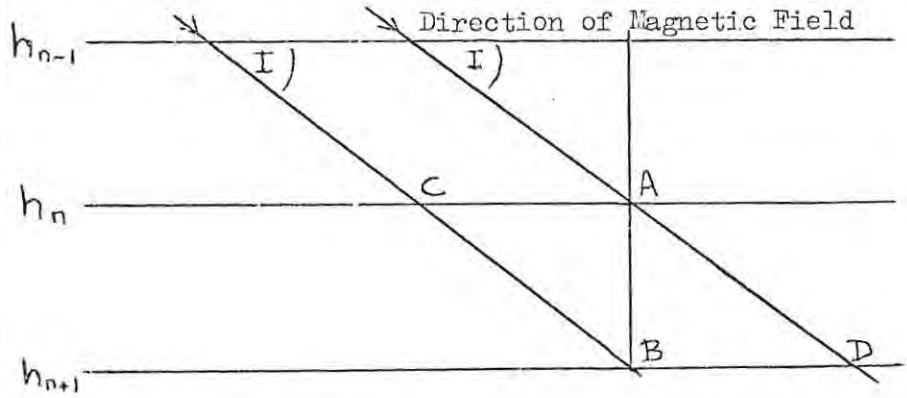

We are interested in the ionization rate at A and B. If the beam of electrons is vertically incident on the layer then the path length z is simply $\Delta h_n \overline{D}(\Delta h_n)$ and $\lambda(z/R)$ at A determines the rate at which ionization is produced in a unit volume at A. If we now consider a beam of electrons incident along the direction of the magnetic field ($I \neq 90^o$) then the path length in the lamination is increased to $\Delta h_n \overline{D}(\Delta h_n)$ cosec I and the $\lambda(z/R)$ at A for the beam of electrons is now different from the one appropriate for vertical incidence. This means that the beam of electrons incident along the field line with $I \neq 90^o$ has lost more energy in the overlying laminations and produces less ionization at A than the beam of electrons with vertical incidence. Ionization at B is caused by the electrons which have travelled through C while the electrons which caused ionization at A leave the lamination at D.

To convert the program from the monodirectional to the IDH case only two variables are changed: the range R and the λ-function. It is not economical to obtain the IDH ionization rate profile directly from the monodirectional profiles by using the method of integrating over the pitch angles. This method would involve calculating monodirectional profiles for electrons at frequent intervals of pitch angle, each with its own λ- function, and summing over the contributions each of which have been weighted by the factor $\sin\theta \cos\theta \, d\theta$ (see Appendix 1). We have therefore used a mean λ_{IDH} function obtained from values published by Berger et al. They found the λ_{IDH} function

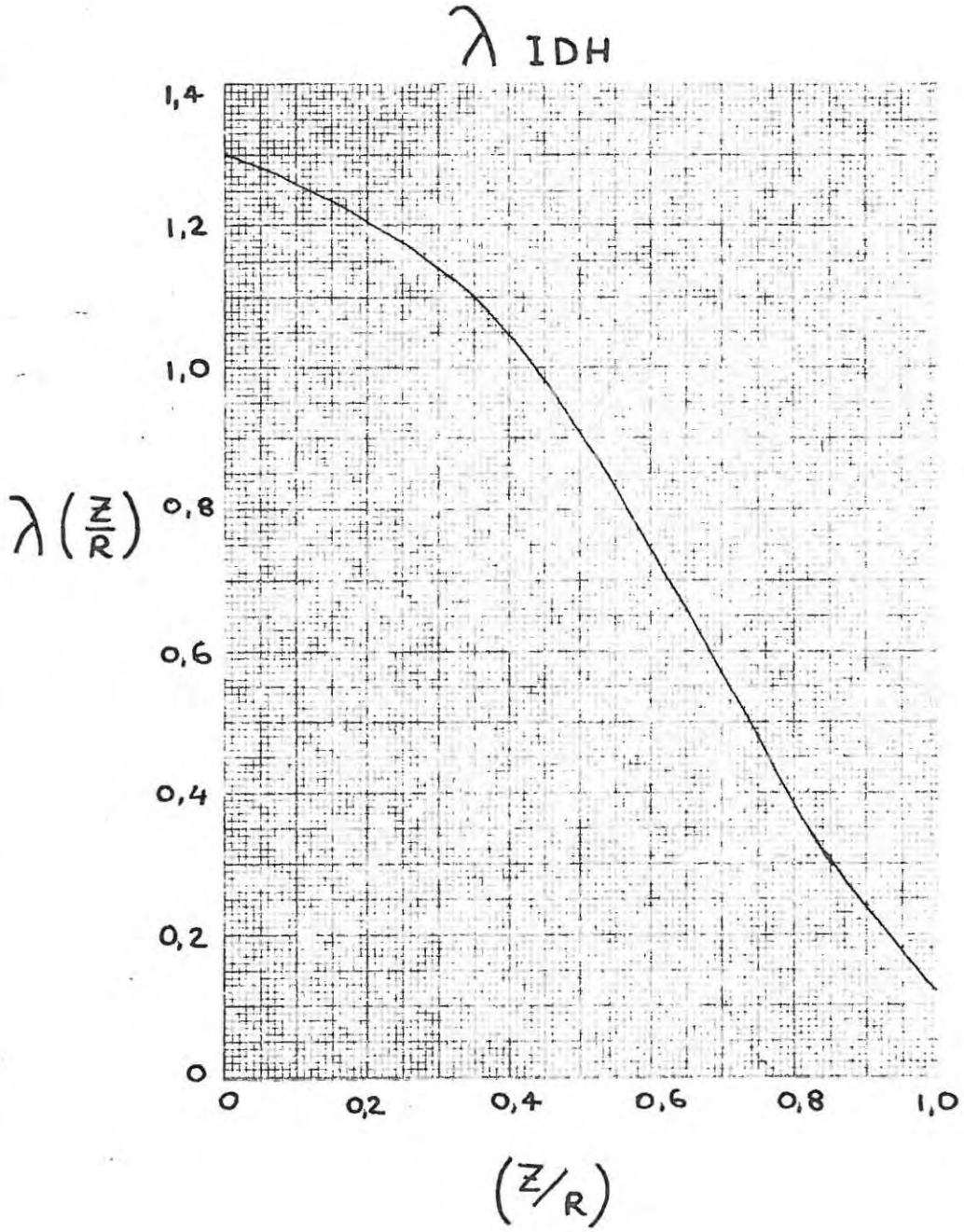

FIG. 3-1

to vary slightly with incident energy and the λ_{IDH} function used (shown in Fig 3-1) has been chosen to represent the "mean" of the λ -functions obtained for 2,5,10 and 20 keV incident electrons. The "mean" was found not to differ by more than 3% from any of the other curves at any point.

Since the λ -function is different for the IDH case it might be reasonable to suppose that the range also changes. Results from Berger et al indicate that the range for the IDH case is best expressed by the relation

$$R = 4{,}17 \times 10^{-6} E_i^{1{,}74} \quad g/cm^2$$

Note here that we can still find out the ionization rate profile due to an IDH flux in a magnetic field with $I \neq 90^o$. This is because IDH has been defined as the flux passing downward through an element of area oriented perpendicularly to the direction of the magnetic field. So the dip angle will still affect the path length in any lamination and although the ionization is along the field line we are only interested in the vertical distribution which is calculated from our formula (2-2).

We now compare the results of Rees and Berger et al with those of the computer program (called AW 18) which calculates the ionization rate profile following the method outlined above (see Appendix 3 for the flow chart).

Fig. 3-2 shows the close agreement with the results of Berger et al. The solid lines are the results of Berger et al and the X's denote the AW 18 calculations with the CIRA 1965 mean model atmosphere used by Berger et al. The four profiles are for E_i = 2, 5, 10 and 20 keV. Note that we have plotted the energy deposition per unit flux (eV/el-cm) against height as did Berger et al, rather than the production rate per unit flux.

Fig. 3-3 shows Rees's curves for 1 and 10 keV incident electrons (solid lines) and AW 18 computations with the Rees atmosphere for the same initial energies (broken lines). For the 1 keV electron flux the maximum ionization rate (qm/F) increases from $3{,}5 \times 10^{-6}$ in pairs/el-cm (Rees) to $3{,}8 \times 10^{-6}$ ion pairs/el-cm (AW 18) while the height of maximum drops from 170 km (Rees) to 162 km (AW 18).

COMPARISON OF RESULTS OF BERGER et al AND AW18

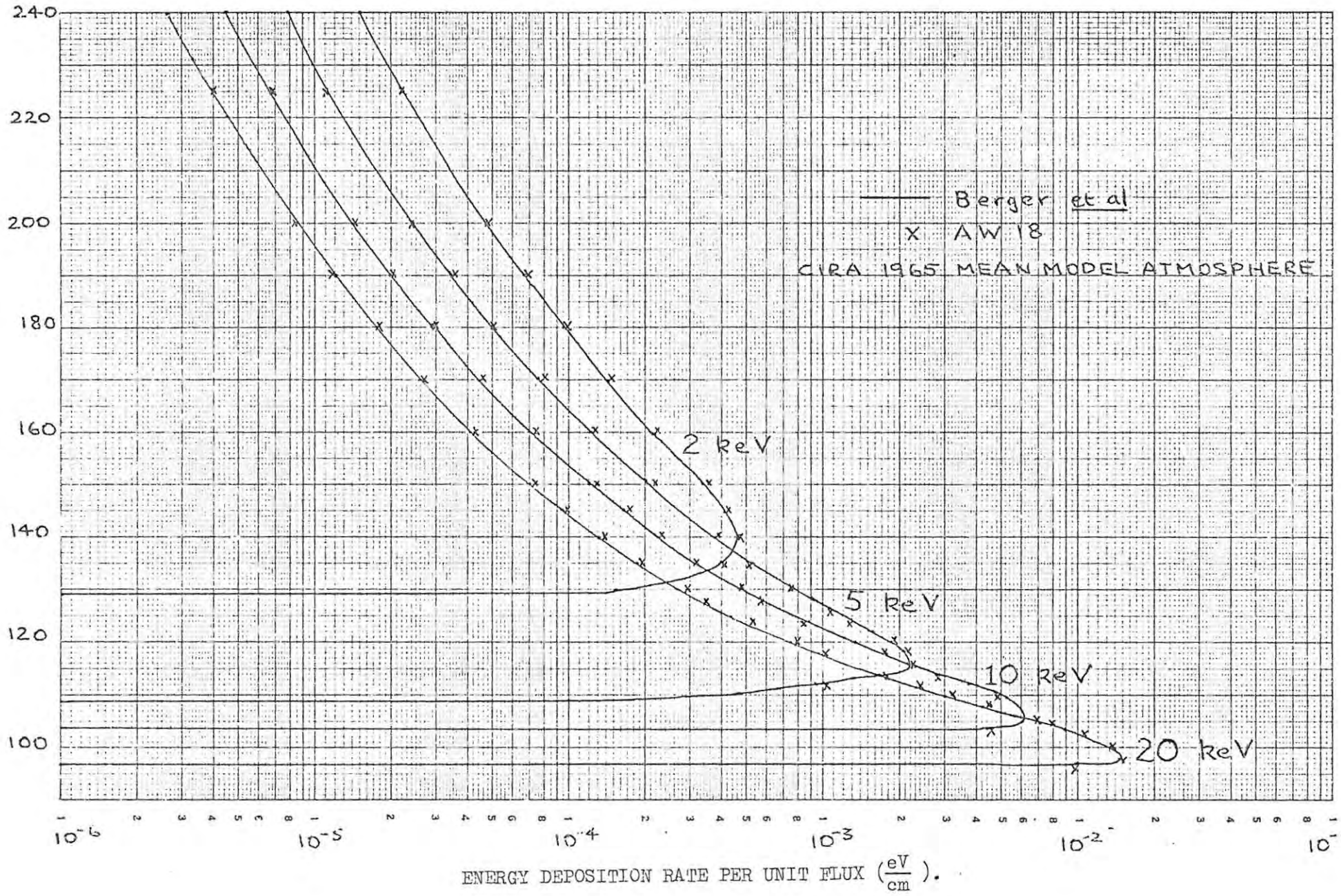

FIG. 3-2

FIG. 3-3

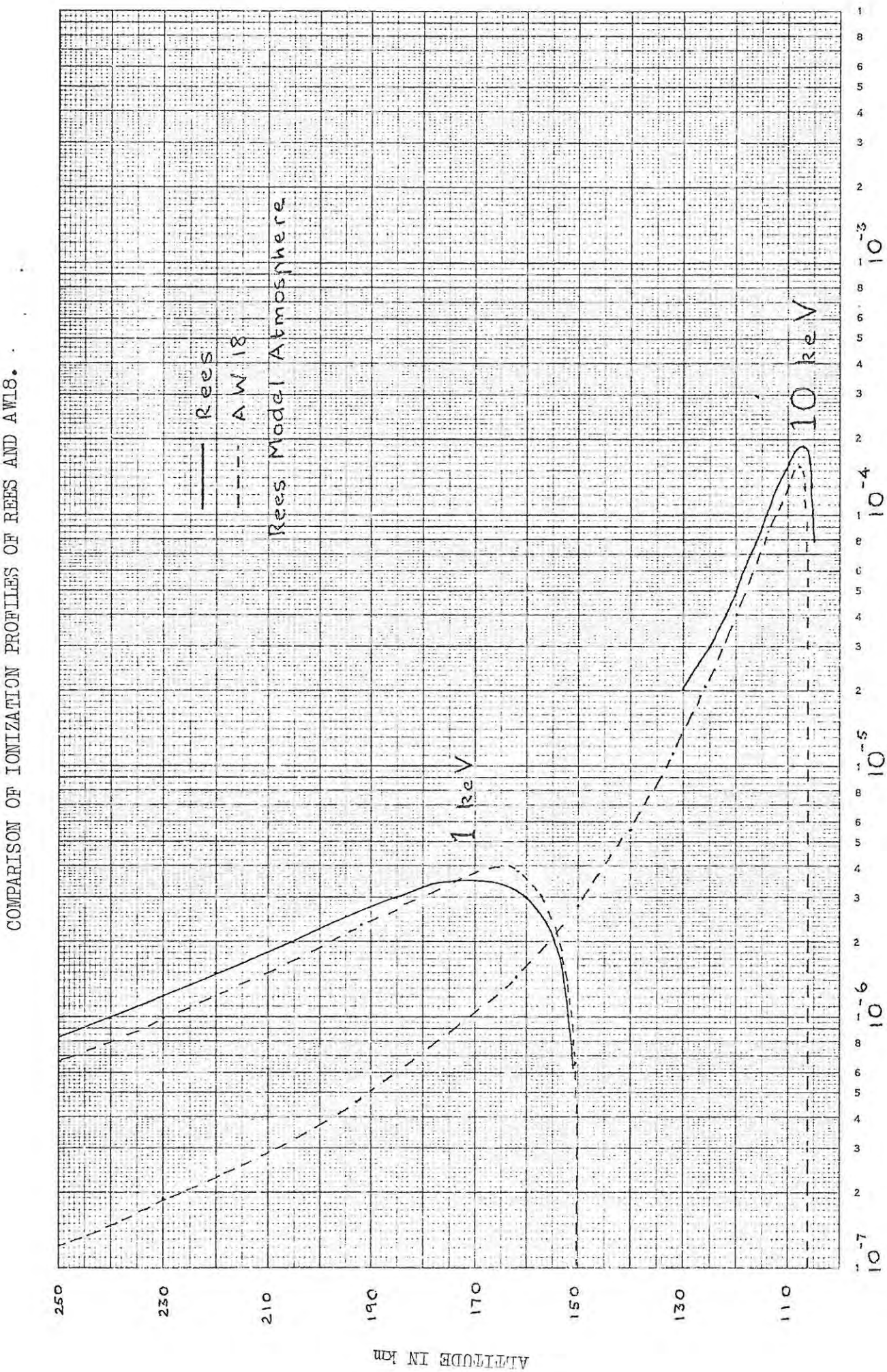

COMPARISON OF IONIZATION PROFILES OF REES AND AW18.

For the 10 keV electron flux (q_m/F) decreases from 1,85 x 10^{-4} ion pairs/el-cm (Rees) to 1,6 x 10^{-4} ion pairs/el-cm (AW 18) and h_m increases from 107 km (Rees) to 108 km (AW 18).

As the AW 18 program depends so very much upon the Monte Carlo results of Berger et al the limitations of their results are also the limitations of the AW 18 results viz:

1. No account is taken of a spatially varying magnetic field. All calculations assume a constant magnetic field.

2. Calculations for $\lambda(z/R)$ were carried out at energies for which the electron scattering cross sections are not very well known.

We conclude this chapter by mentioning that we are interested mainly in the type and size of differences introduced by changing different parameters and as a result if there are some inaccuracies in the calculation of absolute values these will not affect the differences in which we are interested. In later chapters we will study the influence of different model atmospheres, changes in dip angle and the expected ionization rate profiles for stations at different latitudes. For Sanae, in particular, we will study seasonal and daily variations as well as the effect of changes in geomagnetic activity index a_p and 10,7 cm solar flux ($F_{10,7}$).

Chapter 4. Electron Production in Different Model Atmospheres

A model atmosphere such as CIRA 1965 consists of tabulated mass densities and number densities for different heights. Different workers have produced such model atmospheres by attempting to fit theoretical results to satellite data and extrapolating these results through regions where data are not available (e.g. between 80 and 120 km). These models are necessarily simplified and, while their derivation is not of particular interest to us, we must fully understand any limitations and the possible influence of these on results derived from the model atmosphere.

The ionization rate profile depends directly on the mass densities of the model atmosphere. Rees used the model atmosphere given in Chapter 2 while Berger et al used CIRA 1965 mean model atmosphere in theirs. The CIRA 1965 mean model atmosphere is shortly to be replaced by CIRA 1970. For reasons given below we have chosen to use the model atmospheres of Jacchia (1965).

The mean model atmosphere CIRA 1965 is calculated for low latitudes and is not held to be applicable at high latitudes. Jacchia's model atmospheres include a correction for latitude and it is felt that this may help make the model more representative of conditions at high latitudes. The atmospheric density distribution is known to change with exospheric temperature T_{exo}. Jacchia has published tables of mass density with height for the temperature range T_{exo} = 650 K to T_{exo} = 2100 K in 50 degree intervals. He also outlines a method for calculating T_{exo} from the geographic latitude, hour angle of the sun, day number and declination of the sun, 10,7 cm solar flux ($F_{10,7}$) and the geomagnetic activity index a_p. See Appendix 4 for a flow chart of the computer program which evaluates T_{exo}.

The limitations of Jacchia's model atmosphere (120-300 km) are

a) the number densities are fixed at the lower boundary. Incidentally they are the same boundary conditions as used in CIRA 1965 (viz. T = 355 K, $n(N_2) = 450 \times 10^{11}$, $n(O_2) = 7{,}5 \times 10^{10}$, $n(O) = 7{,}6 \times 10^{12}$, $n(He) = 3{,}4 \times 10^{7}$, the units of n being particles per cm^3). These values are acknowledged to be among the best available of recent data from rockets and satellites.

b) the temperature is invariant at the boundary (120 km) and has a constant gradient between 120 km and 150 km. The temperature distribution above 150 km was calculated for the "hottest" model (greatest T_{exo}) assuming thermal equlibrium. Other models were obtained from this model by conduction cooling of the atmosphere in the absence of external energy sources.

c) Static equilibrium of the atmosphere is assumed and this may not be a very good assumption considering that the atmosphere is subject to large variations of temperature (day - night).

Jacchia (1965) also points out (p 220 § 6) that T_{120} may change with geomagnetic activity and also with solar EUV. As T_{120} is assumed to be a fixed boundary condition this may have a marked effect on the realism of the model.

Since we are interested mainly in the upper atmosphere above Sanae (high latitude) we have chosen to use Jacchia's model atmospheres above 120 km rather than CIRA 1965 because it at least takes some account of the variation of atmospheric parameters with latitude. The CIRA 1965 mean model atmosphere is used from 90 km to 120 km. T_{exo} is calculated following Jacchia's method and the densities are interpolated from published values of densities given by Jacchia in Table 1 of his publication. (See Appendix 5 for the flow chart of the interpolation program.)

Let us now take a look at the effect of different model atmospheres on the ionization rate profile (Figs 4-1 to 4-4.) (Note that the height scale is different for each figure). We see that for low energy electrons (Fig 4-1) the profile changes shape from 700 to 2100 K. For a low T_{exo} when the atmosphere is more compressed, most of the energy is lost around the peak while at higher T_{exo} there is more atmosphere at greater altitudes and more energy is deposited at these altitudes so the profile appears "broader" and peaks at a greater altitude than for low T_{exo}. This feature is pronounced for 1 keV electrons, the peak altitude (hm) shifting upwards by some 23 km while the peak ionization rate q_m/F decreases from $5{,}8 \times 10^{-6}$ to $3{,}1 \times 10^{-6}$ ion pairs/el cm i.e. by 47%. The behaviour of 2 keV electrons

VARIATION WITH T_{exo}

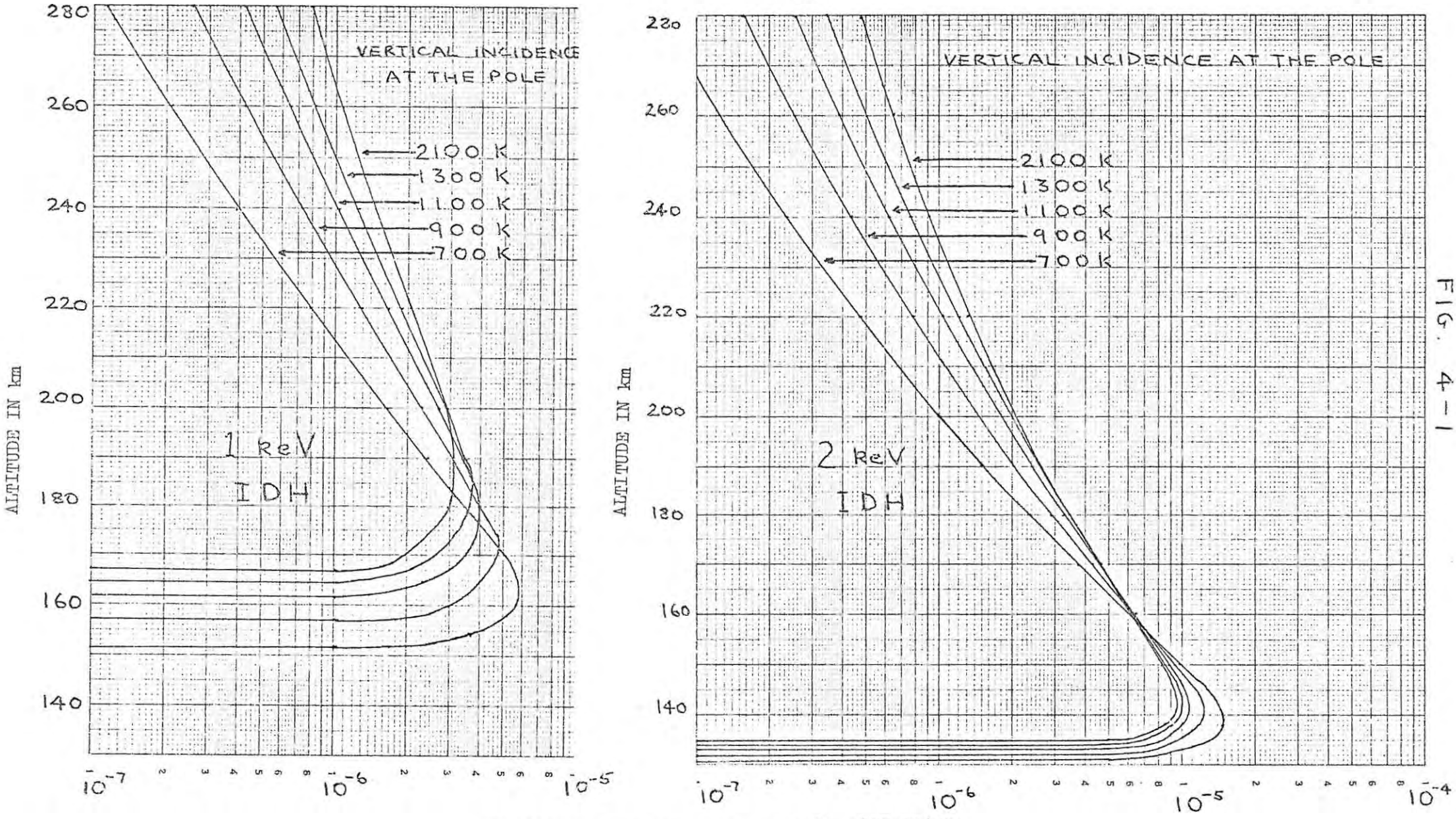

IONIZATION RATE PER UNIT FLUX $\frac{q}{F}$ $\left(\frac{\text{ion pairs}}{\text{el-cm}}\right)$

FIG. 4-1

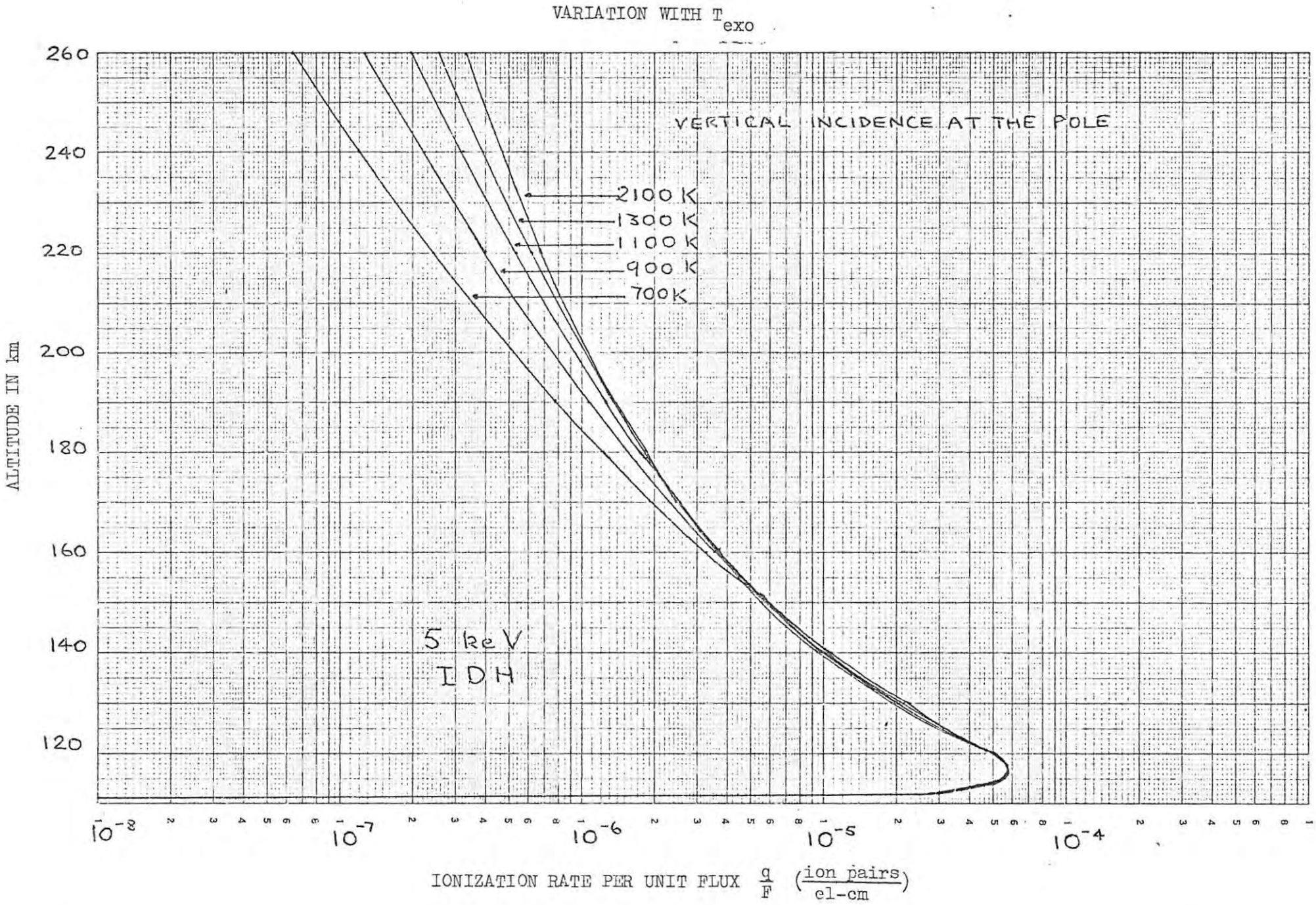
VARIATION WITH T_{exo}
VERTICAL INCIDENCE AT THE POLE
2100 K
1300 K
1100 K
900 K
700K
5 keV
I D H
ALTITUDE IN km
260
240
220
200
180
160
140
120
10^{-8}
10^{-7}
10^{-6}
10^{-5}
10^{-4}
IONIZATION RATE PER UNIT FLUX $\frac{q}{F}$ $(\frac{\text{ion pairs}}{\text{el-cm}})$

FIG. 4-2

FIG. 4-3

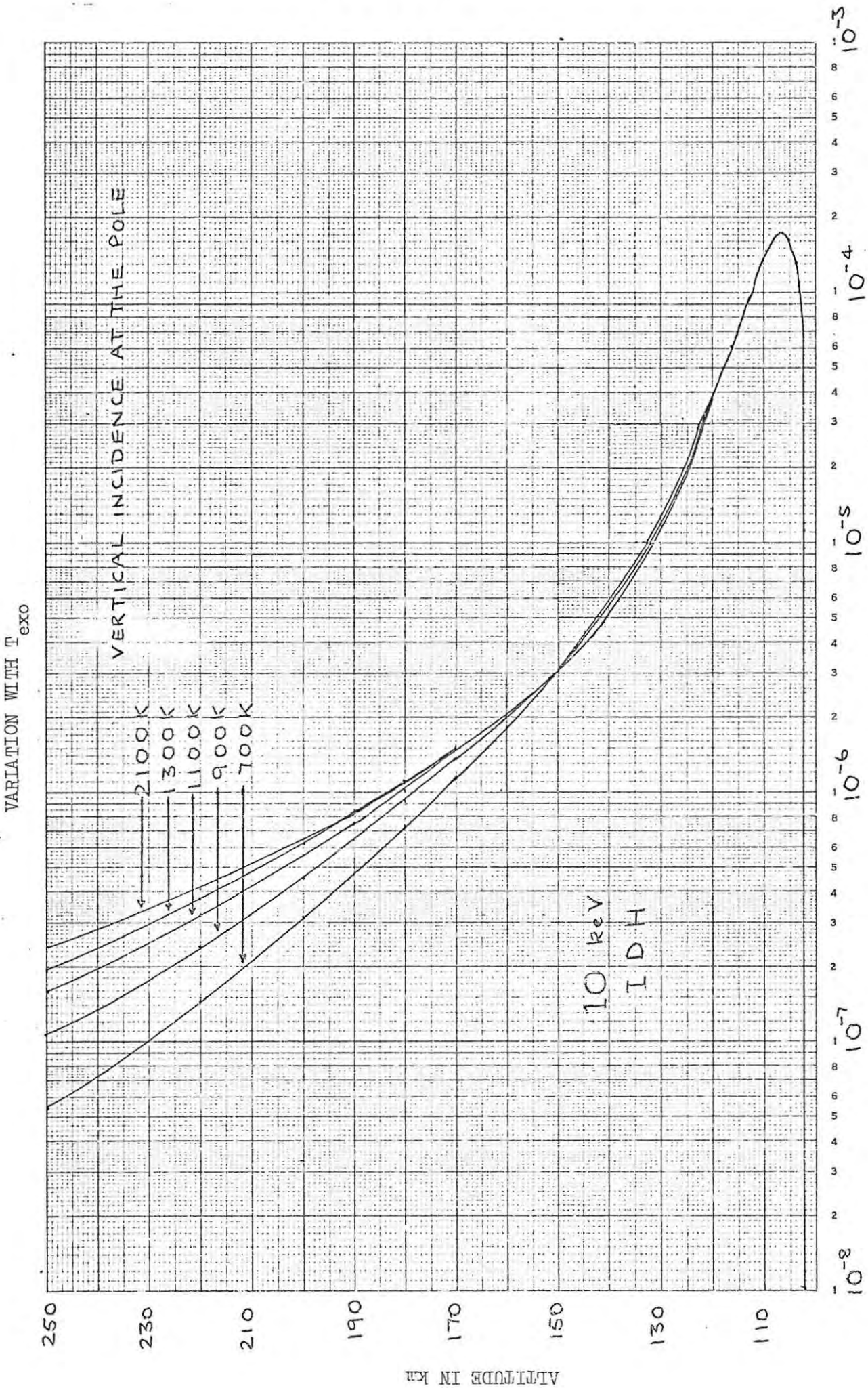
VERTICAL INCIDENCE AT THE POLE
VARIATION WITH T_{exo}
2100K
1300K
1100K
900K
700K
10 KeV
1 D H
ALTITUDE IN Km
250
230
210
190
170
150
130
110
IONIZATION RATE PER UNIT FLUX $\frac{q}{F}$ $\left(\frac{\text{ion pairs}}{\text{el-cm}}\right)$
10^{-3}
10^{-4}
10^{-5}
10^{-6}
10^{-7}
10^{-8}

FIG. 4-4

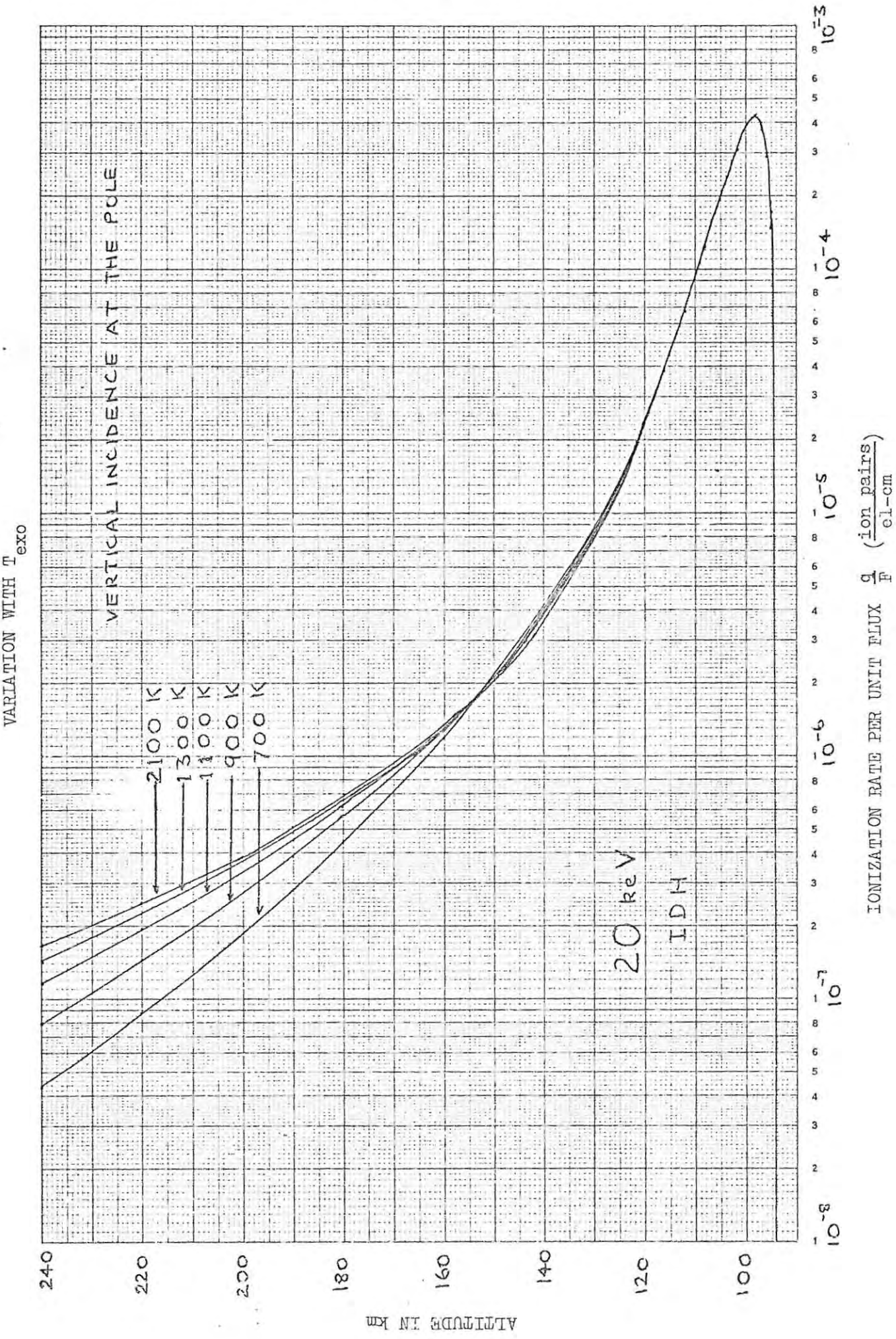
VARIATION WITH T_{exo}
VERTICAL INCIDENCE AT THE POLE
2100 K
1300 K
1100 K
900 K
700 K
20 KeV
IDH
ALTITUDE IN km
240
220
200
180
160
140
120
100
10^{-3}
10^{-4}
10^{-5}
10^{-6}
10^{-7}
10^{-8}
IONIZATION RATE PER UNIT FLUX $\frac{q}{F}$ $\left(\frac{\text{ion pairs}}{\text{cl-cm}}\right)$

is similar although in this case hm only shifts by about 4 km and q_m/F decreases from $1{,}5 \times 10^{-5}$ to $9{,}6 \times 10^{-6}$ ion pairs/el cm i.e. by 36%. When we come to look at the profiles for 5, 10 and 20 keV electrons (Figs 4-2, 4-3, 4-4) we see that the values of hm and q_m/F do not change. Since all three profiles peak at altitudes below 120 km this is most probably a result of using the same model atmosphere (CIRA 1965 mean model atmosphere) below 120 km.

We also notice that for 1 keV electrons at high altitudes the ionization produced in a model atmosphere with low T_{exo} is much less than that in a model with high T_{exo}. This trend is observed until the region between 210 to 180 km is reached when a cross-over takes place and more ionization is produced in a model with low T_{exo} than in a model with high T_{exo}. The altitude at which the productions are equal for two different T_{exo}'s varies for the values of T_{exo} involved.

Similar behaviour is observed for 2 keV electrons although in this case the cross-over takes place between 190 and 155 km. For 5 keV and 10 keV the cross-over region is between 180 and 155 km while for 20 keV it is between 165 and 150 km. Below 150 km the 5, 10 and 20 keV electrons also show that production is less for T_{exo} high than for T_{exo} low until below 120 km when all production rates become practically the same. This is doubtless connected with the fact that we have used a model which does not vary with T_{exo} below 120 km.

Fig 4-5 shows values of hm plotted vs T_{exo} as well as values of log q_m/F vs T_{exo}. As the height of maximum production and the peak ionization rate are difficult to read off the graphs they were calculated by taking four pairs of h and q values around the peak and solving for hm and q_m/F by setting

$$q/F = a + b\,h + c\,h^2 + d\,h^3 \qquad (4\text{-}1)$$

then $d(q/F)/dh = h + 2ch + 3dh^2 = 0$ at the maximum. The expression is solved to give hm (one real solution within the bounds) hm was then substituted into (4-1) to give q_m/F. See Appendix 6 for the flow chart of program MAXHQ.

We see from Fig 4-5 that for 1 keV electrons hm increases and q_m/F decreases as T_{exo} increases from 700 K to 1500 K, from 1500 to 2100 K the increase in hm becomes negligible, lying within 2 km of its asymptotic

FIG. 4-5

VARIATION OF h_m WITH T_{exo}

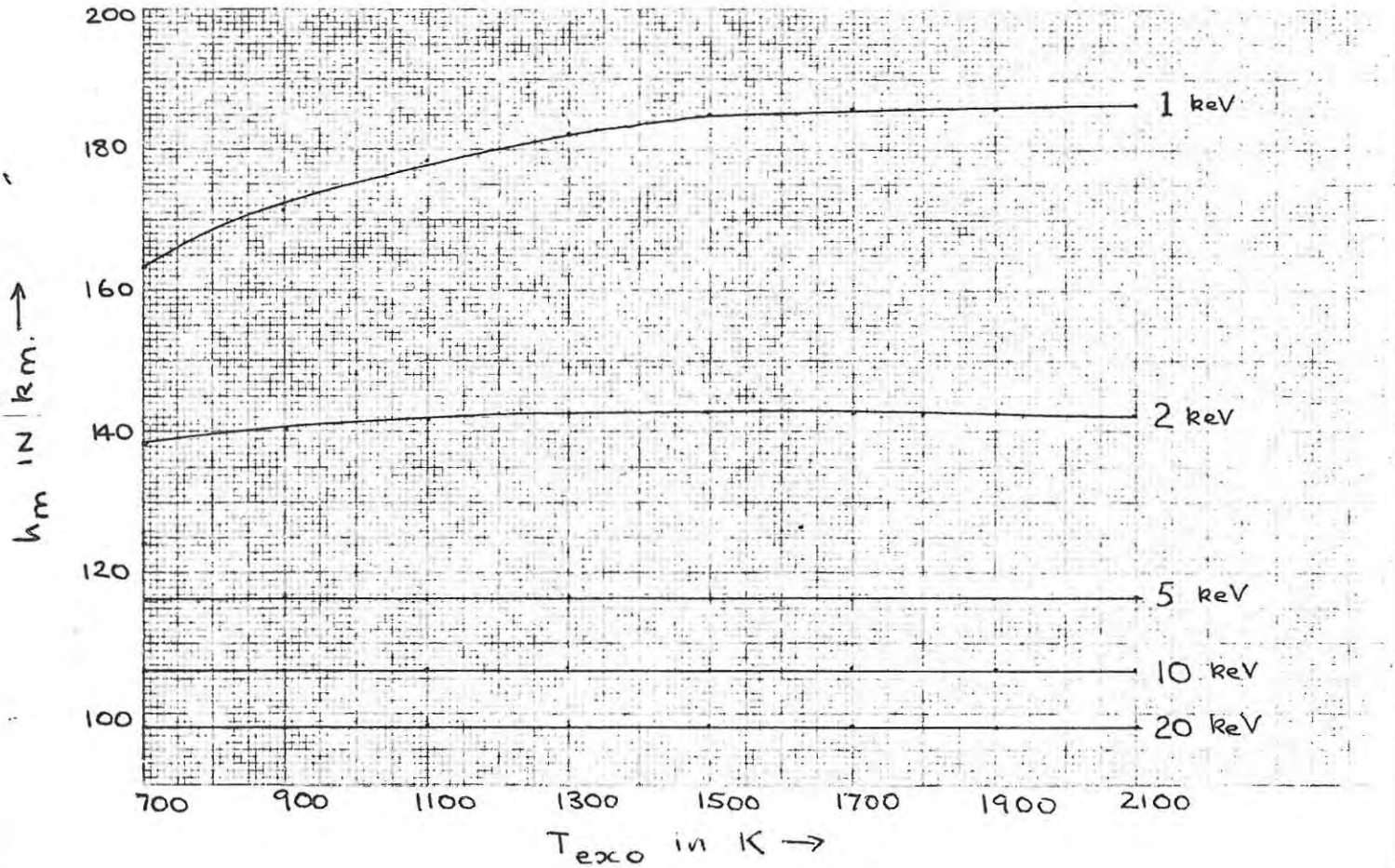

VARIATION OF q_m/F WITH T_{exo}

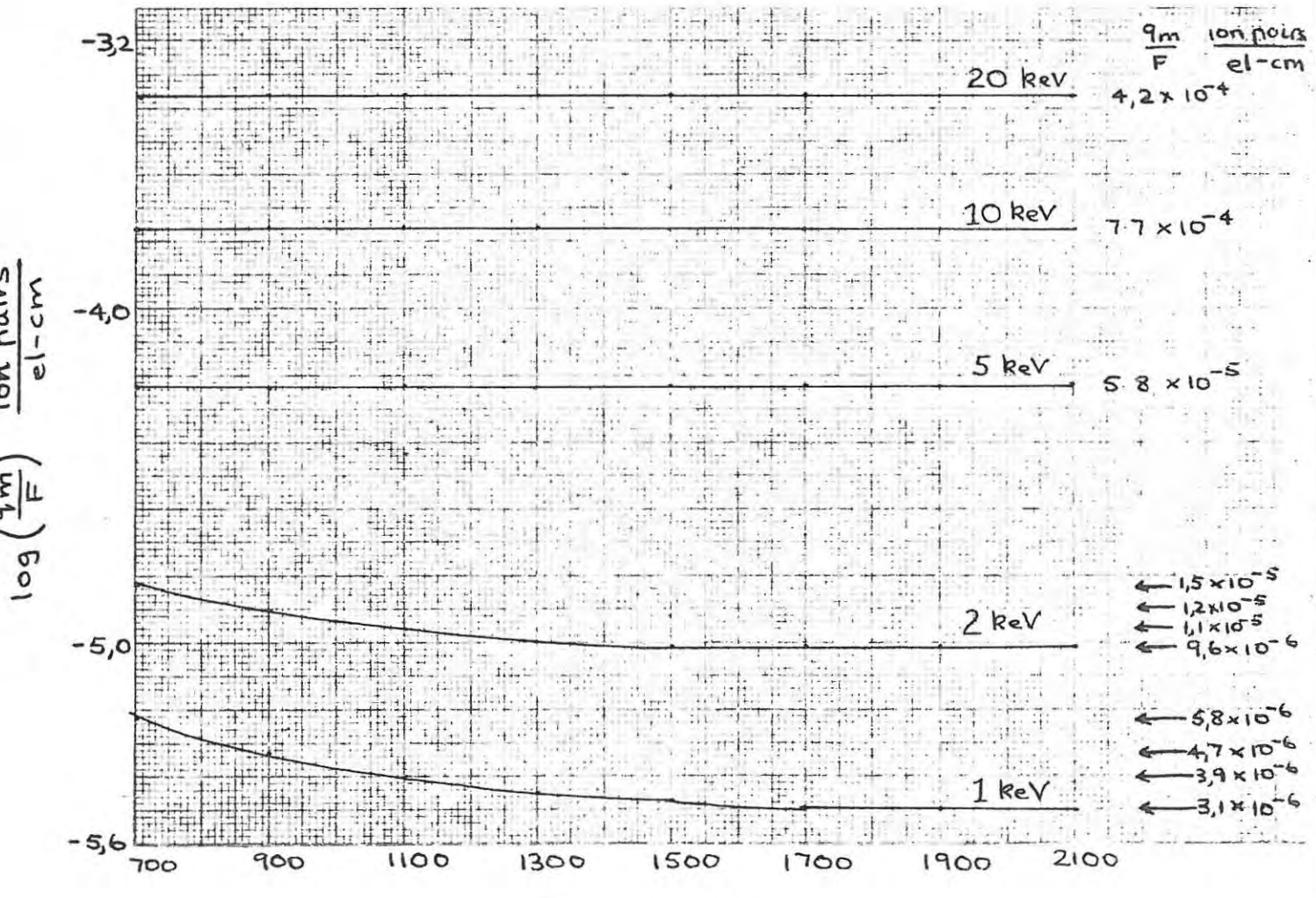

value, which difference would not be possible to see on any ordinary ionogram although the decrease in q_m/F only becomes negligible (i.e. $> 3\%$ which we have chosen as the accuracy of our results because this is the order of the maximum difference between the results of Berger et al and AW18) above 1700 K.

We see for 2 keV electrons that there is negligible difference between h_m in the temperature range 900 to 2100 K while any decrease q_m/F is negligible at temperatures > 1300 K.

For 5, 10 and 20 keV electrons there is no difference in either h_m or q_m/F.

One of our major regions of interest in the ionosphere is the F-layer. Previously it has been generally accepted that ionization produced per unit flux of precipitating electrons in the region above 200 km has been due to low energy electrons (soft spectrum). We notice from Table 4-1 that electrons of 20 keV contribute an amount equal to about 11% of that produced by 1 keV electrons. These percentage contributions are calculated such that the production by 1 keV electrons is taken to be 100. We also note that the percentage contribution is very nearly independent of T_{exo} in the range 700 to 2100 K.

Table 4-1 also gives values of q/F for three heights in the F-region for T_{exo} = 700 K, 900 K, 1100 K, 1300 K, 1500 K, 2100 K.

Table 4-1

Variation of q/F with T_{exo} in the F-region.

T_{exo}	Alt.	q/F (1 keV)		q/F (2 keV)		q/F (5 keV)		q/F (10 keV)		q/F (20 keV)		q/F (50 keV)		q/F (100 keV)	
2100K	280	7,88(-7)	100%	4,74(-7)	60%	2,41(-7)	30%	1,45(-7)	18%	8,66(-8)	11%	4,40(-8)	6%	2,63(-8)	3%
	240	1,46(-6)	100%	9,05(-7)	62%	4,65(-7)	32%	2,79(-7)	19%	1,67(-7)	11%	8,48(-8)	6%	5,08(-8)	3%
	200	2,80(-6)	100%	2,03(-6)	73%	1,06(-6)	38%	6,38(-7)	23%	3,83(-7)	14%	1,94(-7)	7%	1,16(-7)	4%
1500K	280	6,65(-7)	100%	4,01(-7)	60%	2,04(-7)	31%	1,22(-7)	18%	7,31(-8)	11%	3,71(-8)	6%	2,22(-8)	3%
	240	1,37(-6)	100%	8,46(-7)	62%	4,34(-7)	32%	2,60(-7)	19%	1,56(-7)	11%	7,91(-8)	6%	4,74(-8)	3%
	200	2,90(-6)	100%	2,04(-6)	70%	1,07(-6)	37%	6,41(-7)	22%	3,84(-7)	13%	1,95(-7)	7%	1,17(-7)	4%
1300K	280	5,64(-7)	100%	3,39(-7)	60%	1,73(-7)	31%	1,03(-7)	18%	6,19(-8)	11%	3,14(-8)	6%	1,88(-8)	3%
	240	1,25(-6)	100%	7,68(-7)	61%	3,93(-7)	31%	2,36(-7)	19%	1,41(-7)	11%	7,17(-8)	6%	4,29(-8)	3%
	200	2,88(-6)	100%	1,97(-7)	68%	1,03(-6)	36%	6,19(-7)	21%	3,71(-7)	13%	1,88(-7)	7%	1,13(-7)	4%
1100K	280	4,17(-7)	100%	2,51(-7)	60%	1,28(-7)	31%	7,64(-8)	18%	4,57(-8)	11%	2,32(-8)	6%	1,39(-8)	3%
	240	1,03(-6)	100%	6,28(-7)	61%	3,21(-7)	32%	1,92(-7)	19%	1,15(-7)	11%	5,85(-8)	6%	3,50(-8)	3%
	200	2,71(-6)	100%	1,79(-6)	66%	9,31(-7)	34%	5,60(-7)	21%	3,35(-7)	12%	1,70(-7)	6%	1,02(-7)	4%
900K	280	2,52(-7)	100%	1,51(-7)	60%	7,69(-8)	31%	4,61(-8)	18%	2,76(-8)	11%	1,40(-8)	6%	8,39(-9)	3%
	240	7,18(-7)	100%	4,35(-7)	61%	2,22(-7)	31%	1,33(-7)	19%	7,97(-8)	11%	4,04(-8)	6%	2,42(-8)	3%
	200	2,31(-6)	100%	1,47(-6)	64%	7,56(-7)	33%	4,54(-7)	20%	2,72(-7)	12%	1,38(-7)	6%	8,27(-8)	4%
700K	280	1,13(-7)	100%	6,79(-8)	60%	3,45(-8)	31%	2,06(-8)	18%	1,24(-8)	11%	6,27(-9)	6%	3,75(-9)	3%
	240	3,92(-7)	100%	2,36(-7)	60%	1,20(-7)	31%	7,20(-8)	18%	4,31(-8)	11%	2,19(-8)	6%	1,31(-8)	3%
	200	1,65(-6)	100%	1,01(-6)	61%	5,19(-7)	31%	3,11(-7)	19%	1,87(-7)	11%	9,47(-8)	6%	5,67(-8)	3%

Normalization of the ionization rate profiles.

Figures 4-1 to 4-4 show ionization rate profiles for 5 different initial energies and several different values of T_{exo}. These graphs all have the same general shape and this suggests that it may be possible to normalize them so that they may be represented by a single curve.

A similarly shaped curve is that of the Chapman function which represents production due to photoionization. We might then suppose that a similar type of function would describe a normalized ionization rate profile produced by energetic electrons. The Chapman function for normal incidence may be expressed as

$Q = \exp(1 - X - e^{-X})$ where X is a scaled height and if we solve this for $X = 0$ we find $Q = 1$, and for $X = 1$, Q is 0,69.

The curves in Figs. 4-1 to 4-4 were normalized by calculating $Q = \frac{q/F}{q_m/F}$.

The height at which q/F fell to 0,69 q_m/F was denoted by $h_{0,69}$ and H was defined such that

$$H = h_{0,69} - h_m$$

The scaled height was calculated as

$$X = \frac{h - h_m}{H}$$

The values of (X, Q) were plotted for 150 points scattered along the range $X = -1$ to $X = 11$. These points represented the profiles for 1, 2, 5, 10 and 20 keV electrons in model atmospheres whose values of T_{exo} ranged from 900 K by 200 K steps to 2100 K. These points were used as data for a curve fitting program to fit a modified Chapman-type function, namely

$$Q = (1 + aX + bX^2 + cX^3) \exp (1 - X - e^{-X})$$

(I am indebted to James G. Greener for helping me to use this Fortran program HYPE, adopted from the original obtained from the U.S.A.)

The solid line through the x's in Fig 4-6 is the theoretical curve which fits the expression

$$Q = (1 + 0{,}109\ X - 0{,}155X^2 + 0{,}078X^3) \exp (1 - X - e^{-X}) \qquad (4\text{-}2)$$

This normalized curve or the equation (4-2) provide us with a means of rapidly computing ionization rate profiles as long as q_m/F, h_m and H are known. The first two may be found from Fig 4-5 for any T_{exo} from 700 K to 2100 K. Fig 4-7 is a plot of H vs T_{exo} for the energies 1, 2, 5, 10 and 20 keV. The value of H could only be read to within 1 km and the points are plotted with error bars. The smooth curves drawn through the experimental values of H may be used for determining a likely value of H for 1, 2, 5, 10 and 20 keV electrons in the range 700 to 2100 K. The values of H_1 at 900 and 1100 K do not fall on the smooth curve. It is possible that the values of h_m and/or q_m/F were inaccurate by more than 1 km for these two values of T_{exo}.

Use of the normalized curve.

The following is a procedure for calculating ionization rate profiles using the normalized curve.

1. Determination of T_{exo}.
(following a slightly modified method of Jacchia (1965)).

To find T_{exo} for any particular event the following must be known.

φ° = latitude of station
δ° = declination of the sun
d = day number (running from 1 for January 1st to 365 for Dec. 31st.)
a_p = geomagnetic activity index
H = hour angle in degrees
$F_{10,7}$ = 10,7 cm solar flux
$\overline{F}_{10,7}$ = five monthly average 10,7 cm solar flux.

These may be used in Program Jacchia (Appendix 4) or used in the following formulae (from Jacchia (1965))

$$\eta = \tfrac{1}{2}(\varphi - \delta)$$

$$\theta = \tfrac{1}{2}(\varphi + \delta)$$

$$\tau/2 = \left(\frac{H - 45^{\circ} + 12^{\circ} \sin (H + 45^{\circ})}{2}\right)$$

$$\Delta T = 1{,}0^{\circ}\, a_p + 125^{\circ}\, (1 - \exp(-0{,}08)\, a_p)$$

$$T_o = 418^{\circ} + 1{,}8^{\circ}\, F_{10,7} + 1{,}8^{\circ}\, \overline{F}_{10,7} + (0{,}37 + 0{,}14 \sin 2\pi \frac{d - 151}{365})\, \overline{F}_{10,7} \sin 4\pi \left(\frac{d - 59}{365}\right)$$

$$T_{exo} = T_o\, (1 + 0{,}28 \sin^{1,25}\theta)\, (1 + 0{,}28 \left(\frac{\cos^{1,25}\eta - \sin^{1,25}\theta}{1 + 0{,}28 \sin^{1,25}\theta} \cos^{2,5}\frac{\tau}{2}\right) + \Delta T$$

(Note: We have used 1,25 in $\sin^{1,25}\theta$ etc. from Jacchia and Slowey (1967) rather than 2,5 as published by Jacchia (1965)).

2. Having found T_{exo}, q_m/F and h_m may be read from Fig. 4-5 and H may be read from Fig. 4-7.

3. Pairs of X and Q may be found from Fig. 4-6 and $h = XH = h_m$ and $q/F = Q\, q_m/F$ calculated.

The ionization rate profile may now be plotted.

This method provides a rapid means of calculating approximate ionization rate profiles without the use of computers. The reliability may be assessed from Fig. 4-6.

FIG. 4-6

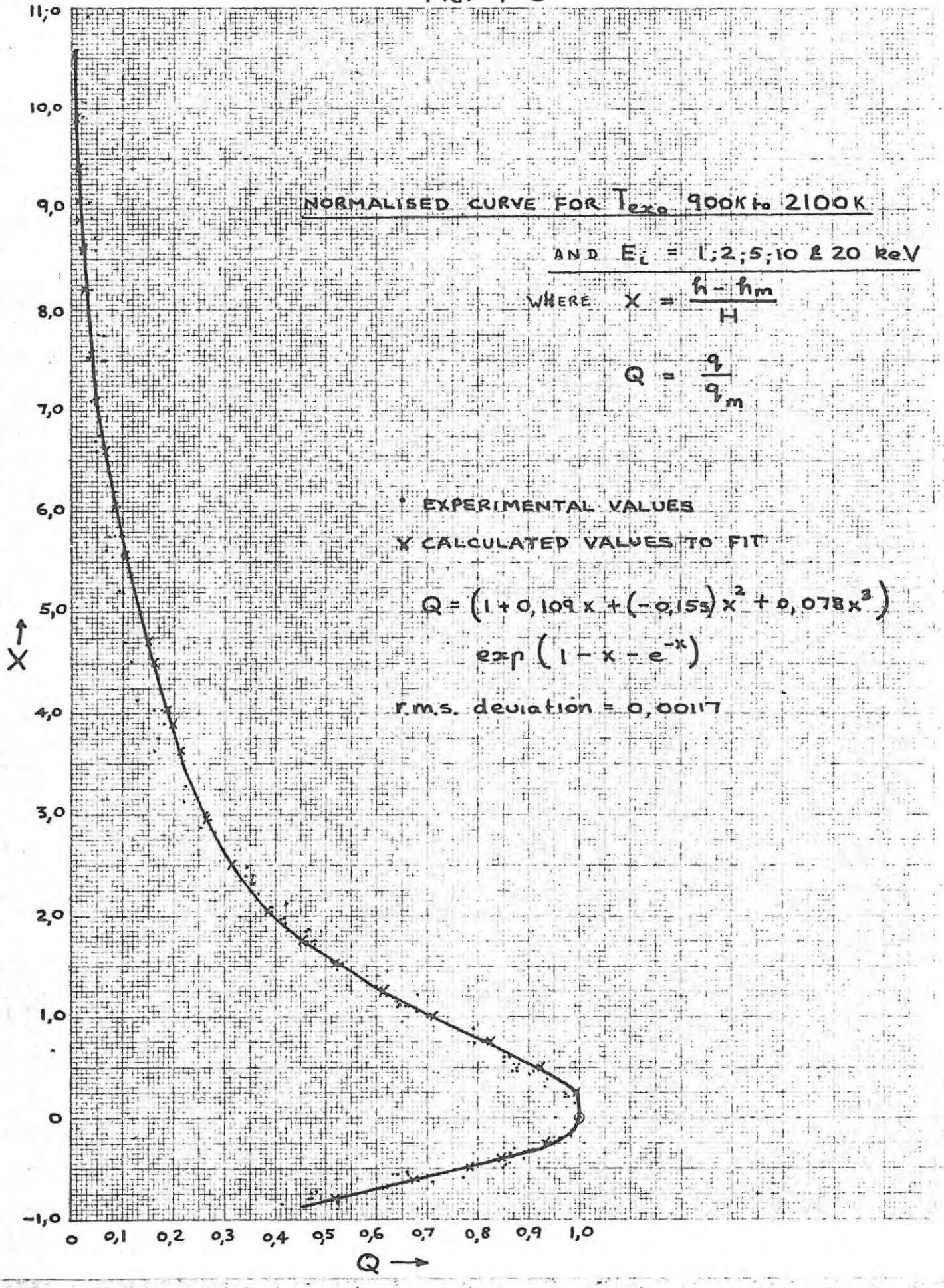
NORMALISED CURVE FOR T_{ex} 900K to 2100K
AND E_i = 1;2;5;10 & 20 keV
WHERE $X = \frac{h - h_m}{H}$
$Q = \frac{q}{q_m}$
EXPERIMENTAL VALUES
CALCULATED VALUES TO FIT
$Q = \left(1 + 0,109x + (-0,155)x^2 + 0,078x^3\right) \exp\left(1 - x - e^{-x}\right)$
r.m.s. deviation = 0,00117
X
Q
11;0
10,0
9,0
8,0
7,0
6,0
5,0
4,0
3,0
2,0
1,0
0
-1,0
0 0,1 0,2 0,3 0,4 0,5 0,6 0,7 0,8 0,9 1,0

Chapter 5 The Effect of Different Dip Angles

Stations at different latitudes often have different values of I, the dip angle of the magnetic field. We are interested in the difference introduced in the ionization rate profile when we change the dip angle through the values -90° to -30°. (The negative signs denote that we are considering conditions in the southern hemisphere but is irrelevant in so far as the interpretation of the results is concerned.) We do not consider $I < 30^{\circ}$ because in this thesis we are not interested in the possible precipitation of electrons near the geomagnetic equator.

The main effect of changing the dip angle is to increase the distance travelled in any lamination by the precipitating electrons. As we have seen in Chapter 3 this means that more energy is lost in the lamination but less is deposited at the height level in which we are interested. This explains the shape of the ionization rate profiles shown in Fig. 5-1 to 5-4. At first sight it appears that less than the total incident energy is lost when $I \neq 90^{\circ}$. However, we are looking at the vertical distribution in height and if we were to integrate the energy loss along the direction of the field with dip angle I we should obtain the correct total incident energy.

Differences between the ionization rates for dip angle from -90° to -30° became significant at the following altitudes and below

E_i	Altitude above which differences $< 3\%$
1 keV	240 km
2 keV	200 km
5 keV	150 km
10 keV	130 km
20 keV	110 km

Note that the dip angle does not appreciably influence the ionization rate in the F2-region except perhaps for 1 keV electrons while the ionization rate in the F1-region is influenced by changing the dip angle in the case of energies of 5 keV and less.

VARIATION WITH DIP ANGLE

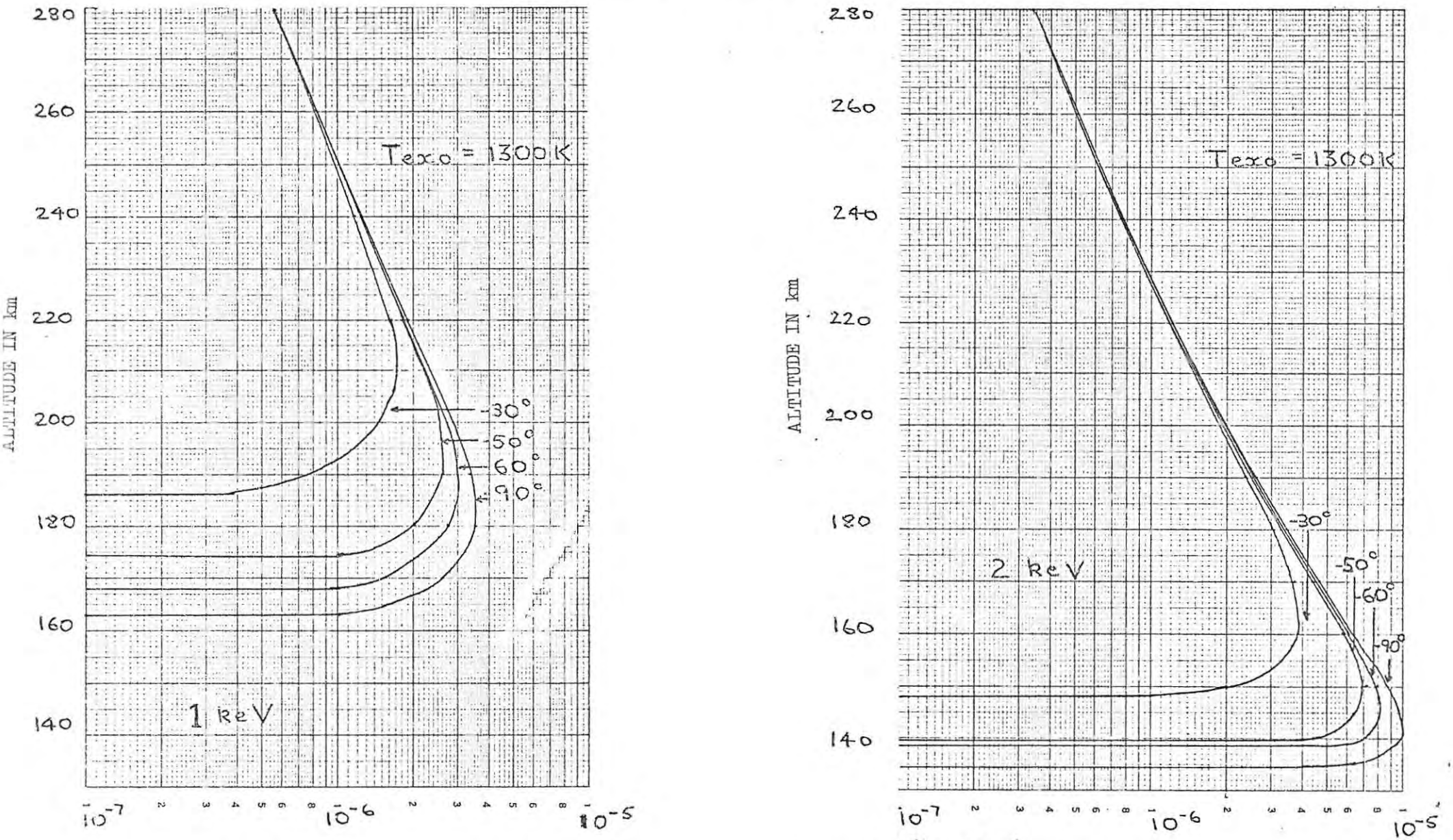

IONIZATION RATE PER UNIT FLUX $\frac{q}{F}$ $\left(\frac{\text{ion pairs}}{\text{el-cm}}\right)$

FIG. 5-1

VARIATION WITH DIP ANGLE

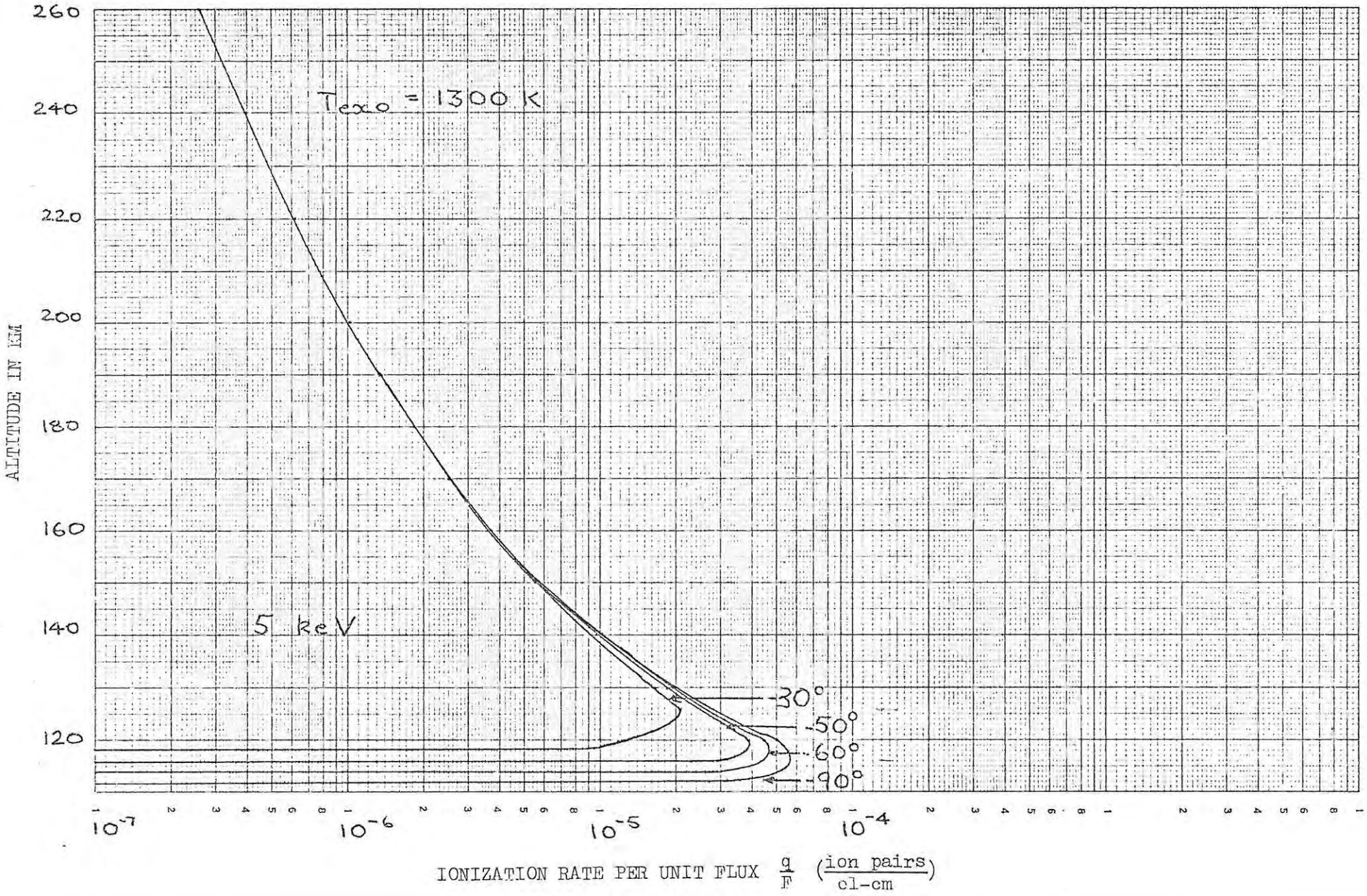

FIG. 5-2

FIG. 5-3

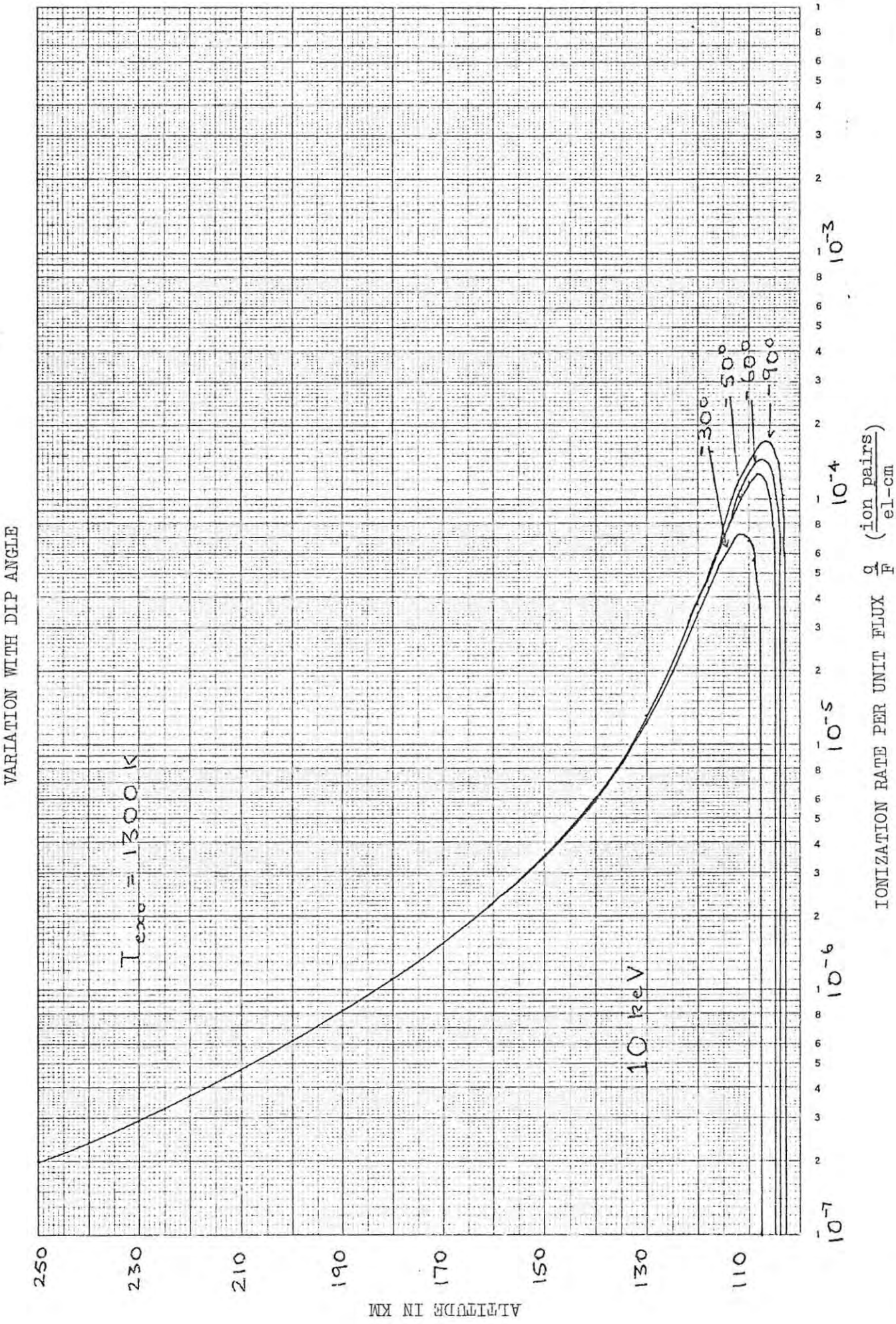
VARIATION WITH DIP ANGLE
$T_{exo} = 1300$ K
10 keV
-30°
-50°
-60°
-90°
ALTITUDE IN KM
250
230
210
190
170
150
130
110
IONIZATION RATE PER UNIT FLUX $\frac{q}{F}$ ($\frac{\text{ion pairs}}{\text{el-cm}}$)
10^{-3}
10^{-4}
10^{-5}
10^{-6}
10^{-7}

FIG. 5-4

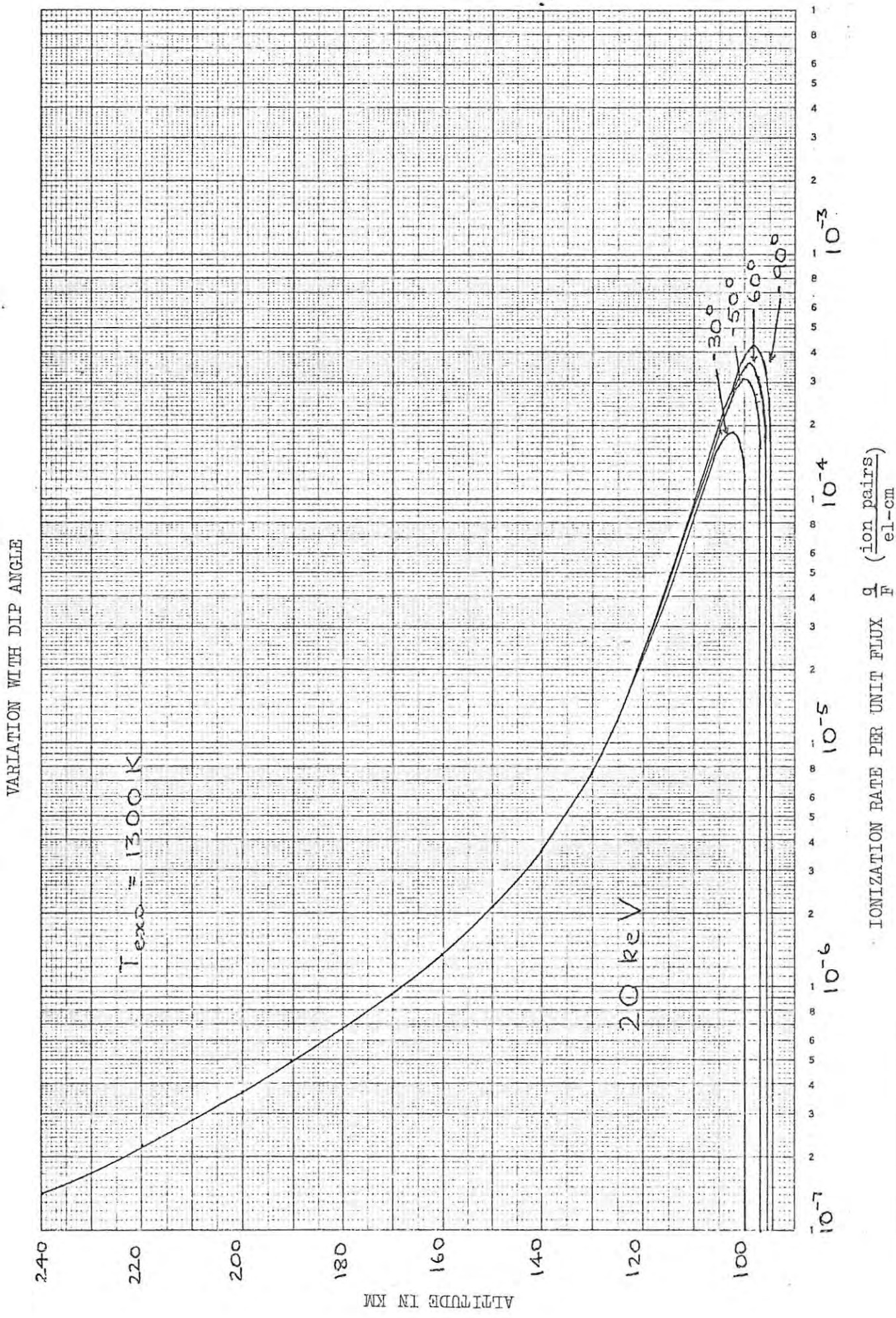
VARIATION WITH DIP ANGLE
T_{exo} = 1300 K
20 keV
-30°
-15°
60°
90°
ALTITUDE IN KM
240
220
200
180
160
140
120
100
IONIZATION RATE PER UNIT FLUX $\frac{q}{F}$ ($\frac{\text{ion pairs}}{\text{el-cm}}$)
10^{-3}
10^{-4}
10^{-5}
10^{-6}
10^{-7}

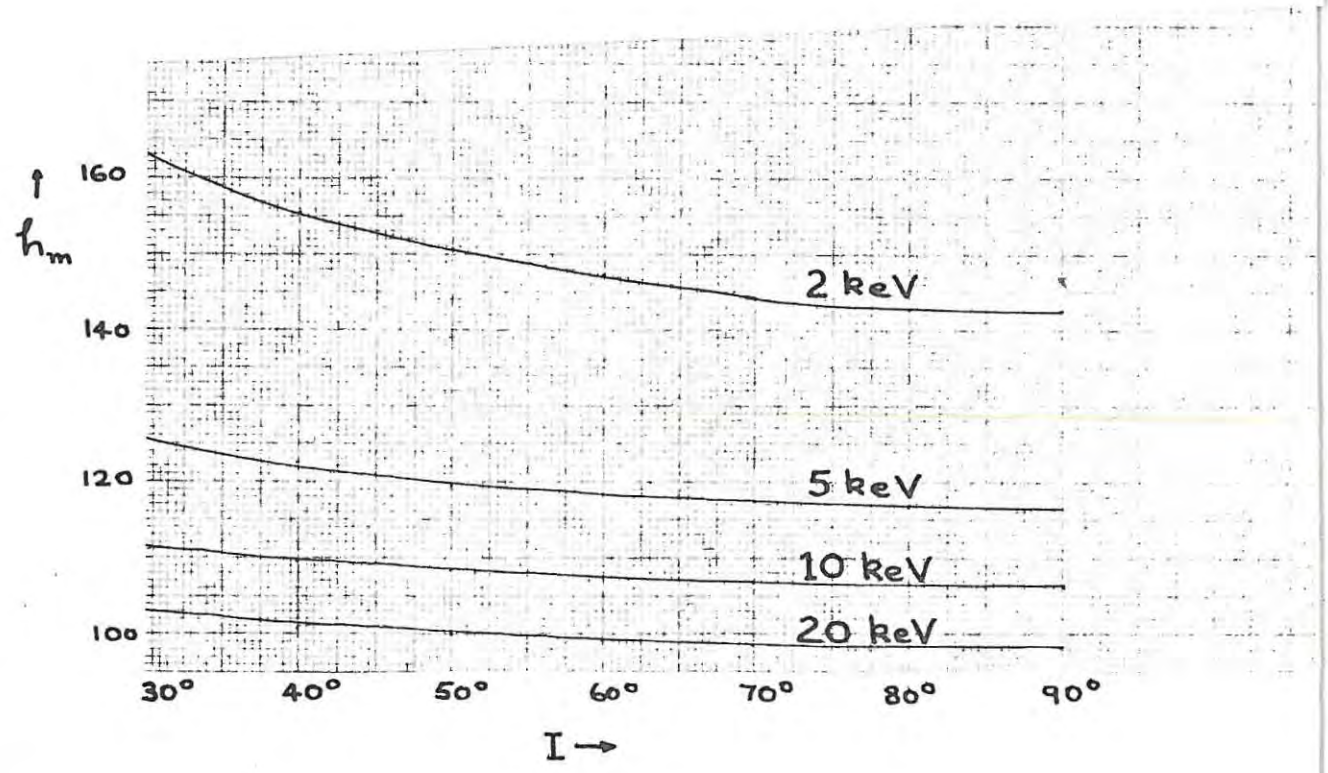

VARIATION OF LOG q_m/F WITH DIP ANGLE

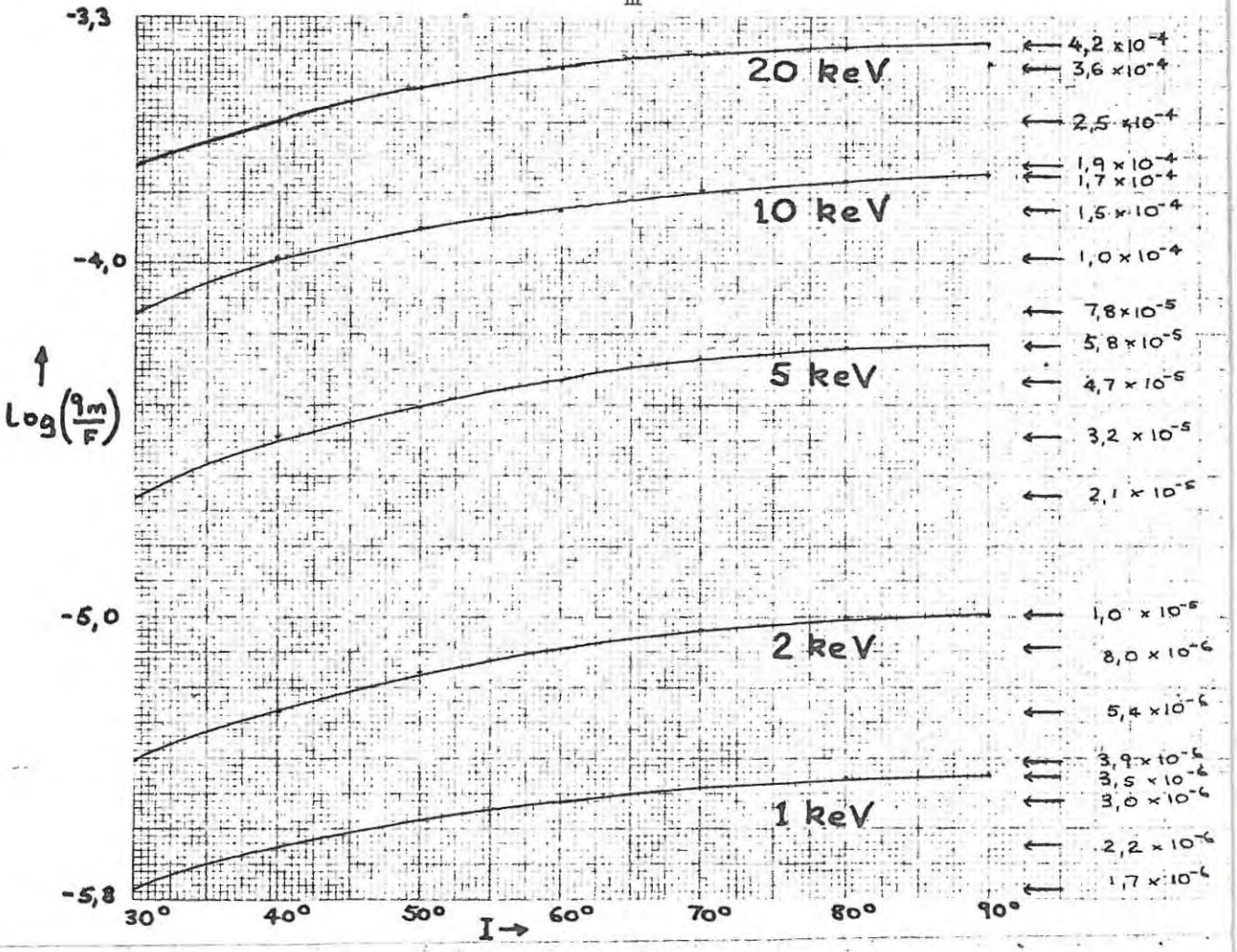

Variation of hm and q_m/F with dip angle are shown in Fig 5-5. We see that for all energies in the range 1-20 keV hm increases for decreasing values of I but the increase is greatest for lower energy electrons e.g. when the dip angle changes from -90^o to -30^o we find that hm increases by 29 km for 1 keV electrons but only by 5 km for 20 keV electrons. The decrease in q_m/F is typically of the order of 60% for the same range in I.

We are most interested in the results of $I = -60^o$ which is close to the value of I (ground) at Sanae ($-62,6^o$ WDCA 1971). Comparing values obtained for $I = -60^o$ with those of $I = -90^o$ will give us some indication of the error involved when we apply results for vertical incidence at the pole to Sanae. We find that for 1 keV electrons the increase in hm from -90^o to -60^o is small (about 5 km) while the estimation of q_m/F can be up to 20% greater than would be the case for $I = 60^o$.

Practically all previous workers have applied results calculated for vertical incidence at the pole for studies of auroral-type phenomena (e.g. Jacobs, Kist and Rawer (1969)). In Antarctica we find that I may be as small as -56^c (Decepcion Island) and this means that the maximum ionization rate (q_m/F) can be up to 25% less than the value for vertical incidence while hm could have shifted upwards by as much as 8 km.

Note that all calculations of ionization rate profiles have assumed that I remains constant throughout the region 100 - 300 km. This is not strictly true but the changes in I in this region are about 1^o and this has a negligible effect on the results.

Chapter 6 Stations at Different Latitudes.

The geographic latitude is one of the parameters which affects the value of T_{exo}. Since some stations of the same geographic latitude have a different value for the magnetic dip angle I, we have chosen several specific stations in the Southern Hemisphere (ranging in latitude from -90^{o} to $-19,2^{o}$) for determining what the ionization rate rate profile looks like when we are at different geographic latitudes.

The following stations were chosen:

Station	latitude	dip angle I_G	T_{exo}
South Pole	-90^{o}	$-74,2^{o}$	1244K
Halley Bay	$-75,5^{o}$	$-64,3^{o}$	1264K
Sanae	$-70,3^{o}$	$-62,6^{o}$	1270K
Port Stanley	$-51,7^{o}$	$-47,5^{o}$	1289K
Marion Island	$-46,9^{o}$	$-63,3^{o}$	1293K
Cape Town	$-34,2^{o}$	$-65,7^{o}$	1301K
Tsumeb	$-19,2^{o}$	$-57,3^{o}$	1307K

The T_{exo} for the model atmosphere for each station was found by varying the latitude only in Program Jacchia (appendix 4). All other parameters were kept constant viz:

Hour angle 0^{o}, Declination 0^{o}, Day 80, $F_{10,7} = 150$, $F_{10,7} = 150$, $a_p = 11$. This means that we have calculated the model atmosphere at midday on the 21st March (equinox) under conditions of mean solar activity (denoted by $F_{10,7} = 150$) and mean geomagnetic activity (denoted by $a_p = 11$).

Figs. 6-1 to 6-4 show ionization rate profiles for four stations (South Pole, Sanae, Port Stanley and Tsumeb).

We immediately see that the dip angle has more influence than the latitude correction in the model atmosphere by virtue of the fact that there is greater separation between the profiles around the peak than at altitudes above 200 km where the model atmosphere plays a more important part.

IONIZATION RATE PROFILES FOR DIFFERENT STATIONS

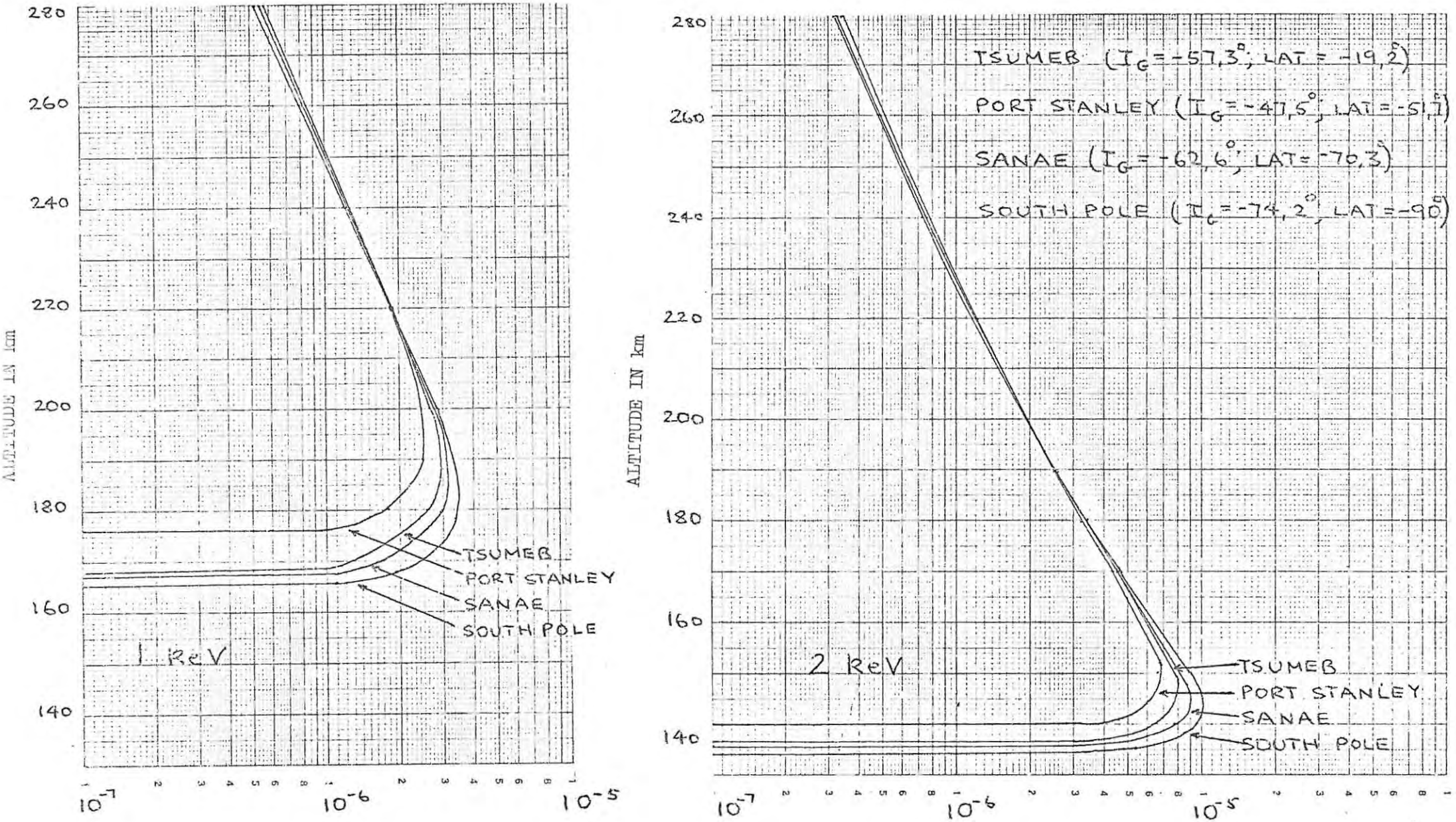

IONIZATION RATE PER UNIT FLUX $\frac{q}{F}$ $\left(\frac{\text{ion pairs}}{\text{el-cm}}\right)$

FIG. 6-1

IONIZATION RATE PROFILES FOR DIFFERENT STATIONS

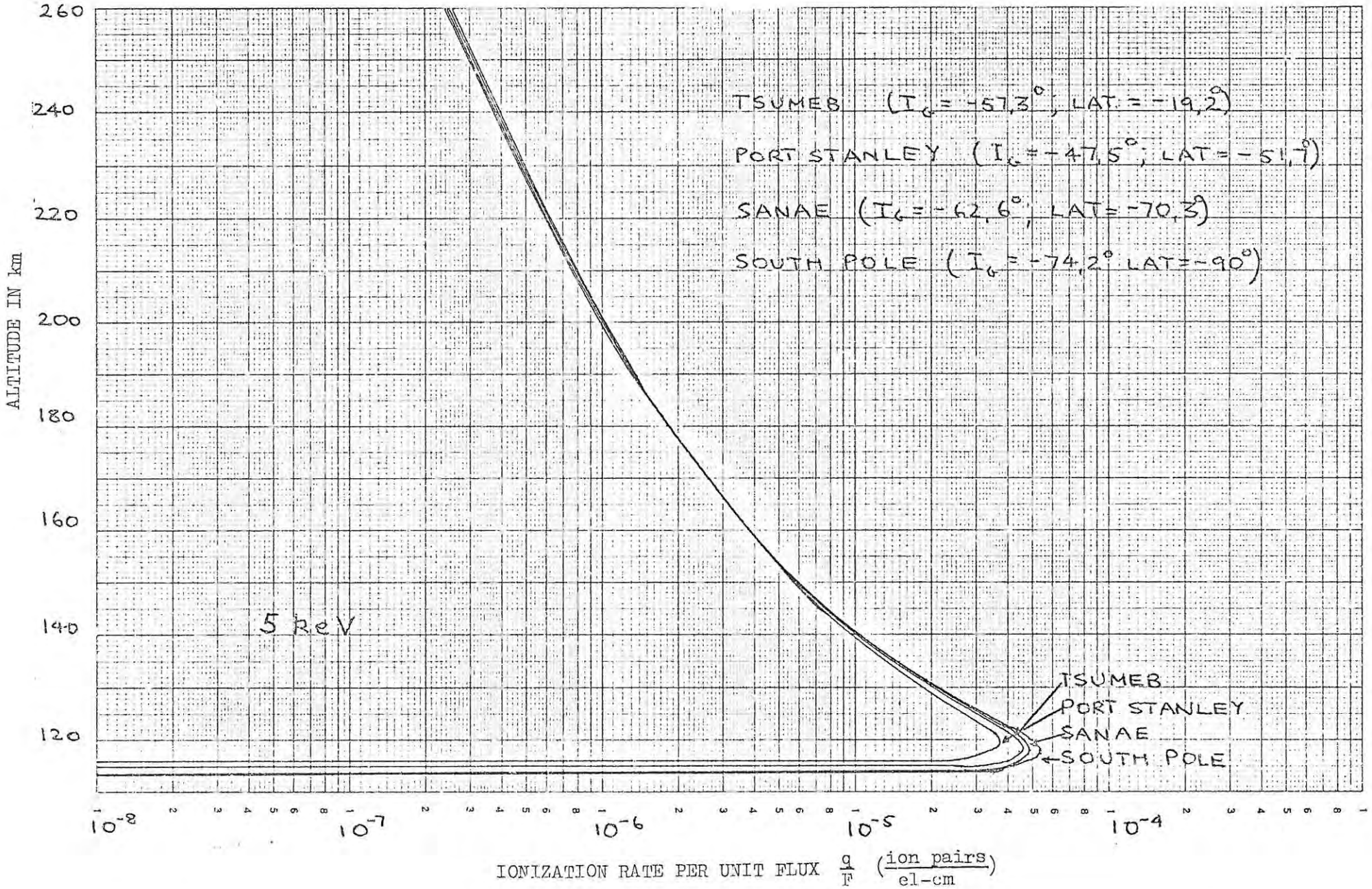

FIG 6-2

IONIZATION RATE PROFILES FOR DIFFERENT STATIONS

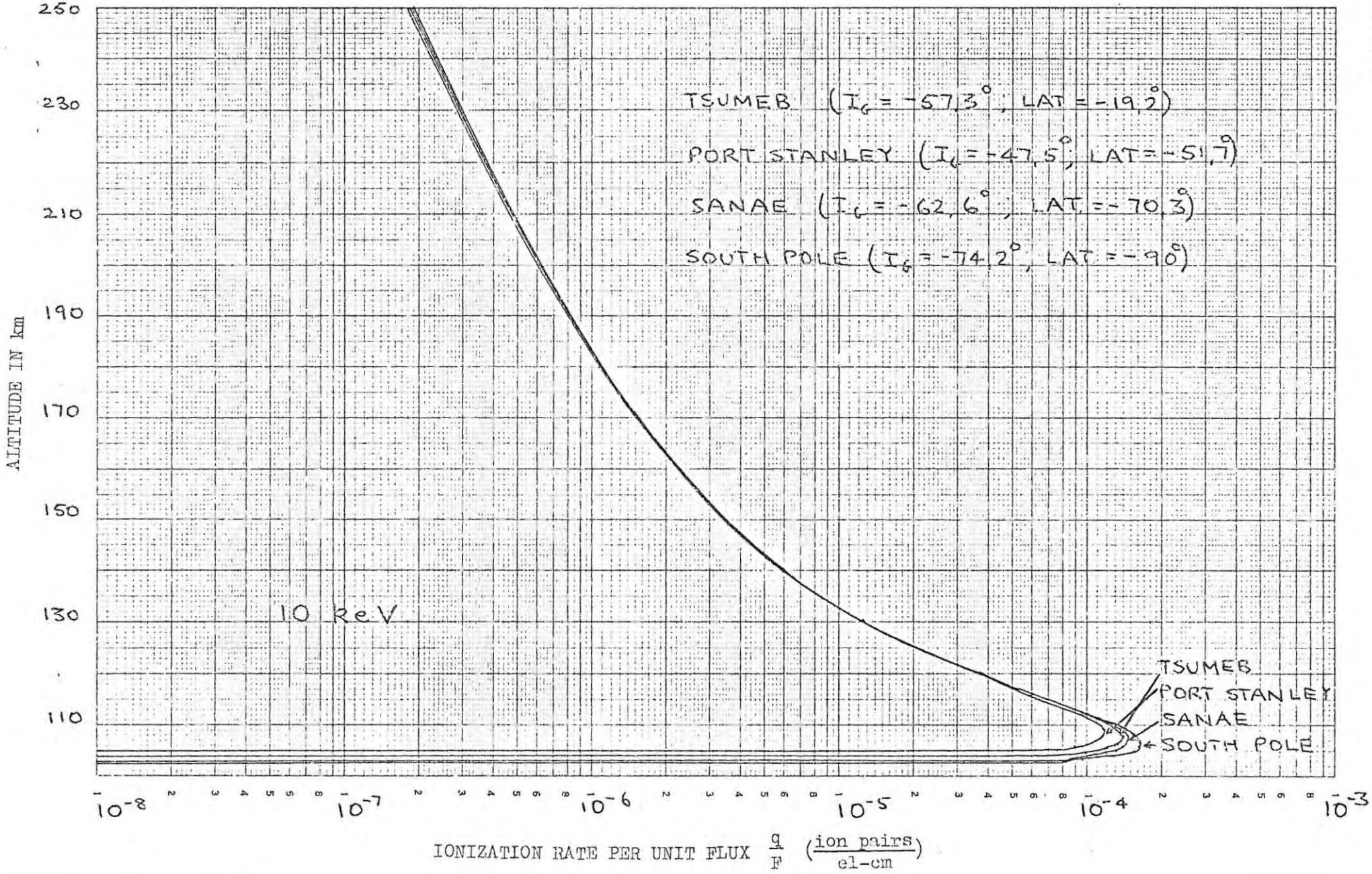

FIG. 6-3

IONIZATION RATE PROFILES FOR DIFFERENT STATIONS

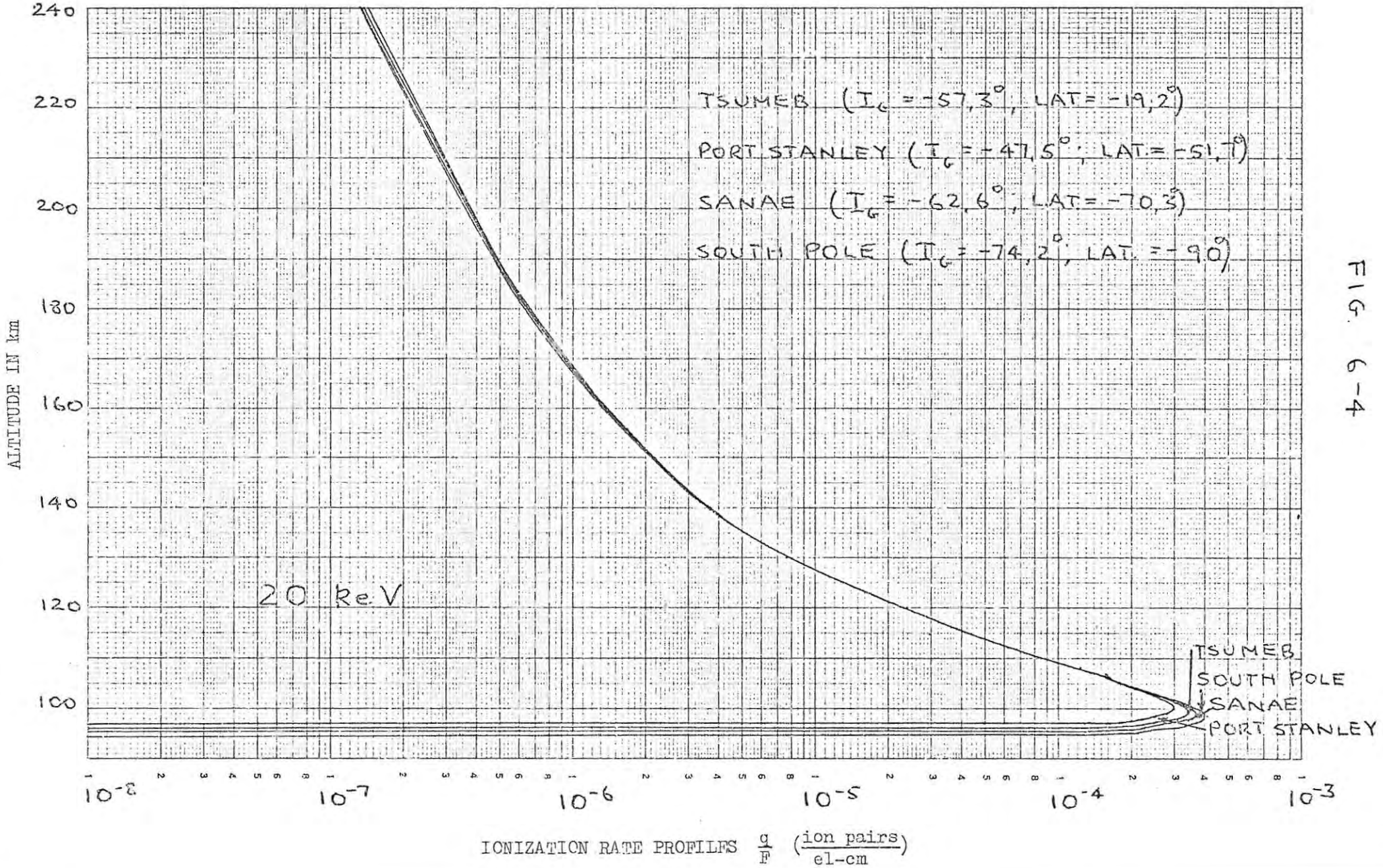

FIG. 6-4

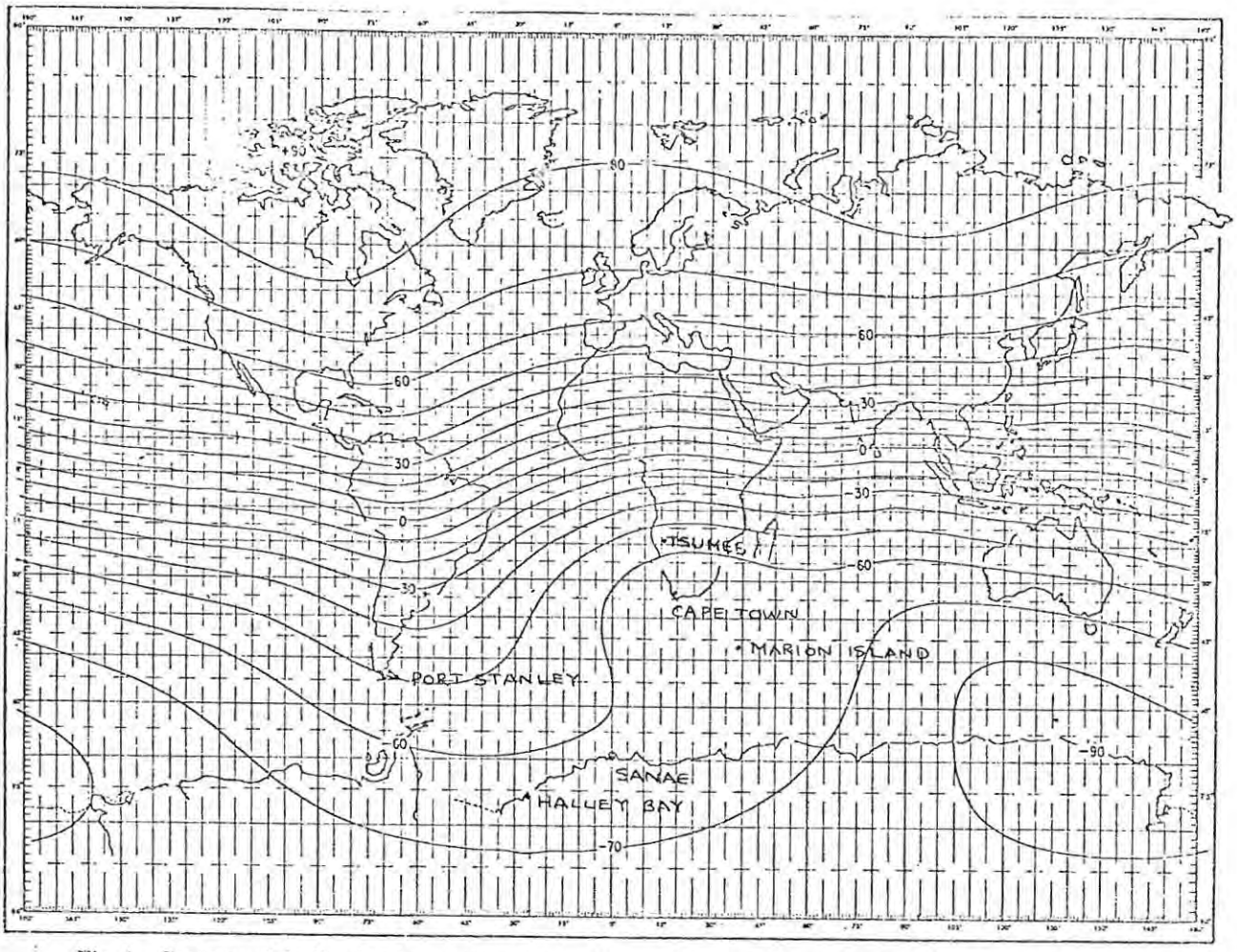

Fig. 4. Contours of inclination from same spherical harmonic expansion as Figure 1 (contour interval 10°).

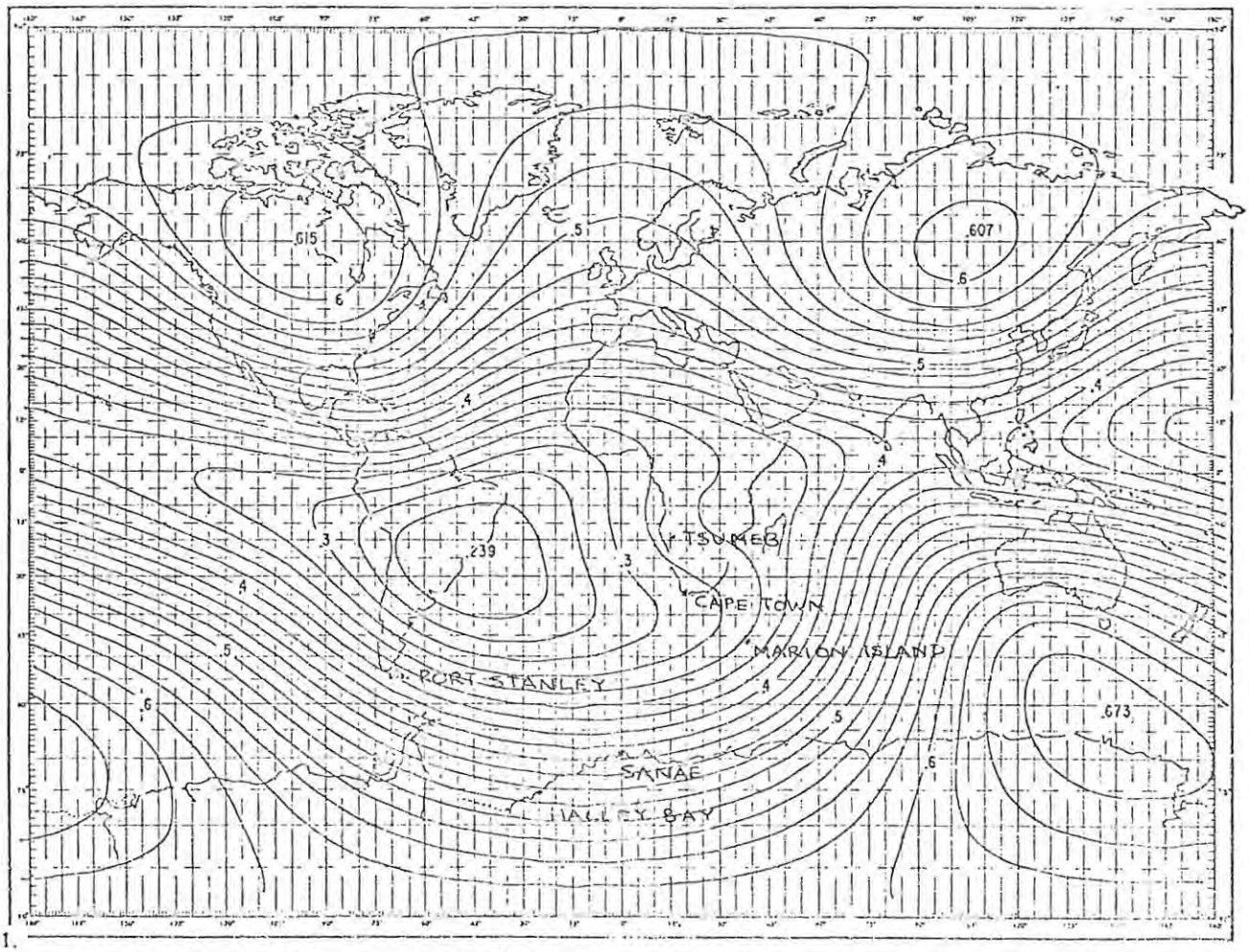

Fig. 1.

Contours of the total intensity of the geomagnetic field in gauss, synthesized from a set of 48 spherical harmonic coefficients [*Jensen and Cain*, 1962] for epoch of 1960.0 (contour interval 0.02 gauss). All centers are highs except the 0.239 over South America.

This is the reason why Port Stanley (T_{exo} = 1289 K, I_G = - 47,5°) peaks at a greater altitude than Tsumeb (T_{exo} = 1307K, I_G = -57,3°).

This is also borne out by comparing values of h_m and q_m/F in table 6-1 for stations with similar dip angles but different latitudes and hence T_{exo} e.g. Marion Island and Sanae. These two stations differ in latitude by approximately 23° (and in T_{exo} by 23 K) but in dip angle by only 0,7°. We see that differences in h_m and q_m/F for the two stations are negligible.

The same is true of Halley Bay and Cape Town whose difference in latitude is even larger (approximately 42° which gives us a difference in T_{exo} of 49°) but whose dip angles differ by 1,4°.

It is indeed surprising as well as interesting to find that Halley Bay and Cape Town should have such similar values for the dip angle I_G, especially if we remember that Halley Bay is situated on the Weddell Sea in Antarctica and Cape Town is a midlatitude city lying on the tip of the African Continent. The reason for this similarity in dip angle is the South Atlantic Geomagnetic Anomaly which has the effect of giving some high latitude stations in Antarctica such as Halley Bay and Sanae and Decepcion Island values of dip angle which are close to those normally found at mid latitude stations. Fig. 4 from Cain and Neilon (1963) shows contours of constant inclination (or dip angle).

This figure is reproduced on the opposite page together with their Fig. 1 (contours of total intensity of the magnetic field).

The approximate positions of Halley Bay, Sanae, Port Stanley, Marion Island, Cape Town and Tsumeb are plotted on Fig. 4. We see that Halley Bay, Sanae, Marion Island and Cape Town all fall within the strip bounded by I = -60° and I = -70°. We also see that Port Stanley (latitude -52°) falls on a contour of lower I than Tsumeb (latitude -52°) falls on a contour of lower I than Tsumeb (latitude -19°) and this is obviously also a result of the South Atlantic Geomagnetic Anomaly.

h_m for stations at different latitudes

Station / E_i	South Pole	Halley Bay	Sanae	Port Stanley	Marion Island	Cape Town	Tsumeb
1keV	182,8	185,8	186,6	194,5	186,9	186,2	190,2
2keV	143,2	145,2	146,0	151,2	145,9	145,1	148,0
5keV	117,1	117,7	117,9	120,0	117,8	117,6	118,7
10keV	106,6	107,2	107,3	108,7	107,2	107,1	107,7
20keV	98,5	98,9	99,0	100,0	99,0	98,9	99,3

q_m/F for stations at different latitudes

Station / E_i	South Pole	Halley Bay	Sanae	Port Stanley	Marion Island	Cape Town	Tsumeb
1keV	3,48(-6)	3,19(-6)	3,13(-6)	2,54(-6)	3,13(-6)	3,18(-6)	2,93(-6)
2keV	9,74(-6)	8,69(-6)	8,40(-6)	6,65(-6)	8,41(-6)	8,61(-6)	7,82(-6)
5keV	5,51(-5)	5,00(-5)	4,89(-5)	3,75(-5)	4,94(-5)	5,09(-5)	4,54(-5)
10keV	1,64(-4)	1,52(-4)	1,50(-4)	1,20(-4)	1,51(-4)	1,54(-4)	1,41(-4)
20keV	3,98(-4)	3,74(-4)	3,68(-4)	3,00(-4)	3,70(-4)	3,78(-4)	3,45(-4)

Table 6-1

Note that we have used the value of I at ground as given in WDCA (1971) for each of the stations and have assumed that this value remains constant from ground to 300 km. This is not strictly true but if we calculate ionization rate profiles for I_{100} to I_{300} (calculated from STP4 notes which gives values of I_G and I_{400}) we find that the maximum rate of ionization does not differ by more than 2% which is well within our 3% limit of accuracy.

In conclusion we note that the ionization rate profiles do change for different stations and that the dip angle has a greater influence on the profile than the latitude correction for temperature.

Chapter 7 Sanae - A Special Study

Since we at Rhodes University are most interested in the effects of precipitating electrons over Sanae, we have chosen this station for studying the effect of changing the parameters which affect the exospheric temperature of the atmospheric model, namely, the hour angle of the sun, the season, the 10,7 cm solar flux $F_{10,7}$ and the geomagnetic activity index a_p. T_{exo} was calculated from these parameters following a slightly modified version of Jacchia's method (Appendix 4). The values chosen as standard for the input data were hour angle = 0^o (midday), geographic latitude = $-70,3^o$ (Sanae), declination of the sun = 0^o and day number = 80 (corresponding to the autumn equinox 21st March), $F_{10,7}$ (the daily value of 10,7 cm solar flux) and $\overline{F}_{10,7}$ (the five monthly average value of the 10,7 cm solar flux) were chosen to be 150 corresponding to average solar flux conditions. (The units of $F_{10,7}$ are 10^{22} W/m^2 but as we are using the values of flux adjusted to 1 A.U., S_a we will refer to the flux of 150 x $10^{22} W/m^2$ as $F_{10,7} = 150$). a_p was chosen to have the average daily value of 11. Each of these parameters was varied in turn keeping the others constant at the standard when the influence of a particular parameter was being studied.

1. The hour angle was varied through 0^{o}, 30^{o}, 90^{o} and 120^{o} corresponding to 1200 h, 1400 h, 1800 h and 0400 h respectively. The T_{exo}'s for the different hour angles are

Hour angle	T_{exo}
0^{o} (1200 h)	1270 K
30^{o} (1400 h) maximum	1279 K
90^{o} (1800 h)	1261 K
-120^{o} (0400 h) minimum	1204 K

We see that the maximum temperature difference involved is 75 K representing a 4% difference in T_{exo}. The ionization rate profiles were calculated for the appropriate model atmospheres and the results may be seen in Fig. 7-1 to 7-4. Only the profiles for 0400 h and 1400 h were plotted as those for 1200 h and 1800 h lay between these two limits.

Table 7-1 gives values for h_m and q_m/F for the different hour angles. We find that differences in h_m are negligible, being of the order of 2 km which is less than the accuracy to which most ordinary ionograms can be scaled. Differences in q_m/F are also negligible, being of the order of 3% or less and this is within the accuracy limit we have chosen.

Table 7-2 shows values of q/F for the few profiles at selected altitudes in the F-region. We see that for all energies in the range 1-20 keV the maximum difference is 10% at 280 km dropping to 6% at 240 km and 3% at 200 km.

Table 7-1

h_m vs hour angle at Sanae

hour angle / E_i	0°(1200h)	30°(1400h)	90°(1800h)	-120°(0400h)
1 keV	186,6	186,9	186,4	184,9
2 keV	146,0	146,0	145,9	145,6
5 keV	117,9	117,9	117,9	117,9
10 keV	107,3	107,3	107,3	107,3
20 keV	99,0	99,0	99,0	99,0

q_m/F vs hour angle at Sanae

hour angle / E_i	0°(1200h)	30°(1400h)	90°(1800h)	-120°(0400h)
1 keV	3,13(-6)	3,12(-6)	3,14(-6)	3,23(-6)
2 keV	8,40(-6)	8,37(-6)	8,42(-6)	8,58(-6)
5 keV	4,89(-5)	4,89(-5)	4,89(-5)	4,89(-5)
10 keV	1,50(-4)	1,50(-4)	1,50(-4)	1,50(-4)
20 keV	3,68(-4)	3,68(-4)	3,68(-4)	3,68(-4)

Table 7-2

Variation of q/F with hour of day in the F-region

E_i	Alt. (km)	q/F (1200h)	q/F (1400h)	q/F (1800h)	q/F (0400h)
1 keV	280	5,44(-7)	5,50(-7)	5,38(-7)	4,98(-7)
	240	1,22(-6)	1,23(-6)	1,21(-6)	1,15(-6)
	200	2,76(-6)	2,76(-6)	2,75(-6)	2,73(-6)
2 keV	280	3,27(-7)	3,31(-7)	3,24(-7)	3,00(-7)
	240	7,50(-7)	7,55(-7)	7,45(-7)	7,08(-7)
	200	1,95(-6)	1,95(-6)	1,94(-6)	1,90(-6)
5 keV	280	1,67(-7)	1,68(-7)	1,65(-7)	1,52(-7)
	240	3,84(-7)	3,87(-7)	3,82(-7)	3,63(-7)
	200	1,02(-6)	1,02(-6)	1,01(-6)	9,90(-7)
10 keV	280	9,98(-8)	1,01(-7)	9,87(-8)	9,13(-8)
	240	2,31(-7)	2,32(-7)	2,29(-7)	2,17(-7)
	200	6,12(-7)	6,14(-7)	6,10(-7)	5,96(-7)
20 keV	280	5,97(-8)	6,04(-8)	5,91(-8)	5,47(-8)
	240	1,38(-7)	1,39(-7)	1,37(-7)	1,30(-7)
	200	3,67(-7)	3,68(-7)	3,66(-7)	3,57(-7)

VARIATION WITH HOUR OF DAY

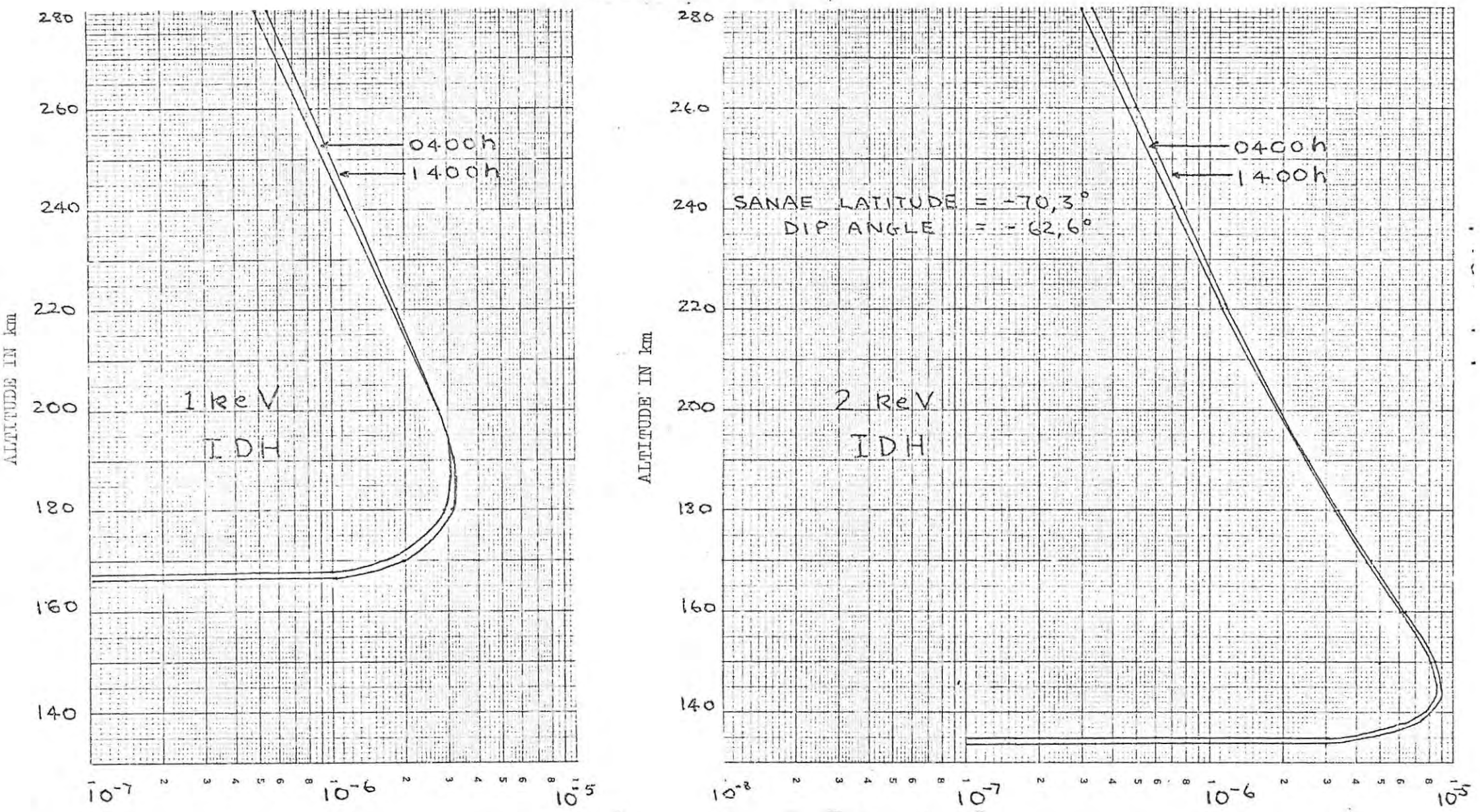

IONIZATION RATE PER UNIT FLUX $\frac{q}{F}$ $\left(\frac{\text{ion pairs}}{\text{el-cm}}\right)$

FIG. 7-2

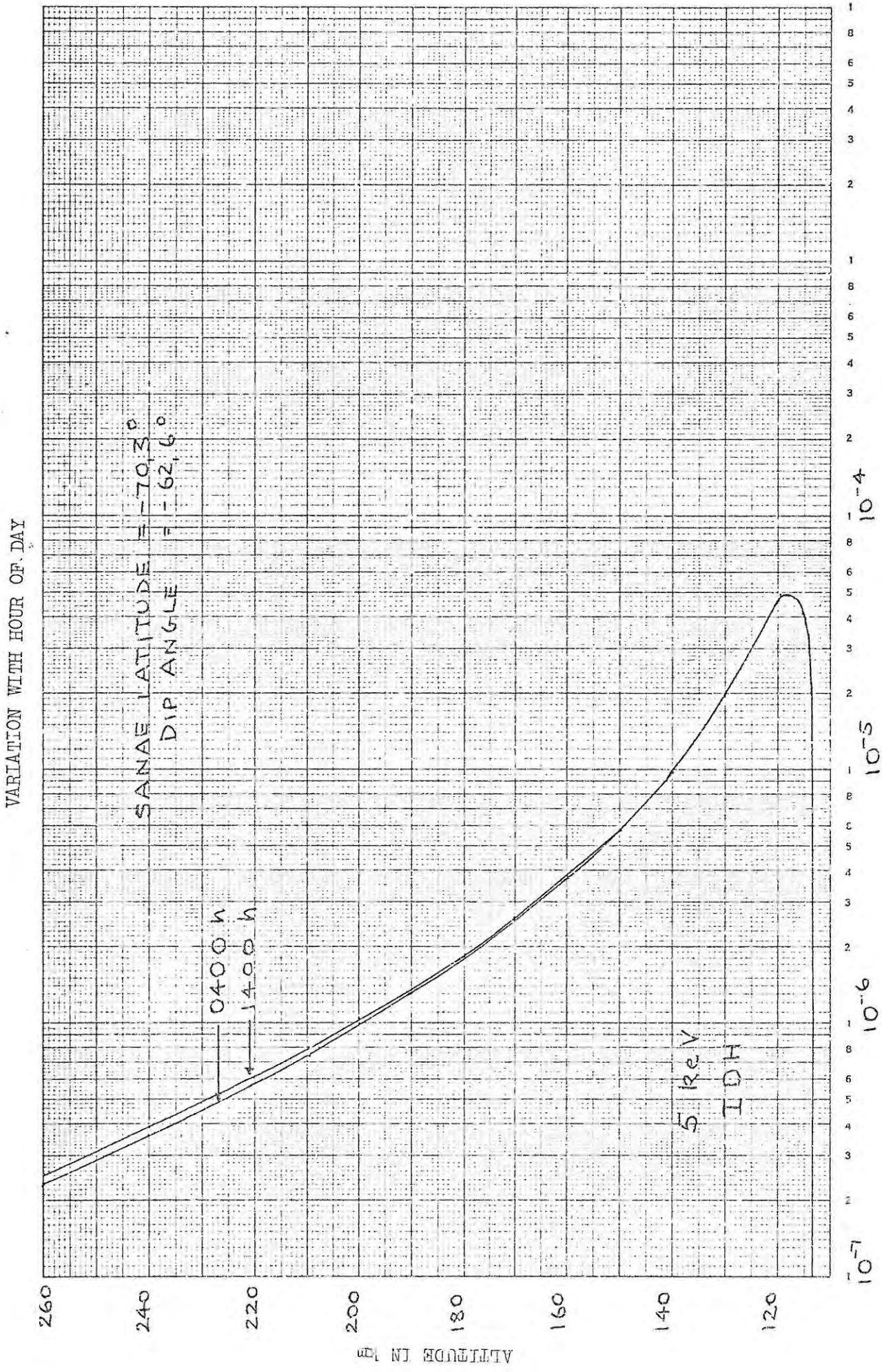
VARIATION WITH HOUR OF DAY
SANAE LATITUDE = -70.3°
DIP ANGLE = -62.6°
0400 h
1400 h
5 KeV
TDH
ALTITUDE IN km
260
240
220
200
180
160
140
120
IONIZATION RATE PER UNIT FLUX $\frac{q}{F}$ $\left(\frac{\text{ion pairs}}{\text{cl-cm}}\right)$
10^{-4}
10^{-5}
10^{-6}
10^{-7}

VARIATION WITH HOUR OF DAY

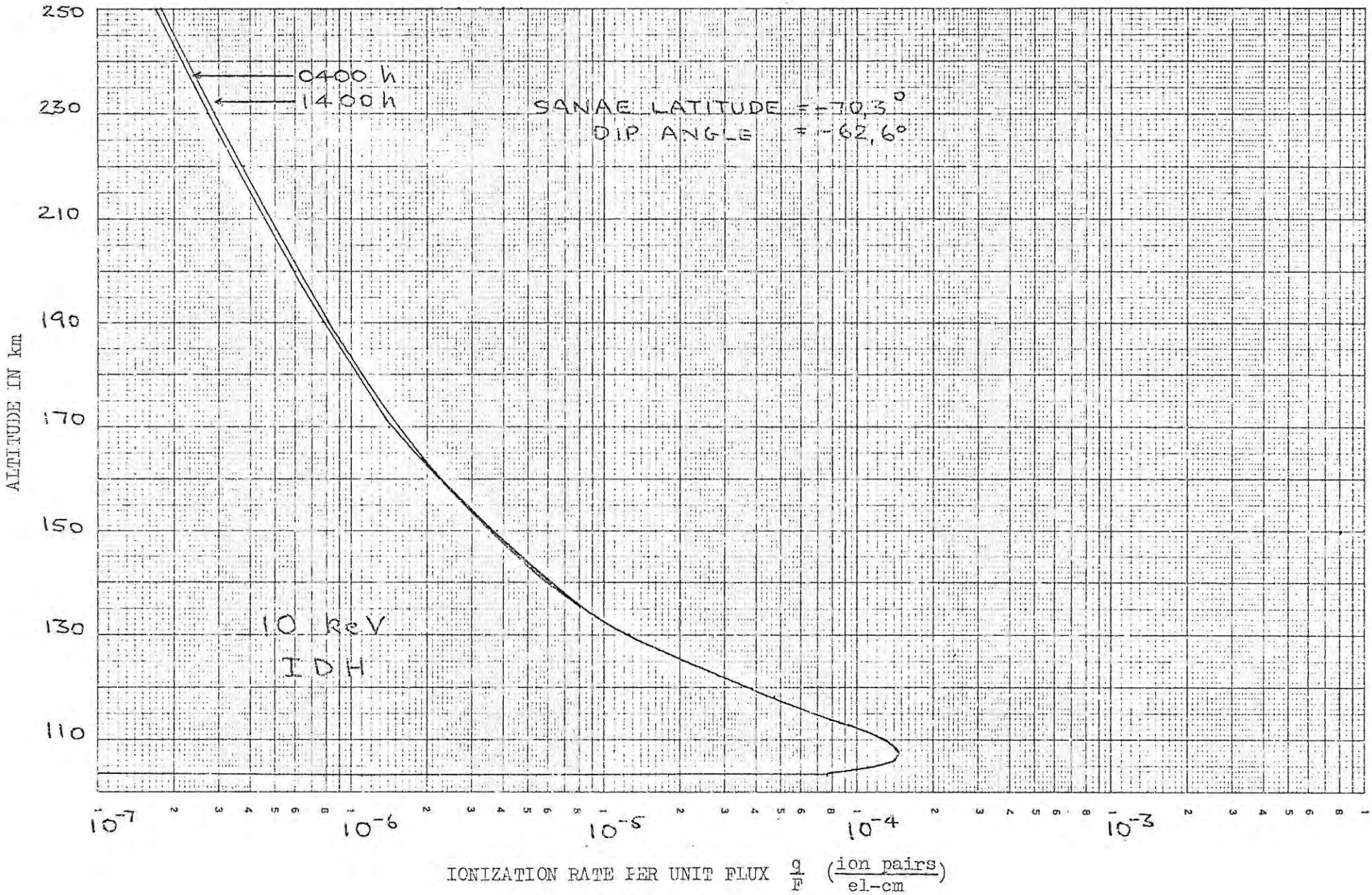

FIG. 7-3

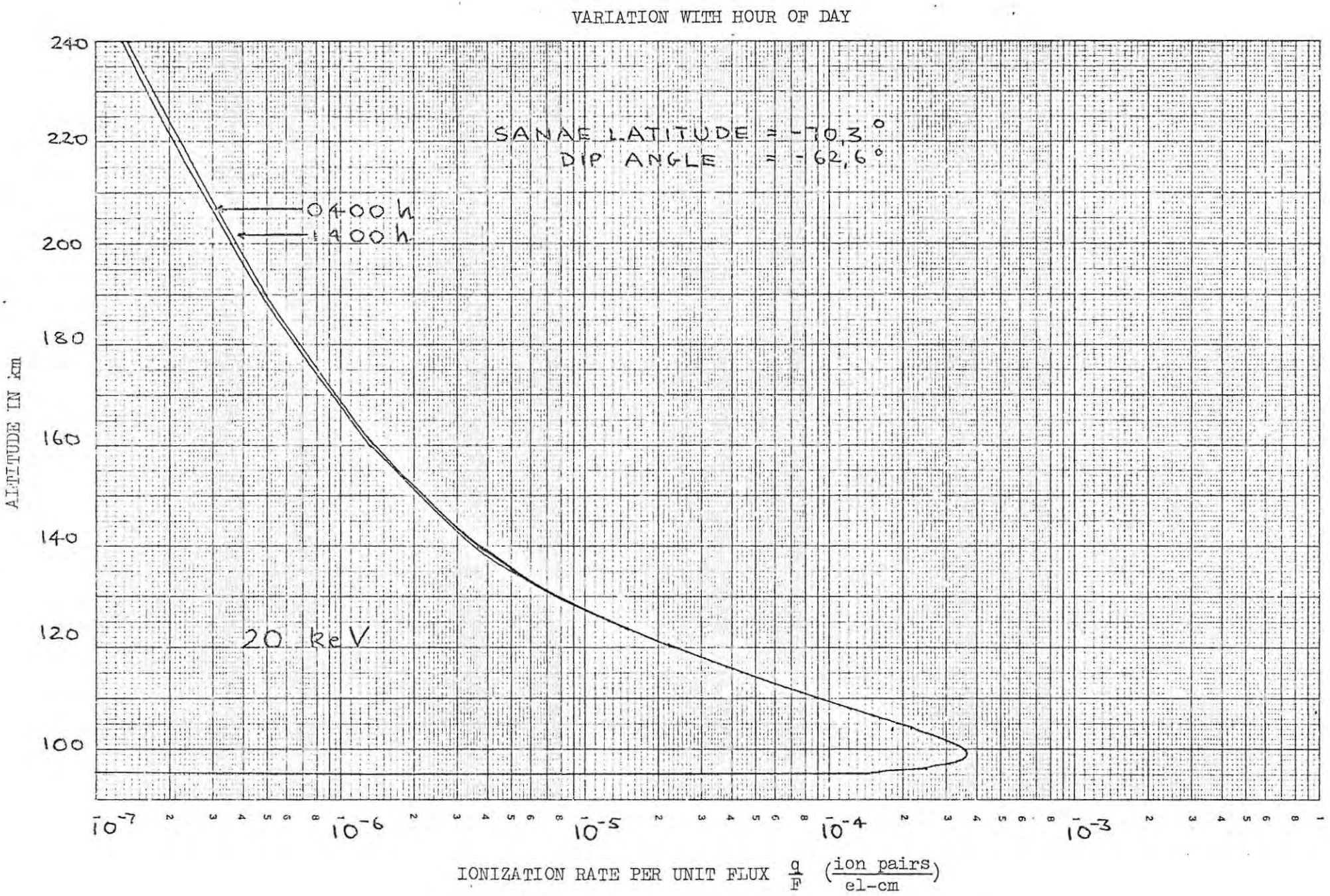
VARIATION WITH HOUR OF DAY
SANAE LATITUDE = -70,3°
DIP ANGLE = -62,6°
0400 h
1400 h
20 keV
240
220
200
180
160
140
120
100
ALTITUDE IN km
10^-7
10^-6
10^-5
10^-4
10^-3
IONIZATION RATE PER UNIT FLUX q/F (ion pairs / el-cm)

FIG. 7-4

2. The seasonal variation in T_{exo} at Sanae was found to be as shown below. This variation is typical of the Jacchia model atmosphere.

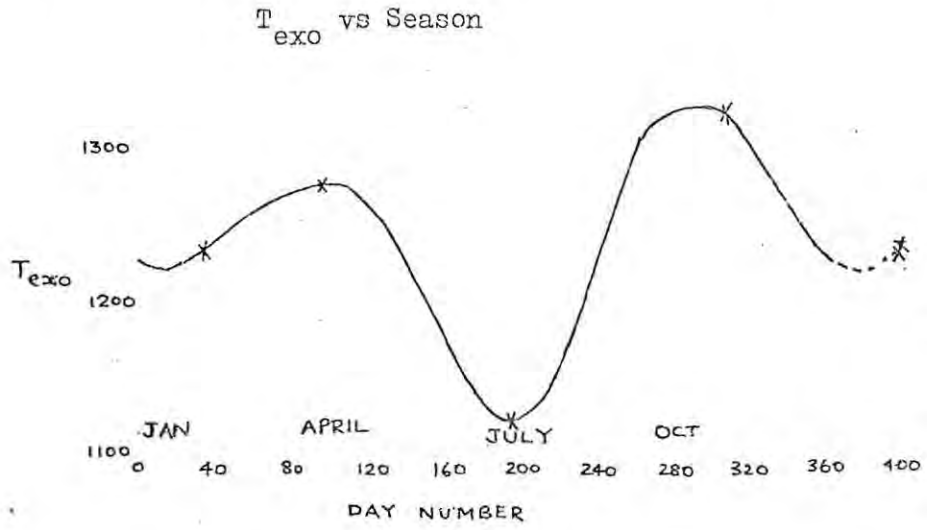

We see that there are two peaks, one in October and the other in April and two minima, one in June and the other in January. The maximum difference is about 200 K.

The ionization rate profiles shown in Fig. 7-5 to 7-8 are plotted for 15th July, 6th November, 4th February and 5th April. These days are marked with an X on the Fig. shown above (T_{exo} vs season).

The variation of h_m and q_m/F with day number is shown in Fig 7-9. For 1 keV electrons see that the maximum variation in h_m is about 6 km. For energies of 2 keV and greater there is negligible change in h_m throughout the years. For 1 keV electrons the variation in q_m/F is of the order of 10 %, for 2 keV this has dropped to 6% and is negligible for 5, 10 and 20 keV. From Table 7-3 it is seen that there is a greater influence in the F region. At 280 km the maximum difference is 28% and at 240 km $\approx$ 18%. This order of difference is found for all the energies at which we have looked. This could clearly be of importance in the investigation of the effects on the F-region of electron precipitation.

Table 7-3

Variation of q/F with season in the F-region

E_i	Alt. (km)	(35) 4th Feb.	(95) 5th April	(196) 15th July	(310) 6th Nov.	Max. difference (196 - 310)
1 keV	280	5,19(-7)	5,47(-7)	4,34(-7)	5,76(-7)	28%
	240	1,18(-6)	1,22(-6)	1,05(-5)	1,26(-6)	18%
	200	2,74(-6)	2,76(-6)	2,67(-6)	2,76(-6)	4%
2 keV	280	3,13(-7)	3,29(-7)	2,61(-7)	3,47(-7)	28%
	240	7,28(-7)	7,53(-7)	6,45(-7)	7,77(-7)	19%
	200	1,92(-6)	1,95(-6)	1,81(-6)	1,98(-6)	9%
5 keV	280	1,59(-7)	1,66(-7)	1,33(-7)	1,76(-7)	28%
	240	3,73(-7)	3,86(-7)	3,30(-7)	3,99(-7)	19%
	200	1,00(-6)	1,02(-6)	9,44(-7)	1,03(-6)	9%
10 keV	280	9,52(-8)	1,00(-7)	7,95(-8)	1,06(-7)	28%
	240	2,24(-7)	2,31(-7)	1,98(-7)	2,39(-7)	19%
	200	6,04(-7)	6,13(-7)	5,67(-7)	6,22(-7)	9%
20 keV	280	5,70(-8)	6,01(-8)	4,76(-8)	6,33(-8)	28%
	240	1,34(-7)	1,39(-7)	1,18(-7)	9.40(-8)	19%
	200	3,62(-7)	3,68(-7)	3,40(-7)	1,43(-7)	9%

VARIATION WITH SEASON

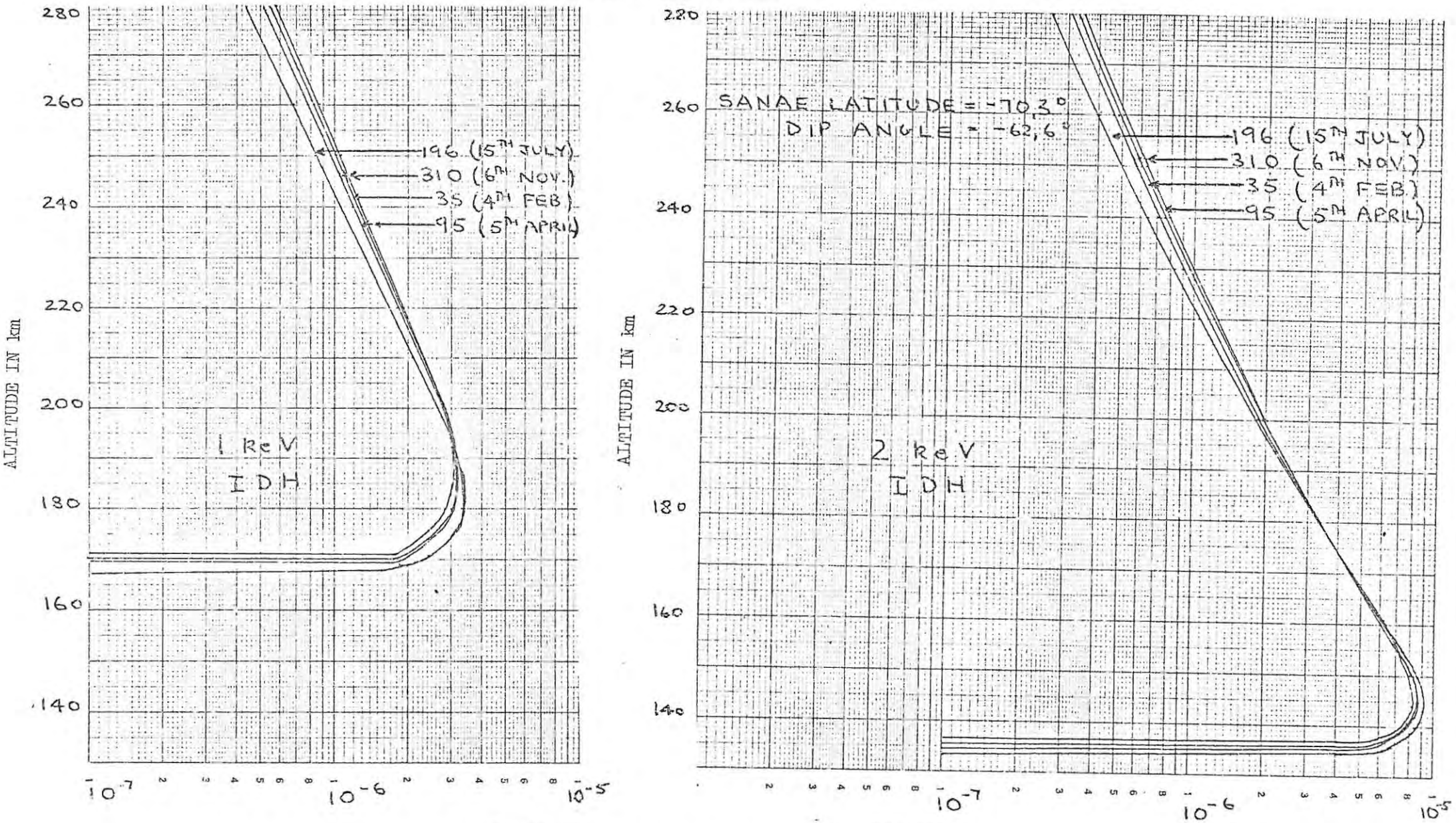

IONIZATION RATE PER UNIT FLUX $\frac{q}{F}$ $\left(\frac{\text{ion pairs}}{\text{el-cm}}\right)$

FIG. 7-5

VARIATION WITH SEASON

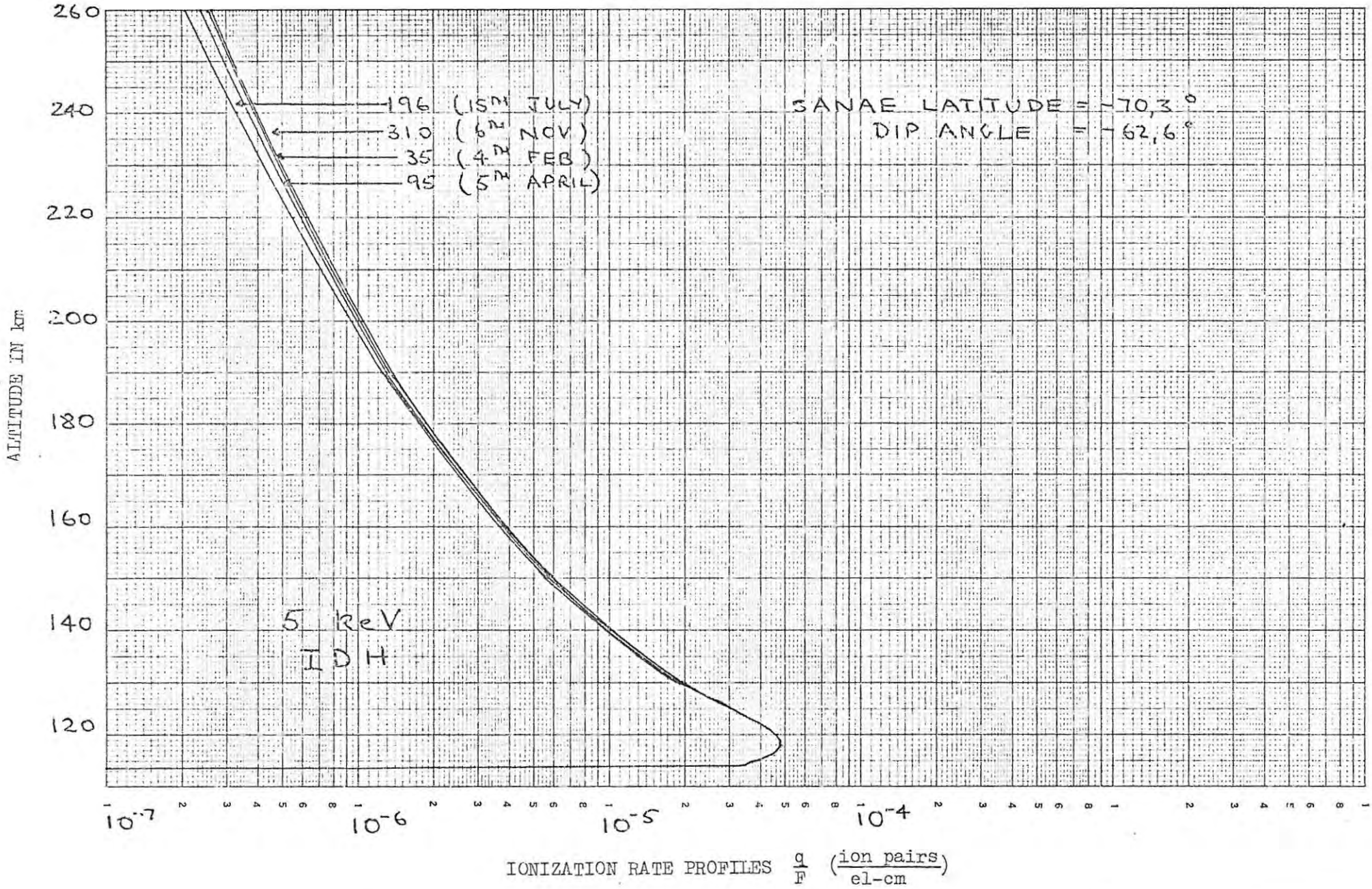

FIG. 7-6

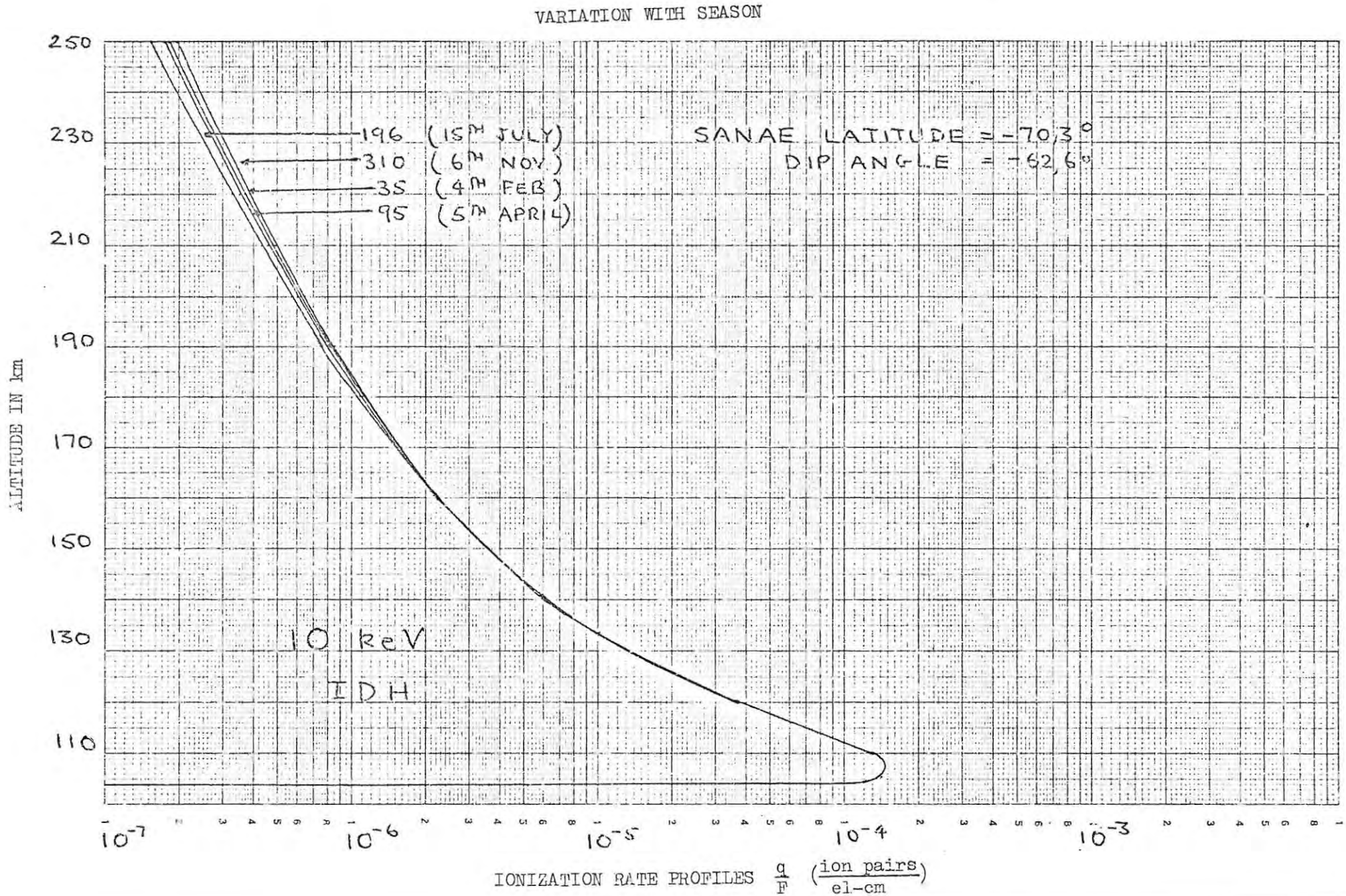
VARIATION WITH SEASON
250
230
210
190
170
150
130
110
ALTITUDE IN km
196 (15TH JULY)
310 (6TH NOV.)
35 (4TH FEB.)
95 (5TH APRIL)
SANAE LATITUDE = -70,3°
DIP ANGLE = -82,6°
10 KeV
IDH
10^-7
10^-6
10^-5
10^-4
10^-3
IONIZATION RATE PROFILES q/F (ion pairs / el-cm)

FIG. 7-7

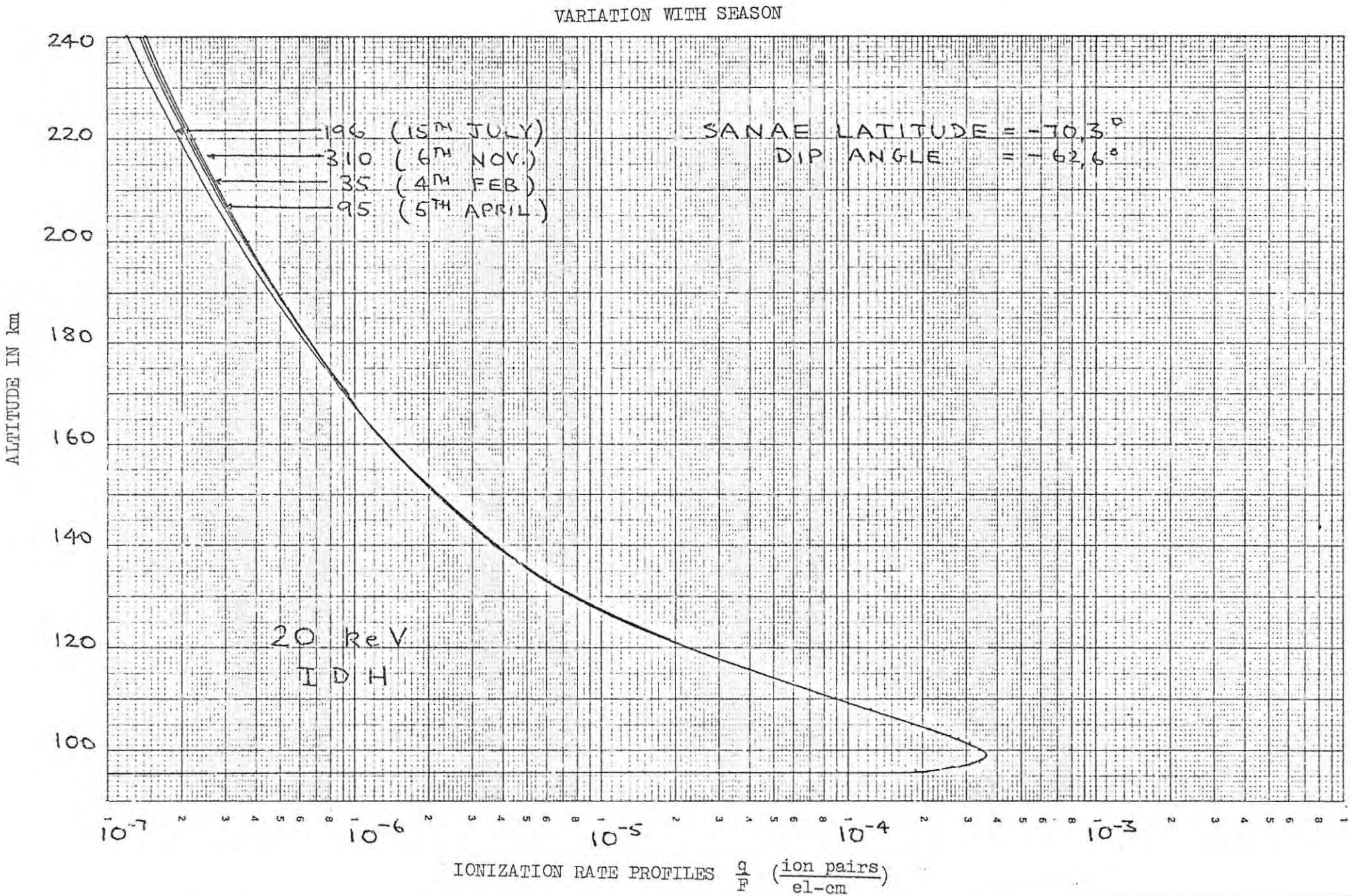
VARIATION WITH SEASON
240
220
200
180
160
140
120
100
ALTITUDE IN km
196 (15TH JULY)
310 (6TH NOV.)
35 (4TH FEB)
95 (5TH APRIL)
SANAE LATITUDE = -70,3°
DIP ANGLE = -62,6°
20 ReV
I D H
10^-7
10^-6
10^-5
10^-4
10^-3
IONIZATION RATE PROFILES q/F (ion pairs / el-cm)

FIG. 7-8

FIG. 7-9

Variation of h_m with Season.

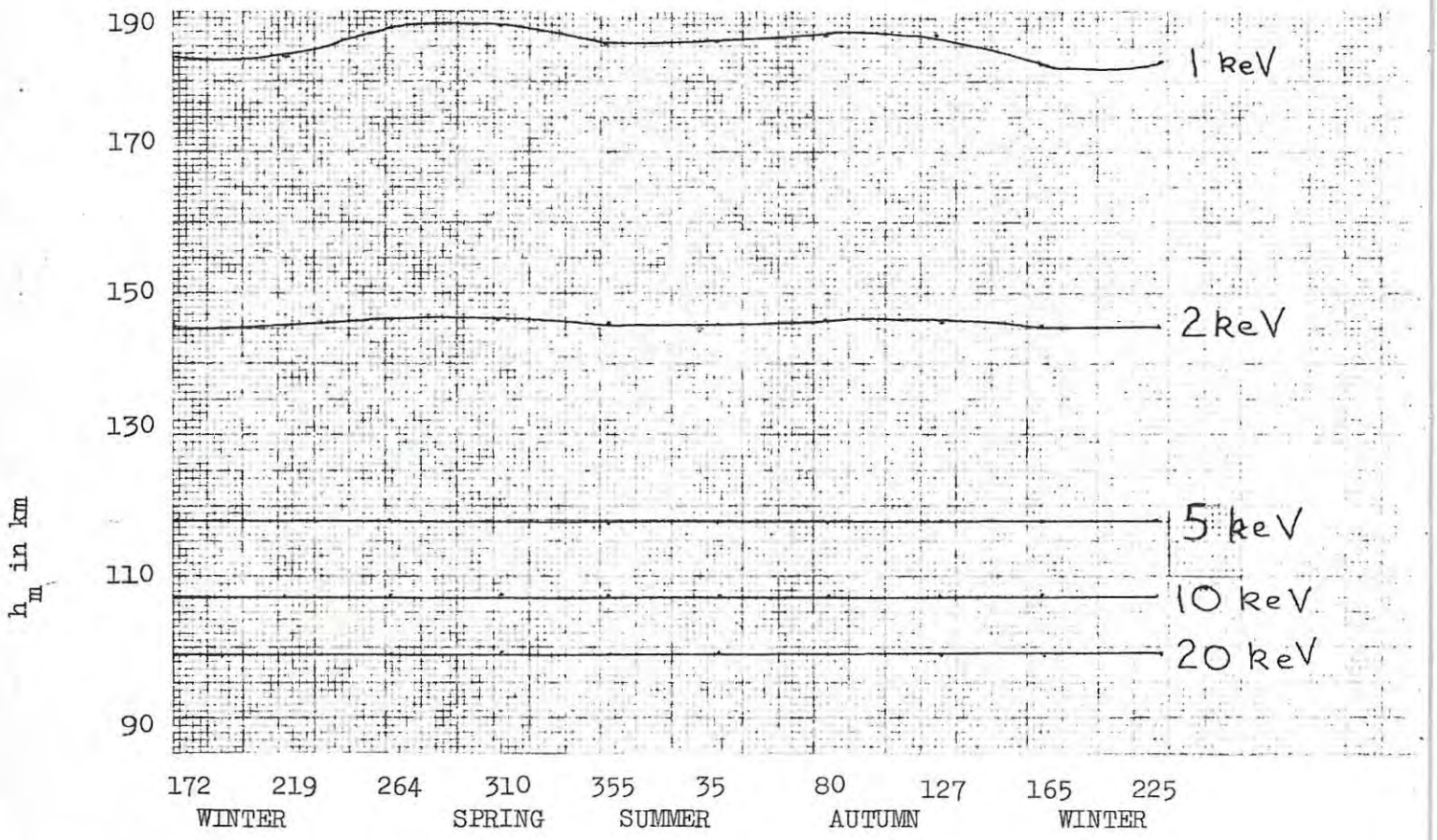

Variation of q_m/F with Season.

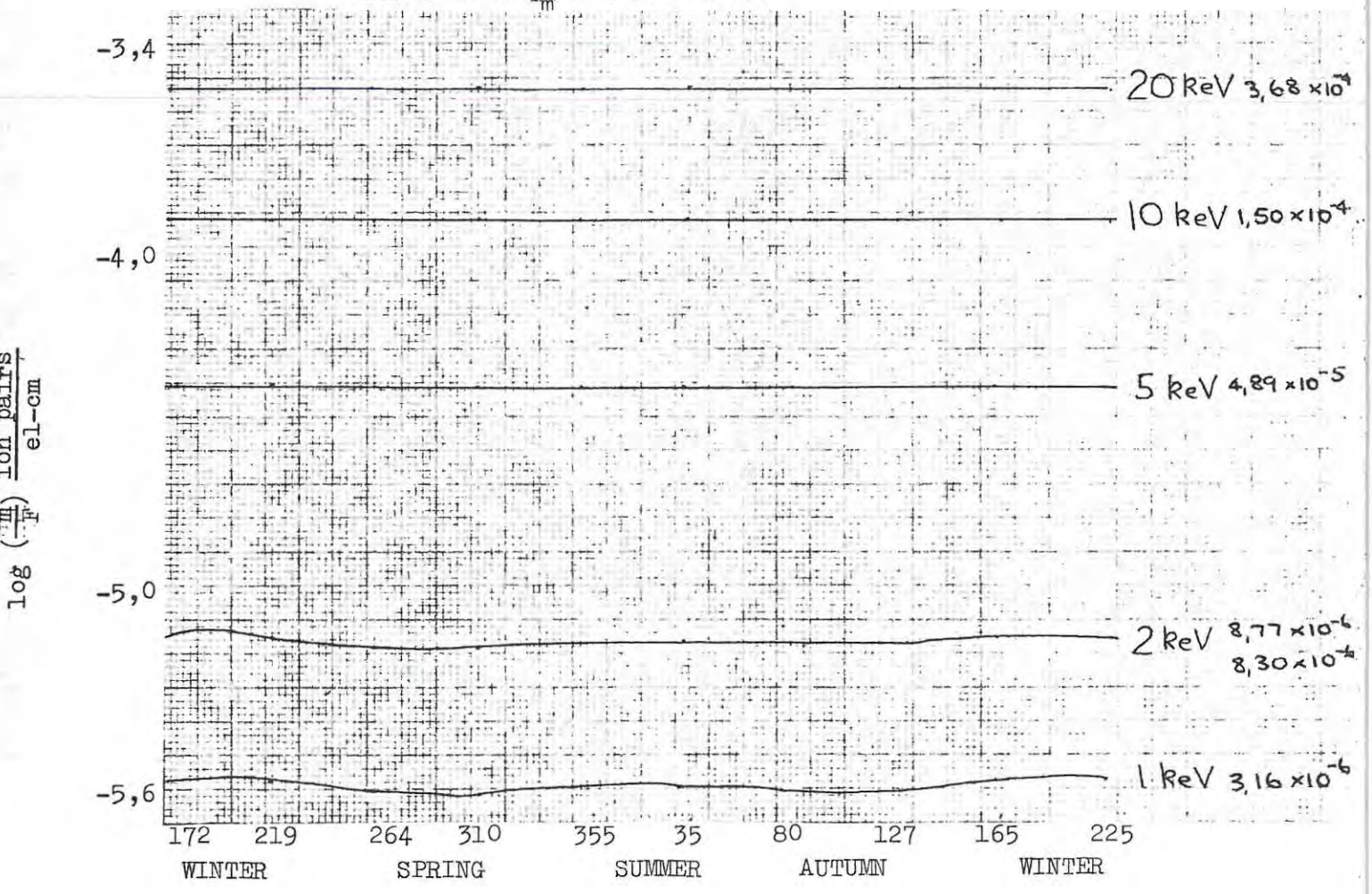

3. As solar activity increases so does the exospheric temperature of the Jacchia model atmosphere.

The following values of T_{exo} were found for three different values of $F_{10,7}$.

$F_{10,7}$	T_{exo}
100 (low solar activity)	1043 K
150 (mean solar activity)	1270 K
200 (high solar activity)	1497 K

On the basis of increased T_{exo} we would expect h_m to move upwards for higher values of $F_{10,7}$ and this is the case as may be seen for low energy electrons in Fig. 7-10. For 1 keV electrons we see that h_m ($F_{10,7}$ = 100) is about 180 km while h_m ($F_{10,7}$ = 200) has shifted to 190 km. The corresponding decrease in q_m/F is about 20% for the same increase in $F_{10,7}$. Similar behaviour is again observed for 2 keV electrons although in this case the change in h_m is only 2 km which may be regarded as negligible. The ionization rate profiles for 5, 10 and 20 keV electrons are shown in Figs. 7-11 to 7-13. Fig 7-14 shows the variation of h_m and q_m/F with $F_{10,7}$.

The differences between the profiles are much greater in the F-region. Table 7-4 gives values of q/F for 280, 240 and 200 km for 1, 2, 5, 10, and 20 keV electrons for several values of $F_{10,7}$ from 100 to 200. For 1 keV electrons we find that the ionization rate increases by 57% at 280 km when $F_{10,7}$ increases from 100 to 200. At 240 km this increase has dropped to 36%.

Table 7-4

Variation of $\frac{q}{F}$ with $F_{10,7}$ in the F-region

E_i	Alt.	q/F (100)	q/F (125)	q/F (150)	q/F (175)	q/F (200)	%age difference 100-200
1 keV	280	3,70(-7)	4,62(-7)	5,44(-7)	6,11(-7)	6,63(-7)	57%
	240	9,43(-7)	1,10(-6)	1,22(-6)	1,30(-6)	1,36(-6)	36%
	200	2,57(-6)	2,70(-6)	2,76(-6)	2,75(-6)	2,73(-6)	6%
2 keV	280	2,23(-7)	2,78(-7)	3,27(-7)	3,69(-7)	4,00(-7)	57%
	240	5,77(-7)	6,73(-7)	7,50(-7)	8,06(-7)	8,43(-7)	38%
	200	1,71(-6)	1,85(-6)	1,95(-6)	2,00(-6)	2,03(-6)	17%
5 keV	280	1,13(-7)	1,42(-7)	1,67(-7)	1,88(-7)	2,04(-7)	57%
	240	2,95(-7)	3,45(-7)	3,84(-7)	4,14(-7)	4,33(-7)	38%
	200	8,88(-6)	9,65(-7)	1,02(-6)	1,05(-6)	1,06(-6)	17%
10 keV	280	6,77(-8)	8,46(-8)	9,98(-8)	1,12(-7)	1,22(-7)	57%
	240	1,77(-7)	2,07(-7)	2,31(-7)	2,48(-7)	2,60(-7)	38%
	200	5,34(-7)	5,81(-7)	6,12(-7)	6,31(-7)	6,41(-7)	18%
20 keV	280	4,06(-8)	5,07(-8)	5,97(-8)	6,72(-8)	7,30(-8)	57%
	240	1,06(-7)	1,24(-7)	1,38(-7)	1,49(-7)	1,56(-7)	38%
	200	3,20(-7)	3,48(-7)	3,67(-7)	3,79(-7)	3,84(-7)	18%

VARIATION WITH $F_{10,7}$

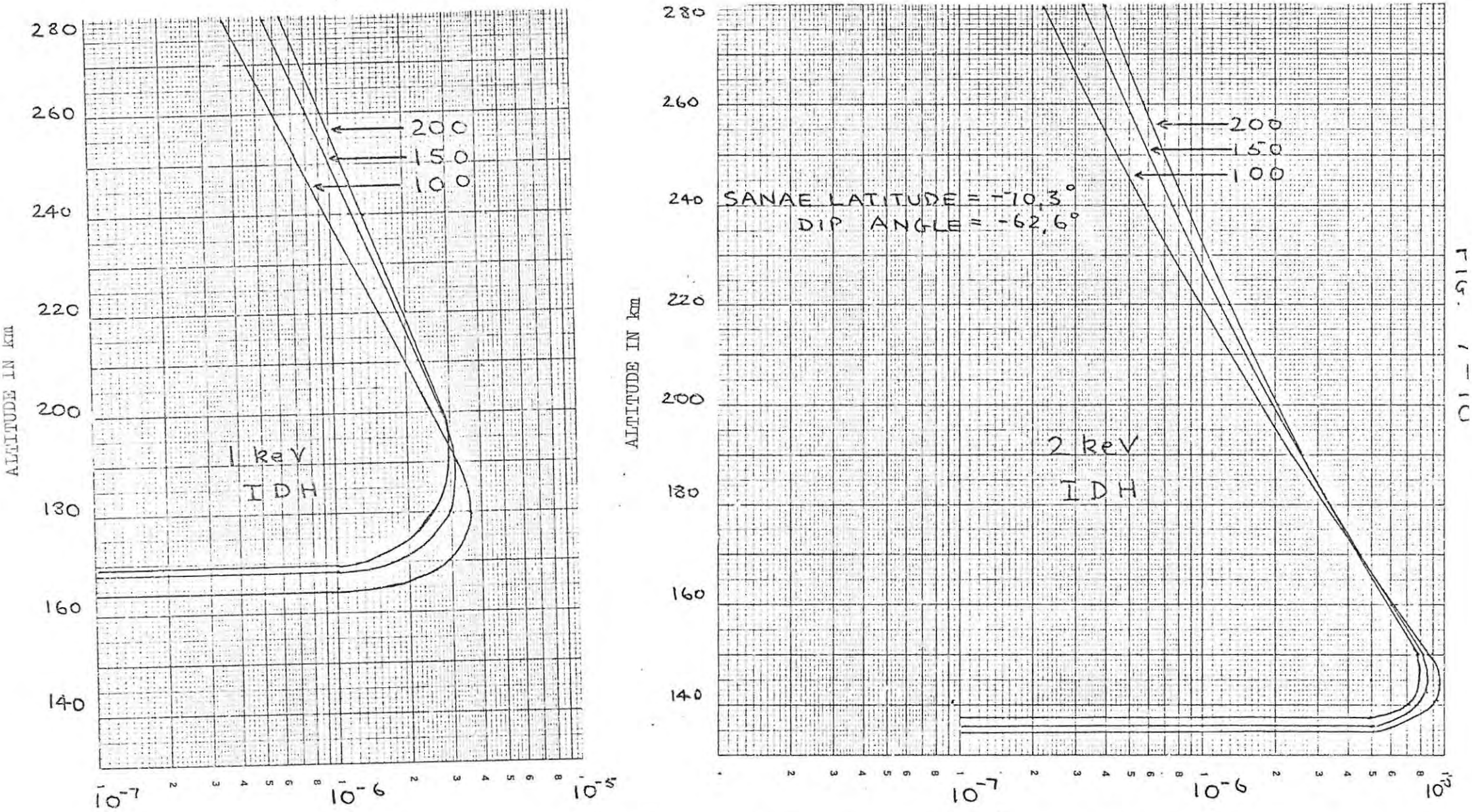

IONIZATION RATE PER UNIT FLUX $\frac{q}{F}$ $\left(\frac{\text{ion pairs}}{\text{el-cm}}\right)$

FIG. 1 - 10

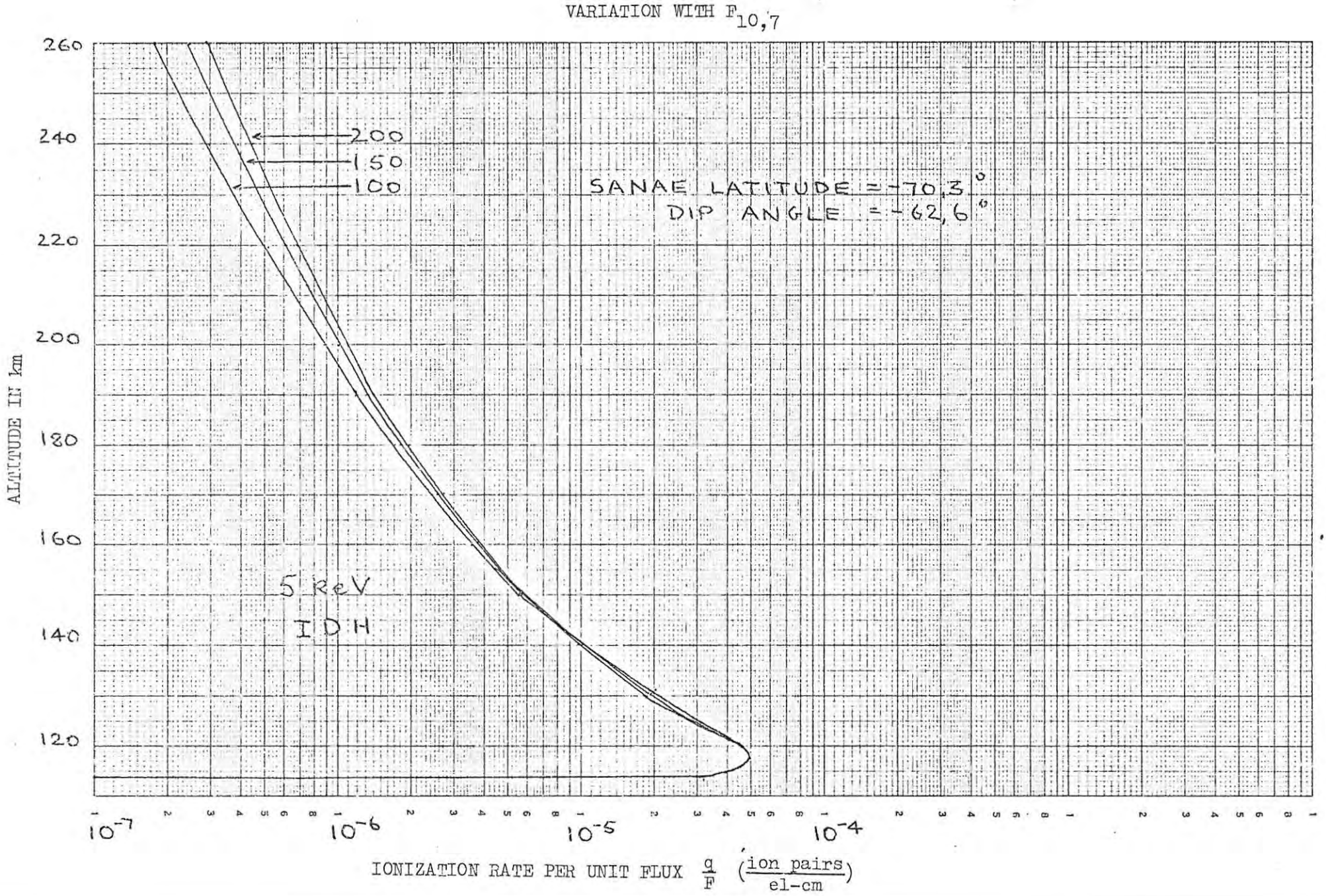
VARIATION WITH $F_{10,7}$
260
240
220
200
180
160
140
120
200
150
100
SANAE LATITUDE = -70,3°
DIP ANGLE = -62,6°
5 KeV
I D H
ALTITUDE IN km
10^{-7}
10^{-6}
10^{-5}
10^{-4}
IONIZATION RATE PER UNIT FLUX $\frac{q}{F}$ $(\frac{\text{ion pairs}}{\text{el-cm}})$

FIG. 7 - 11

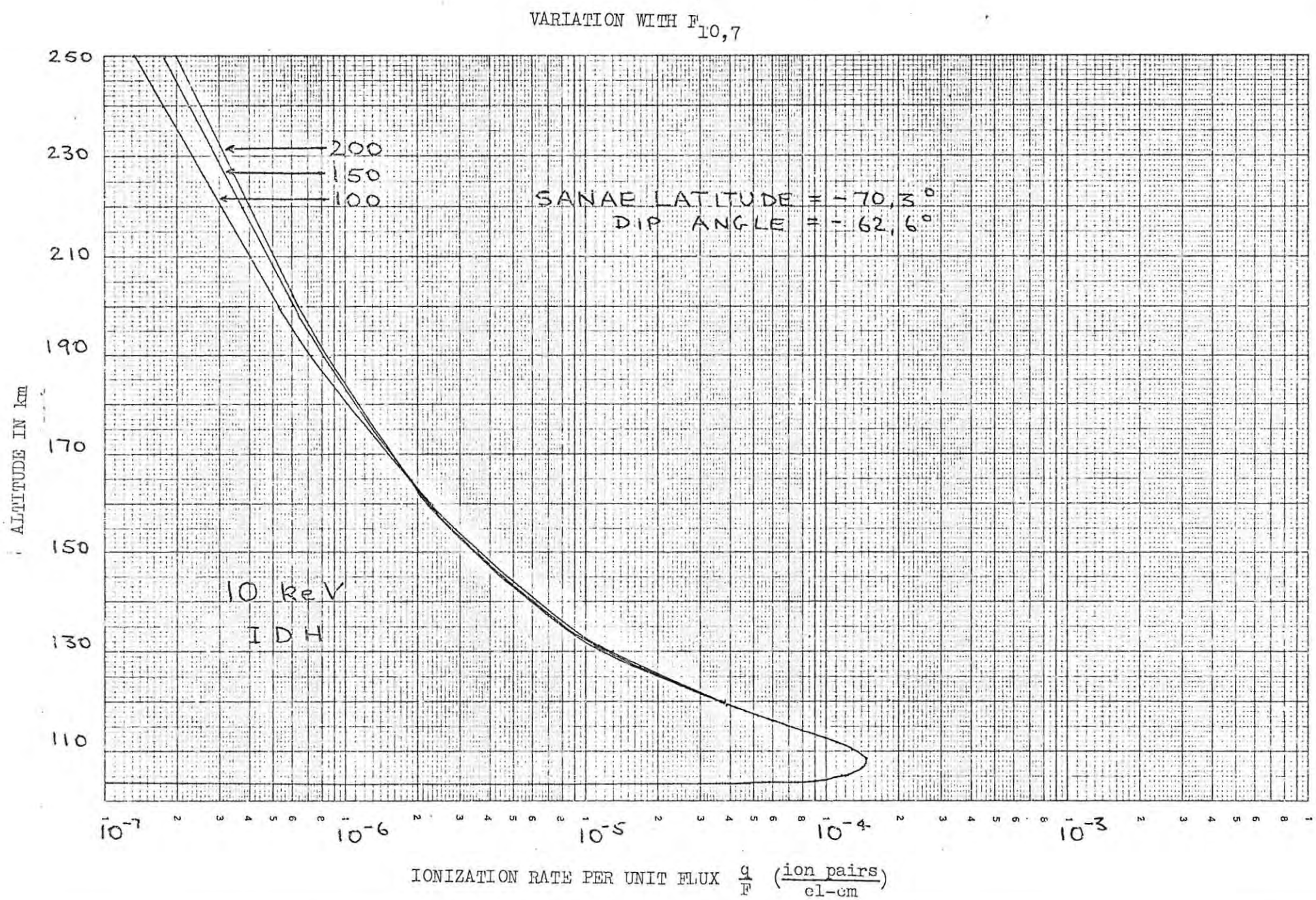
VARIATION WITH $F_{10,7}$
260
230
210
190
170
150
130
110
200
150
100
SANAE LATITUDE = -70,3°
DIP ANGLE = -62,6°
10 keV
I D H
ALTITUDE IN km
10^{-7}
10^{-6}
10^{-5}
10^{-4}
10^{-3}
IONIZATION RATE PER UNIT FLUX $\frac{q}{F}$ $(\frac{\text{ion pairs}}{\text{el-cm}})$

FIG 7-12

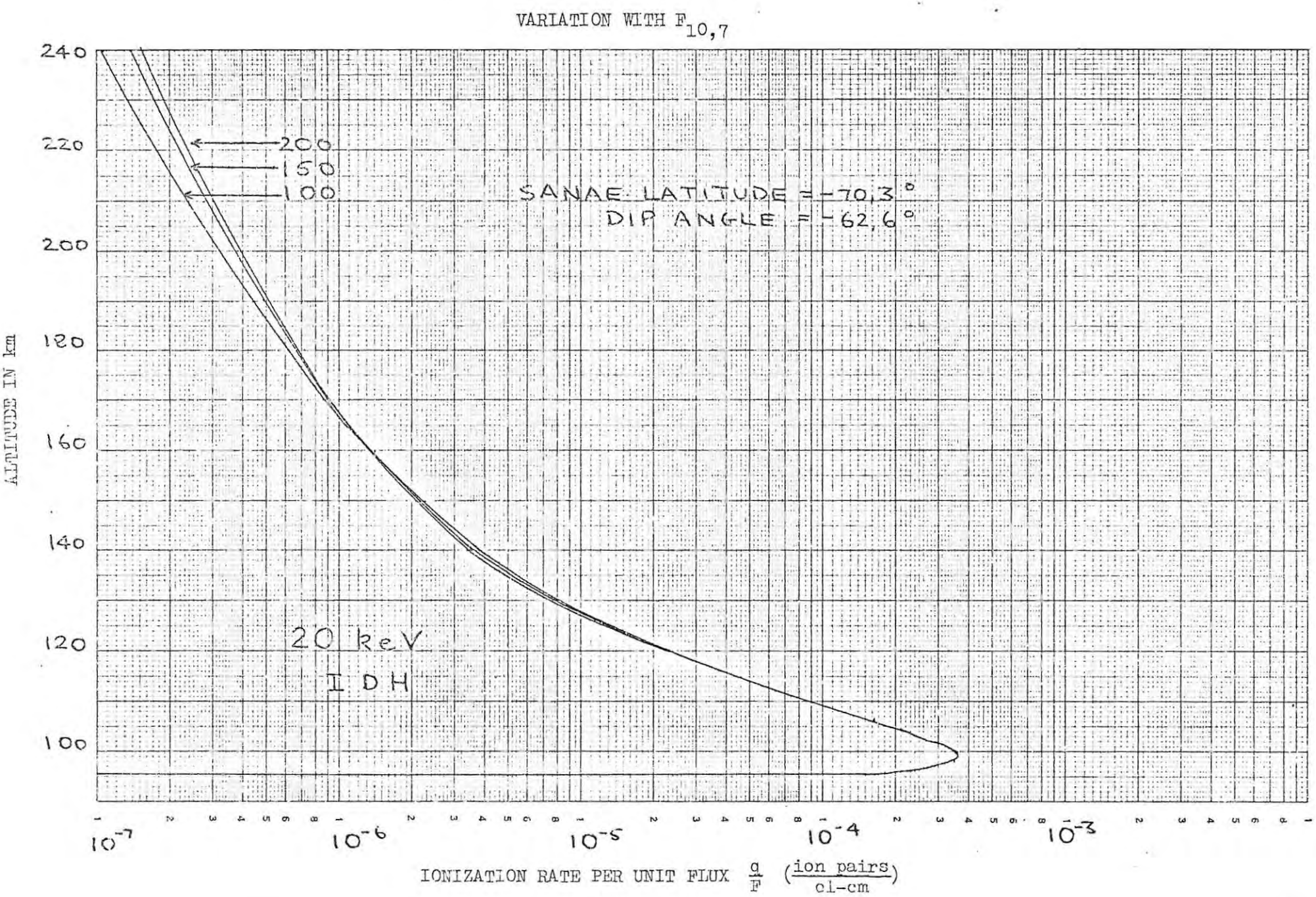
VARIATION WITH $F_{10,7}$
240
220
200
120
160
140
120
100
200
150
100
SANAE LATITUDE = -70,3°
DIP ANGLE = -62,6°
20 keV
H D H
ALTITUDE IN km
10^{-7}
10^{-6}
10^{-5}
10^{-4}
10^{-3}
IONIZATION RATE PER UNIT FLUX $\frac{q}{F}$ $(\frac{\text{ion pairs}}{\text{cl-cm}})$

FIG. 7-13

Variation of h_m with $F_{10,7}$

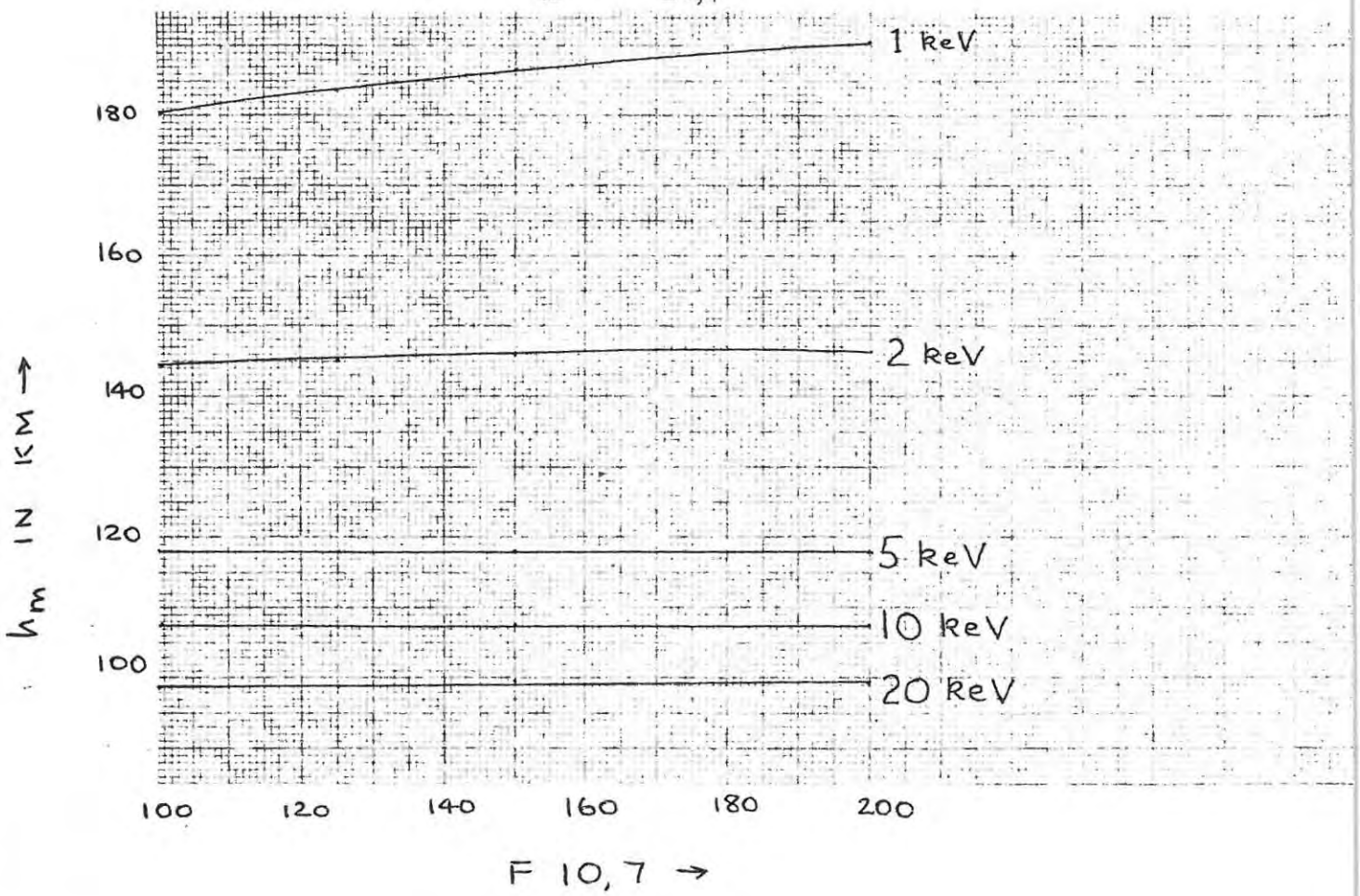

Variation of q_m/F with $F_{10,7}$.

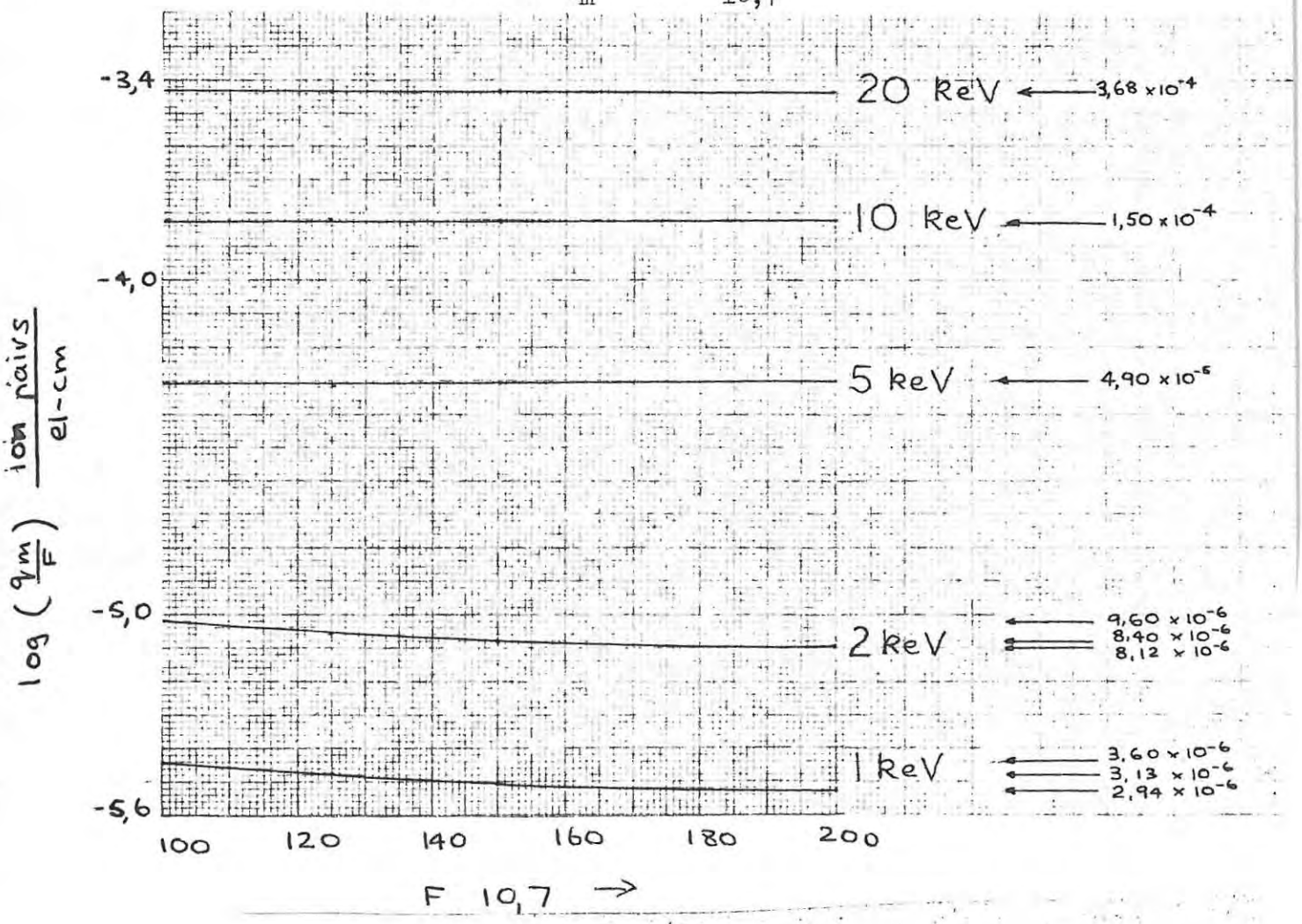

4. Finally we look at the influence of a_p on T_{exo} and the ionization rate profiles. We found the following variation of T_{exo} with a_p.

a_p = 4 (geomagnetically quiet day average)	T_{exo} = 1224 K
a_p = 11 (average daily value)	T_{exo} = 1270 K
a_p = 32 (geomagnetically disturbed day average)	T_{exo} = 1334 K

The ionization rate profiles for a_p = 4 11 and 32 are shown in Figs 7-15 to 7-18. Values of h_m and q_m/F versus a_p are given in Table 7-5. We see that even for 1 keV electrons h_m only changes by about 3 km and this is just about the maximum accuracy to which one can read an ionogram, although the URSI handbook recommends that heights in the F-region should not be scaled more accurately than 5 km. q_m/F decreases by about 4% as a_p increases from 4 to 32. Variations for energies of 2keV and greater are negligible.

Table 7-6 shows F-region variations, the increase in q/F at 280 km is about 10% for all energies. At 240 km this increase has dropped to 6% and becomes negligible by 200 km.

Table 7-5

h_m vs a_p (geomagnetic activity index) at Sanae.

E_i	4	11	32
1 keV	185,4	186,6	188,2
2 keV	145,8	146,0	146,2
5 keV	117,9	117,9	117,9
10 keV	107,3	107,3	107,3
20 keV	99,0	99,0	99,0

q_m/F vs a_p at Sanae

E_i	4	11	32
1 keV	3,20(-6)	3,13(-6)	3,06(-6)
2 keV	8,52(-6)	8,40(-6)	8,26(-6)
5 keV	4,90(-5)	4,89(-5)	4,89(-5)
10 keV	1,50(-4)	1,50(-4)	1,50(-5)
20 keV	3,68(-4)	3,68(-4)	3,68(-4)

Table 7-6

Variation of q/F with a_p in the F-region

E_i	altitude	4	11	32	%age difference between 4 and 32
1 keV	280	5,12(-7)	5,44(-7)	5,84(-7)	13%
	240	1,17(-6)	1,22(-6)	1,27(-6)	8%
	200	2,74(-6)	2,76(-6)	2,76(-6)	negl.
2 keV	280	3,08(-7)	3,27(-7)	3,52(-7)	14%
	240	7,21(-7)	7,50(-7)	7,84(-7)	9%
	200	1,91(-6)	1,95(-6)	1,98(-6)	negl.
5 keV	280	1,57(-7)	1,67(-7)	1,79(-7)	13%
	240	3,69(-7)	3,84(-7)	4,02(-7)	9%
	200	9,99(-7)	1,02(-6)	1,04(-6)	negl.
10 keV	280	9,39(-8)	9,97(-8)	1,07(-7)	13%
	240	2,22(-7)	2,30(-7)	2,41(-7)	9%
	200	6,01(-7)	6,12(-7)	6,24(-7)	negl.
20 keV	280	5,62(-8)	5,97(-8)	6,42(-8)	13%
	240	1,33(-7)	1,38(-7)	1,44(-7)	9%
	200	3,60(-7)	3,67(-7)	3,74(-7)	negl.

VARIATION WITH GEOMAGNETIC ACTIVITY INDEX a_p

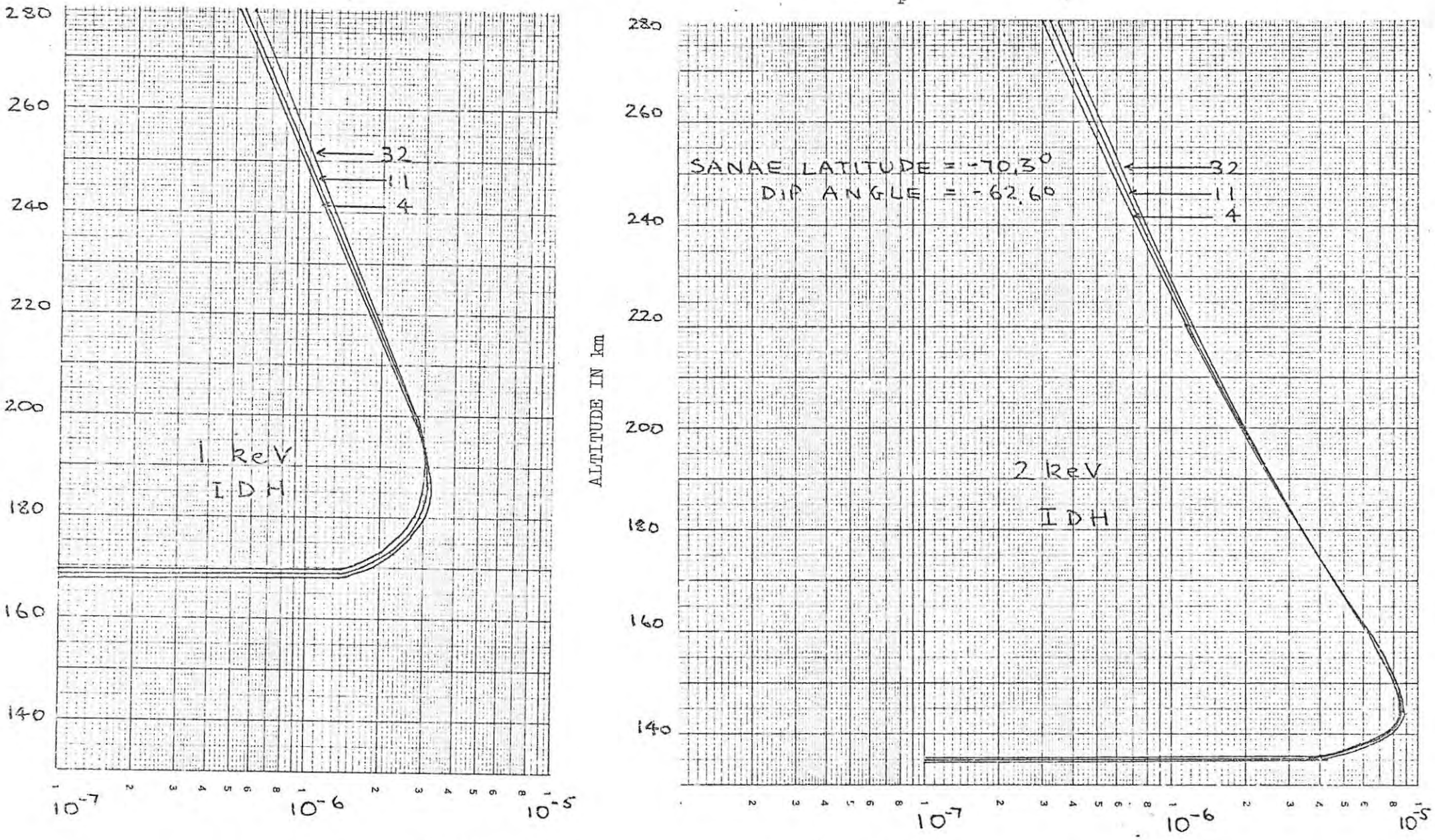

IONIZATION RATE PER UNIT FLUX $\frac{q}{F}$ $\left(\frac{\text{ion pairs}}{\text{el-cm}}\right)$

FIG. 7-15

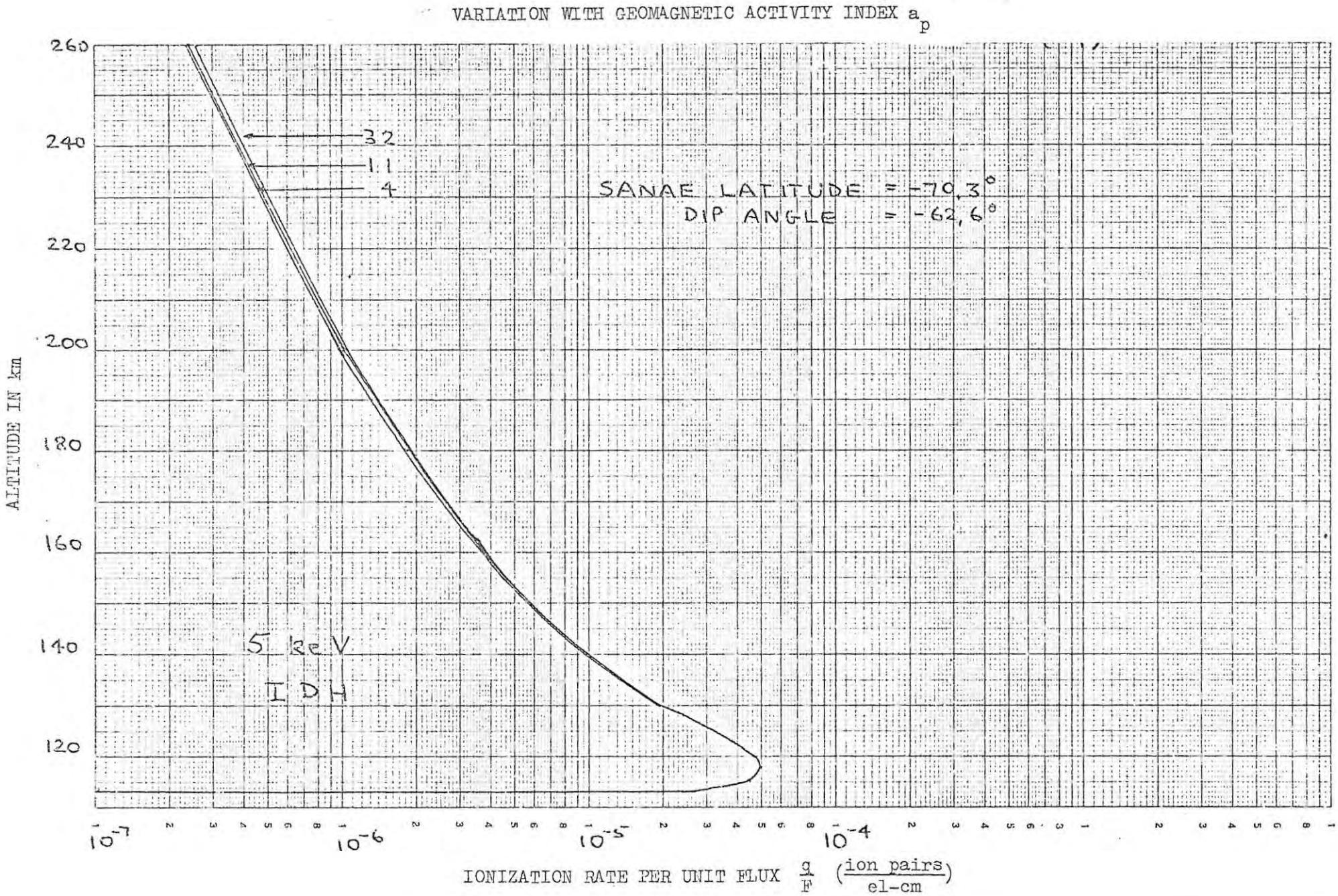
VARIATION WITH GEOMAGNETIC ACTIVITY INDEX a_p
260
240
220
200
180
160
140
120
ALTITUDE IN km
32
11
4
SANAE LATITUDE = -70,3°
DIP ANGLE = -62,6°
5 keV
I D H
10^{-7}
10^{-6}
10^{-5}
10^{-4}
IONIZATION RATE PER UNIT FLUX $\frac{q}{F}$ $(\frac{\text{ion pairs}}{\text{el-cm}})$

FIG. 7-16

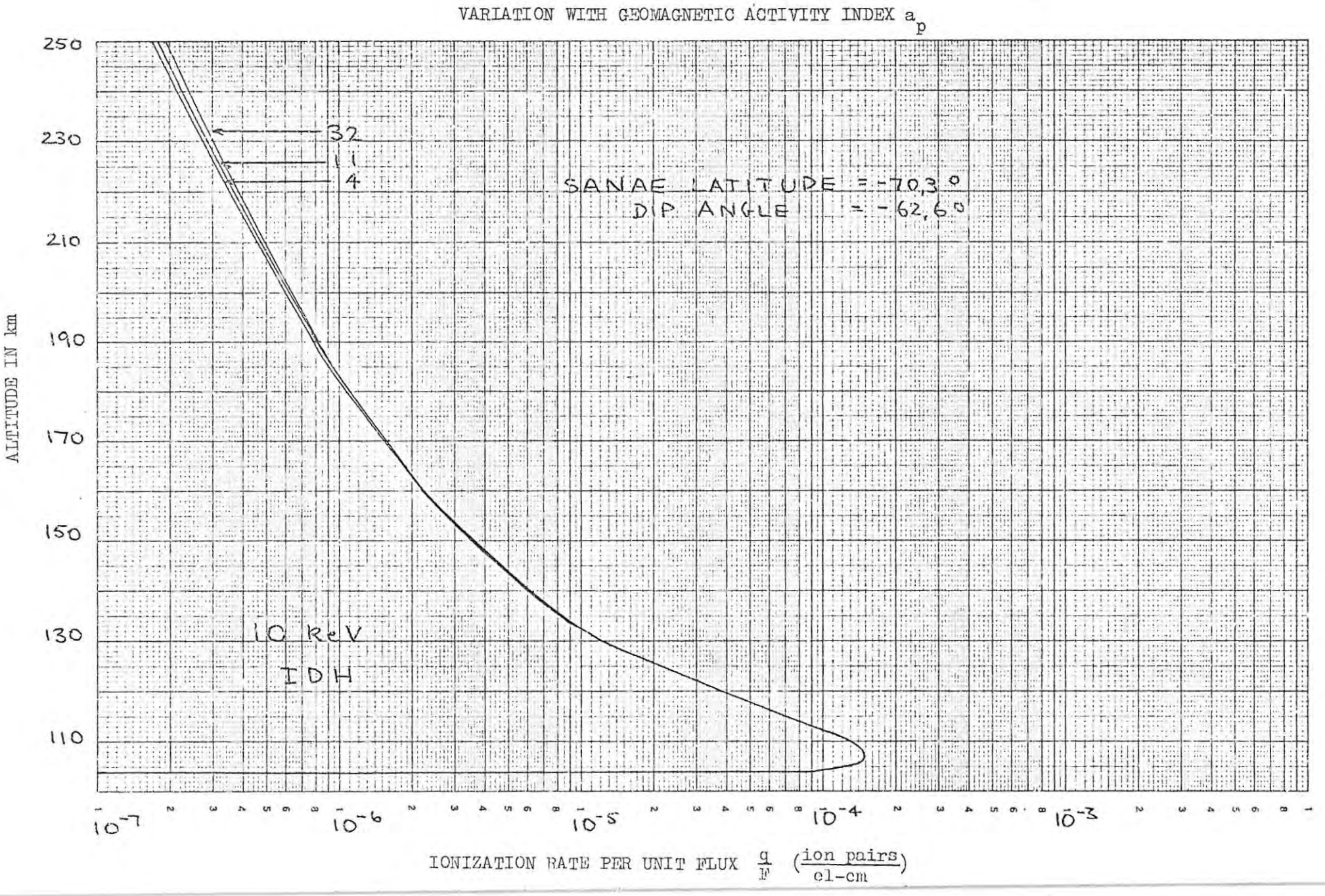
VARIATION WITH GEOMAGNETIC ACTIVITY INDEX a_p
250
230
210
190
170
150
130
110
ALTITUDE IN km
32
1
4
SANAE LATITUDE = -70,3°
DIP ANGLE = -62,6°
10 KeV
IDH
10^{-7}
10^{-6}
10^{-5}
10^{-4}
10^{-3}
IONIZATION RATE PER UNIT FLUX $\frac{q}{F}$ $(\frac{\text{ion pairs}}{\text{el-cm}})$

FIG. 7-17

VARIATION WITH GEOMAGNETIC ACTIVITY INDEX a_p

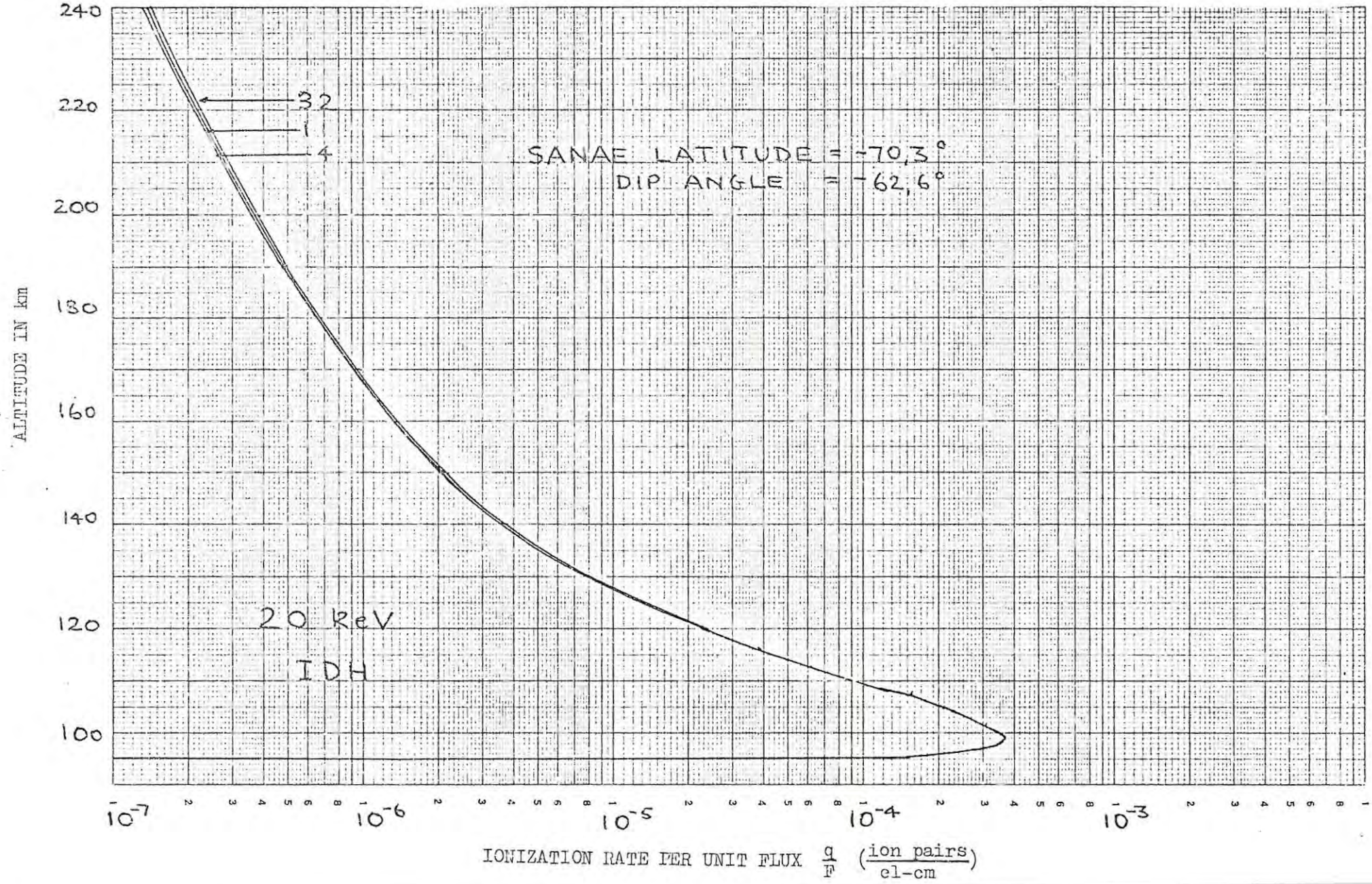

FIG. 7-18

5. Figs. 7-19 to 7-21 show h_m and q_m/F vs T_{exo} for Sanae. The equivalent curves for vertical incidence at the geomagnetic pole (dashed lines) are also shown and may be compared with those for Sanae. The most obvious features are displacement of the peak altitude h_m upwards for Sanae relative to that for geomagnetic pole and the downward displacement for q_m/F for Sanae relative to that for the pole. This almost constant displacement in the peak values for Sanae from those for the pole seems to indicate that the relationship between h_m and q_m/F for any two dip angles is unaffected by T_{exo}. This seems very reasonable since T_{exo} merely redistributes the atmosphere.

In conclusion to this chapter we note that as far as the peak production rate values and altitudes are concerned we can, to a first approximation, ignore diurnal and seasonal variations as well as any influence of the geomagnetic activity index a_p. The influence of the 10,7 cm solar flux is fairly marked over the range we have chosen because of the large increase in T_{exo}. Thus we can expect considerable change in ionization rate profiles produced by thesame electron fluxes during periods of solar activity.

As regards the F-region, for which we take the 280 km level as characteristic, all the parameters exert some influence. The hour angle and a_p produce a maximum difference of 10% while the seasonal maximum difference is of the order of 25%. We also note that the percentage difference is about 60 when $F_{10,7}$ increases from 100 to 200.

Another point to be noted is that the ionization rate profiles given in this thesis for Sanae depend only on the value of T_{exo} which is determined by the latitude of Sanae together with the parameters already mentioned. During a precipitation event, however, the temperature of the atmosphere would be expected to increase. (Herman and Chandra (1969) estimate that 2 eV per ion pair formed is used to increase the kinetic energy of the ambient gas). Our calculation of the model atmosphere does not take account of this increase in temperature and so it is likely that we underestimate production at greater heights using the present theory.

FIG. 7-19

VARIATION OF h_m WITH T_{exo} FOR SANAE

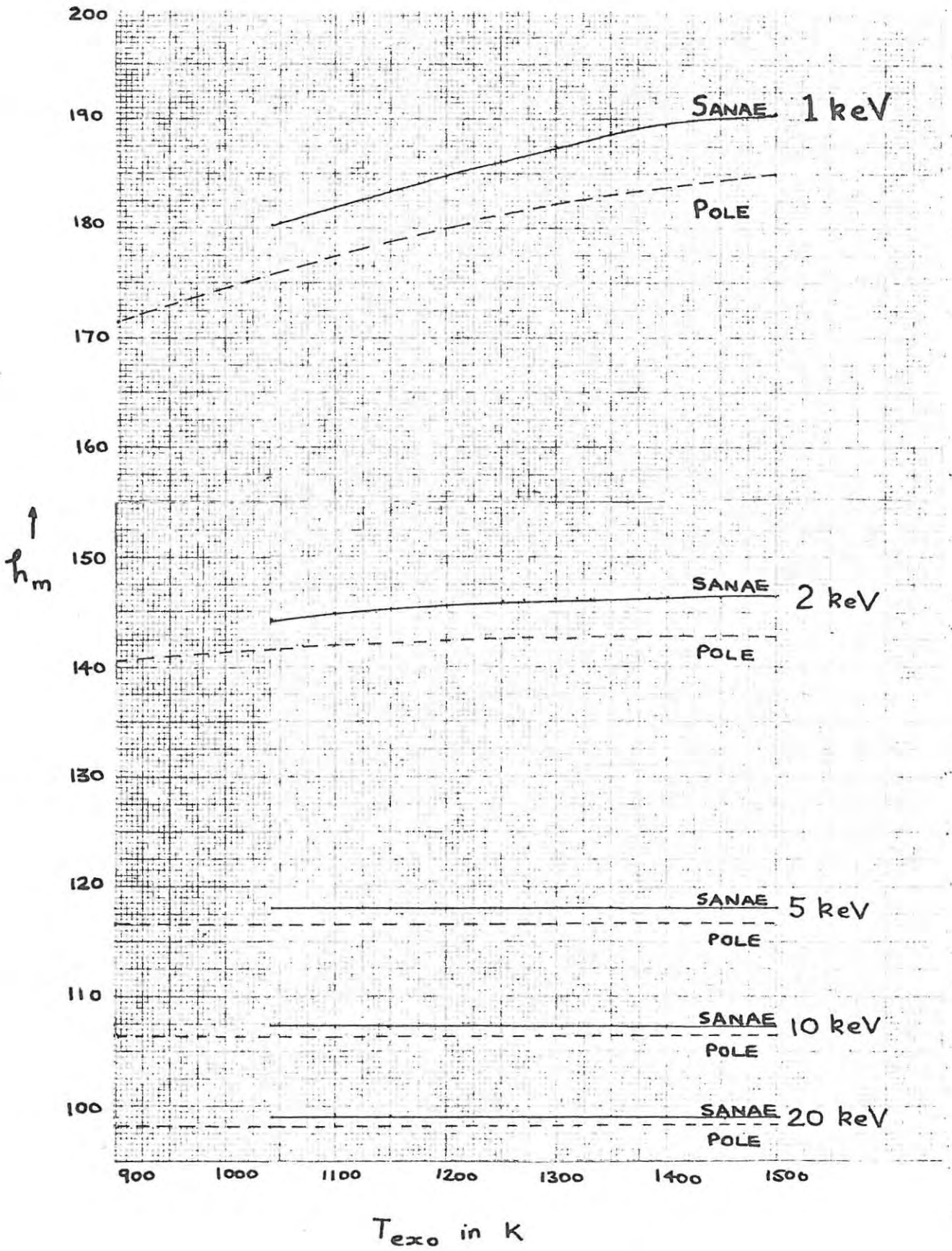

FIG. 7-20

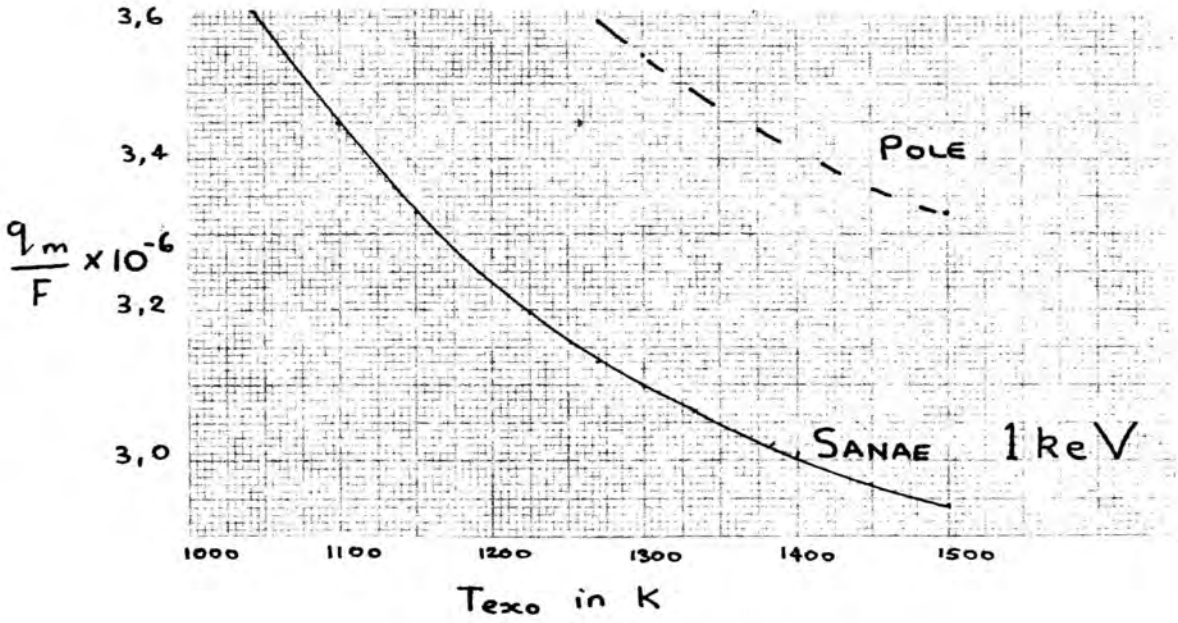

VARIATION OF q_m/F WITH T_{exo} FOR SANAE

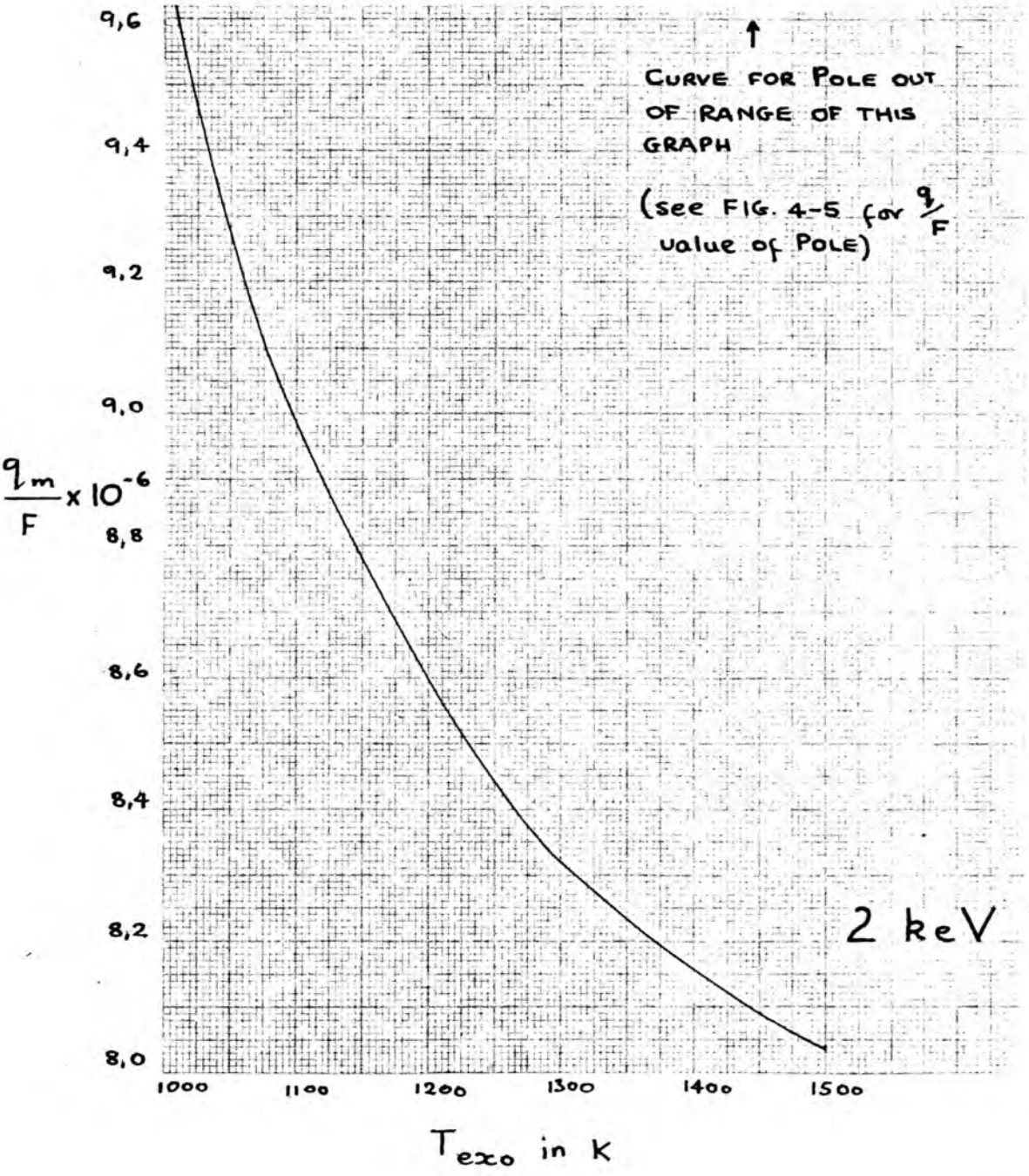

FIG. 7-21

VARIATION OF $\frac{q_m}{F}$ WITH T_{exo} FOR SANAE.

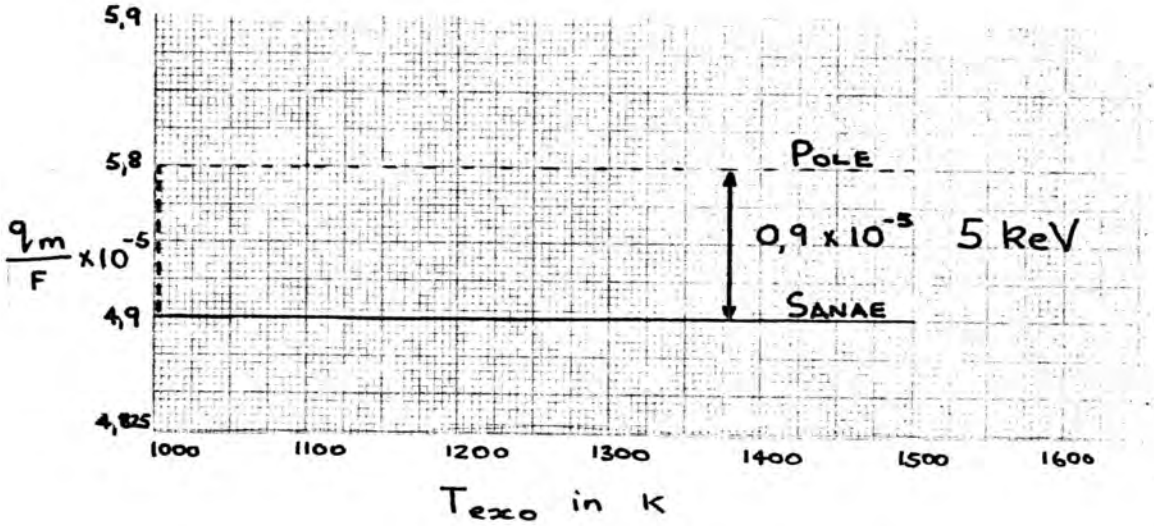

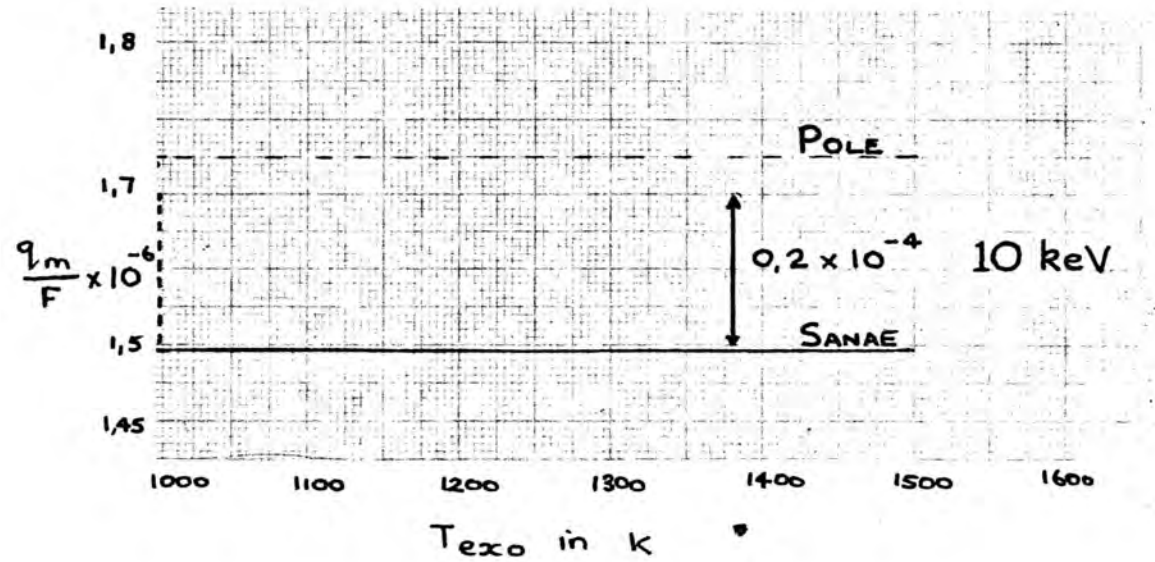

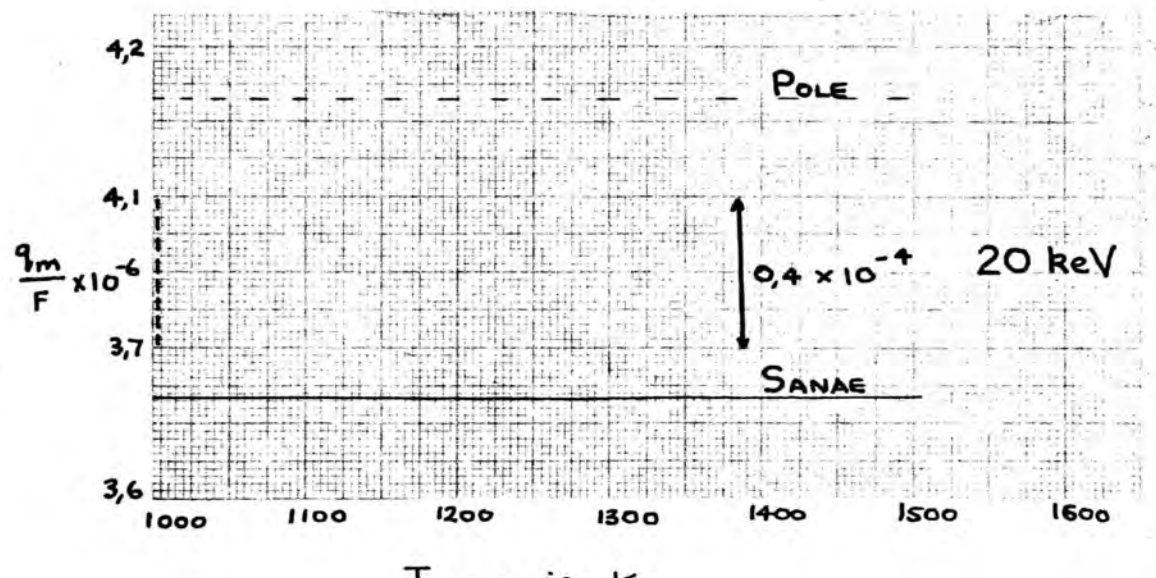

Chapter 8. An Energy Spectrum of the Type $J_{>E} = J_o e^{-E/E_o}$

Satellite observations indicate that fluxes of monoenergetic electrons seldom occur. (Although Evans (1968) reported a nearly monoenergetic flux of aurorae electrons). Most electrons fluxes measured may be described by an integral enery spectrum of the type

$$J_{>E} = J_o e^{-E/E_o} \text{ el/cm}^2 \text{ sec keV sr} \qquad (8\text{-}1)$$

where $J_{>E}$ is the directional flux of electrons having energy $> E$.

J_o is the directional flux above zero energy
E_o is the characteristic (or e-folding) energy
E is any selected energy

(Ulwick, Reidy and Baker, 1967 and Bailey, 1968)

Several authors such as Sharp(private communication with Hultqvist (1965)) Christensen and Karas (1970) and Galperin and Temny (1968) have analysed satellite data and found E_o to vary from 2 to 200 keV.

Previously we have dealt with monoenergetic fluxes and calculated values of q/F contributions over a range of energies, multiplying each contribution by the fraction of the total flux density expected in each small energy interval. Note that F represents the IDH flux for each given energy interval.

The directional flux density in the energy interval ΔE is given by

$$j \Delta E = J_{>E} - J_{>E+\Delta E} = J_o \frac{\Delta E}{E_o} e^{-E/E_o} \qquad (8\text{-}2)$$

For an IDH flux (8-2) becomes (from Appendix 1)

$$\pi j \Delta E = \pi J_o \frac{\Delta E}{E_o} e^{-E/E_o} \qquad (8\text{-}3)$$

We find the ionization rate at a given altitude by summing $(q/F) \quad j \Delta E$ over all energies

i.e. $$Q = \sum_E \frac{q}{F} \pi J_o \frac{\Delta E}{E_o} e^{-E/E_o}$$

or $$Q/\pi J_o = \sum_E \frac{q}{F} \frac{\Delta E}{E_o} e^{-E/E_o} \qquad (8\text{-}4)$$

which is the ionization rate per unit integral IDH flux.

The AW18 program can be used to calculate ionization, rates for a flux of electrons with the assumed energy spectrum $J_{>E} = J_o e^{-E/E_o}$ or for a flux of monoenergetic electrons. An appropriate data card determines which ionization rate profile is to be calculated (See Appendix 2 for the flow chart and printout of the AW18 program). Briefly, the method involves using q/F as calculated for a given energy E (this energy varies through a chosen range), multiplying the result by the factor $\frac{\Delta E}{E_o} e^{-E/E_o}$ and summing the contibutions over the energy range.

The e-folding energy E_o is of prime importance in determining whether the energy spectrum is hard or soft. For a hard spectrum E_o is typically greater than 40 keV and for a soft spectrum E_o is from 2 to 10 keV.

For our calculations we have chosen the energy range to be from 1 keV to 10 E_o and the energy interval ΔE to be E/100.

We have not included energies below 1 keV because the scattering cross-sections are not well known for lower energies. It is doubtful if the value of 35 eV/ ion pair formed can be applied to energies below 1 keV.

Hultqvist (1965) mentioned that Sharp et al (in a private communication) "did not on occasion find any energy flux below 1,5 keV". O'Brien and Taylor (1964) concluded from luminosity measurements above 250 km that the energy spectrum is not of the power law type below 1 keV. Burch (1968) however, showed that this is not necessarily the case. Ignoring energies less than 1 keV will have the effect of underestimating the ionization rate in the F-region above 200 km but will not seriously influence the energy deposition below this altitude.

The upper energy limit is chosen to be 10 E_o as we do not expect the flux of electrons to be very great above this. (If J_o is 10^6 electrons/cm^2 sec sr, $J_{>E} = J_o e^{-E/E_o} \approx \frac{J_o}{50000} \simeq$ 20 els-cm^2 sec sr).

Choosing $\Delta E = E/100$ gives us an increment which increases proportionately to E. This means that smaller increments are used at the low energy end, where the ionization rate profiles change rapidly with small changes in initial energy, and greater increments towards the upper limit of the range where the differences between the ionization rate profiles are not great for small changes in initial energy.

Figure 8-1 shows the ionization rates per unit IDH flux ($Q/\pi J_o$) for different e-folding energies (solid lines). The harder spectra produce less ionization in the F-region and also peak at lower altitudes than do the softer spectra. The peak altitudes and ionization rates per unit flux for several e-folding energies are:

E_o (keV)	h_m (km)	$\frac{Q_m}{\pi J_o}$ ($\frac{\text{ion pairs}}{\text{el-cm}}$)
2	119,4	$7,8 \times 10^{-6}$
5	108,6	$3,5 \times 10^{-5}$
20	92,7	$2,0 \times 10^{-4}$
50	below 90	$4,9 \times 10^{-4}$
100	below 90	$5,8 \times 10^{-4}$

Suppose we have $J_{>E} = J_o e^{-E/E_o}$ then the flux in the energy interval $\Delta E = j \Delta E = \frac{J_o}{E_o} e^{-E/E_o} \Delta E$; we may now find the average energy carried by the flux

$$= \frac{1}{J_o} \int_o^\infty J_o \frac{E}{E_o} e^{-E/E_o} dE \qquad (8\text{-}5)$$

$$= \frac{1}{E_o} \int_o^\infty E\, e^{-E/E_o} dE$$

$$= E_o \qquad (8\text{-}6)$$

Thus the e-folding energy is the average energy per electron for a spectrum of this type. The dashed lines on Fig. 8-1 are the monoenergetic profiles for 2,5 and 20 keV. The profile for the monoenergetic flux is denoted by E_i (initial energy) while that for the energy spectrum is denoted by E_o (the e-folding energy).

IONIZATION RATE PROFILES FOR DIFFERENT e-FOLDING ENERGIES (VERTICAL INCIDENCE AT THE POLE)

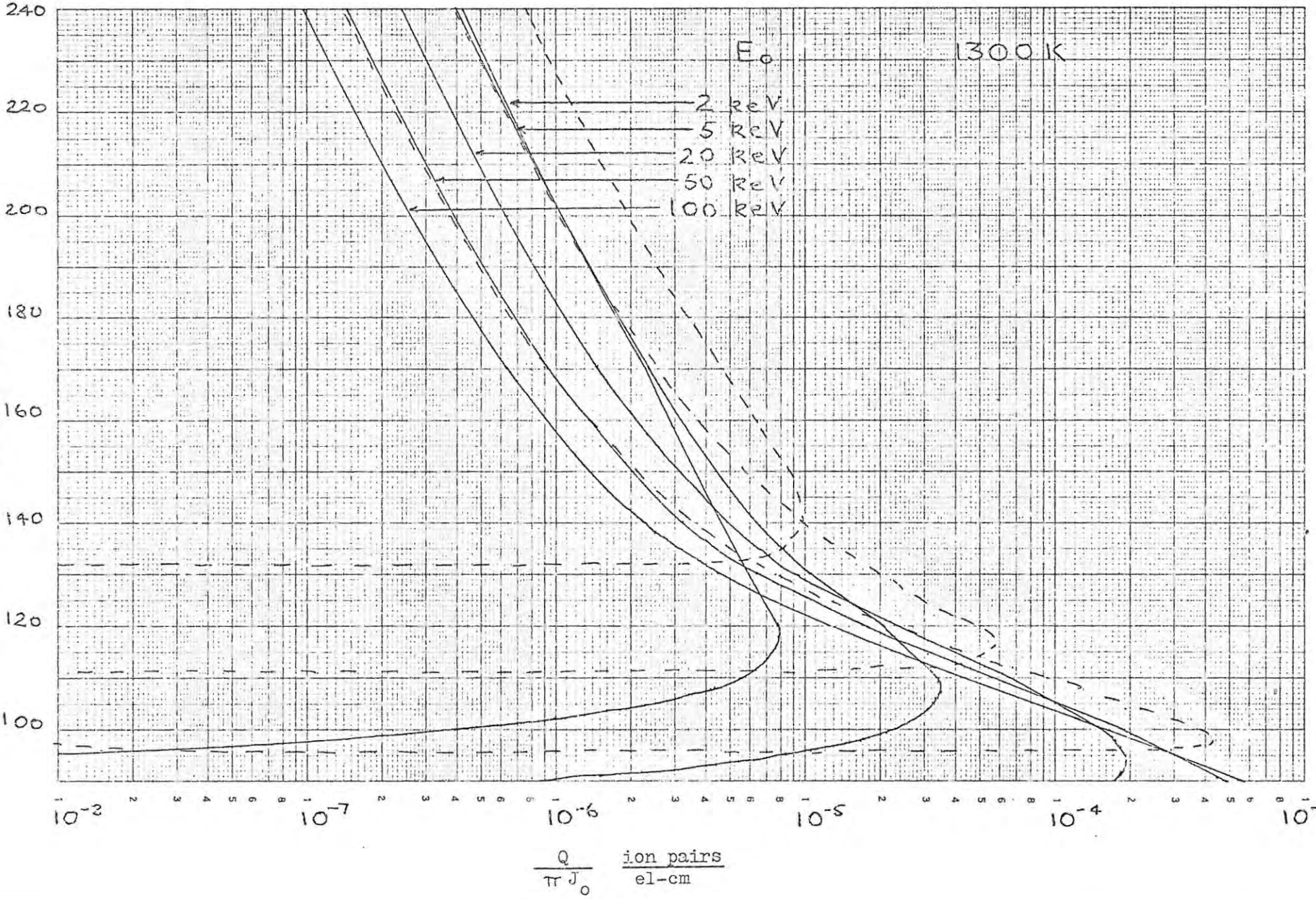

FIG. 8-1

Comparing the dashed lines (E_i) with the solid lines (E_o) shows that in each case the profile for E_o is broader i.e. there is a spread of energies on both sides of the mean thus giving more ionization both above and below the maximum. Because of this the maximum ionization rate is less than that for the monoenergetic case.

Comparing the curves for E_o = 2 keV and E_i = 2 keV it appears that more ionization is produced by the monoenergetic electrons than by the "energy spectra" electrons. The reverse appears to be the case for E_o = 20 kev and E_i = 20 keV. The reason for this lies in our assumption of 2 keV as the average energy per electron of the energy spectrum with e-folding energy 2 keV. This is true if we integrate between the limits 0 and ∞ as shown in (8-5). However our ionization rate profiles are calculated with a lower energy limit of 1 keV i.e. we should use the limits 1 and ∞ in the integral of (8-5). Recalculating using the limits 1 and ∞ we obtain the average energy per electron

$$= e^{-1/E_o} (1 + E_o)$$

For E_o = 2 keV we now have the corresponding $E_i \approx$ 1,8 keV
E_o = 5 keV we now have the corresponding $E_i \approx$ 4,9 keV
E_o = 20 keV we now have the corresponding $E_o \approx$ 20 keV

This means that the E_i curves for 2 and 5 keV are not truly representative of the ionization rate profiles $\frac{Q}{\pi J_o}$ if the lower energy limit is significantly greater than zero. Alternatively, we note that the ionization rate profiles $\frac{Q}{\pi J_o}$ for 2 and 5 keV are not representative if the lower energy limit is not 1. Comparing E_o = 2 keV and E_i = 2 keV it seems that the ionization rate $(\frac{Q}{\pi J_o})$ for E_o = 2 keV would be very much greater if the lower energy limit were 0.

The harder spectra ($>$ 20 keV) are virtually unaffected by increasing the lower limit from 0 to 1 keV.

Figs 8-2 and 8-3 show the dependence of the ionization rate profiles for E_o = 2,5 and 50 keV on T_{exo}. Three values of T_{exo} were chosen namely 900 K, 1300 K and 1700 K. We see that the peak production rates and altitudes are unaffected, probably because they occur below 120 km where the use of the same mean model atmosphere causes negligible difference between results.

VARIATION OF $Q/\pi J_0$ WITH T_{exo}

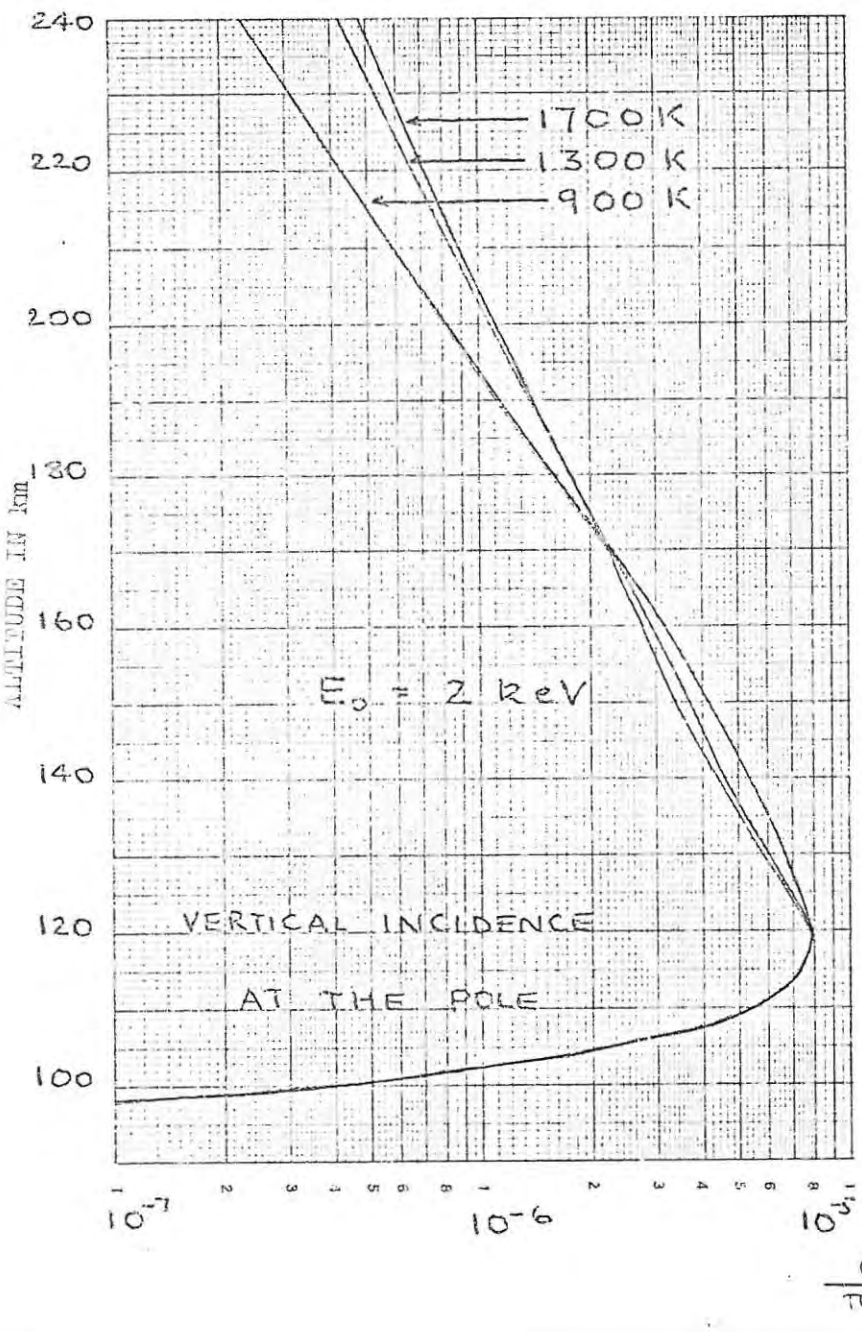

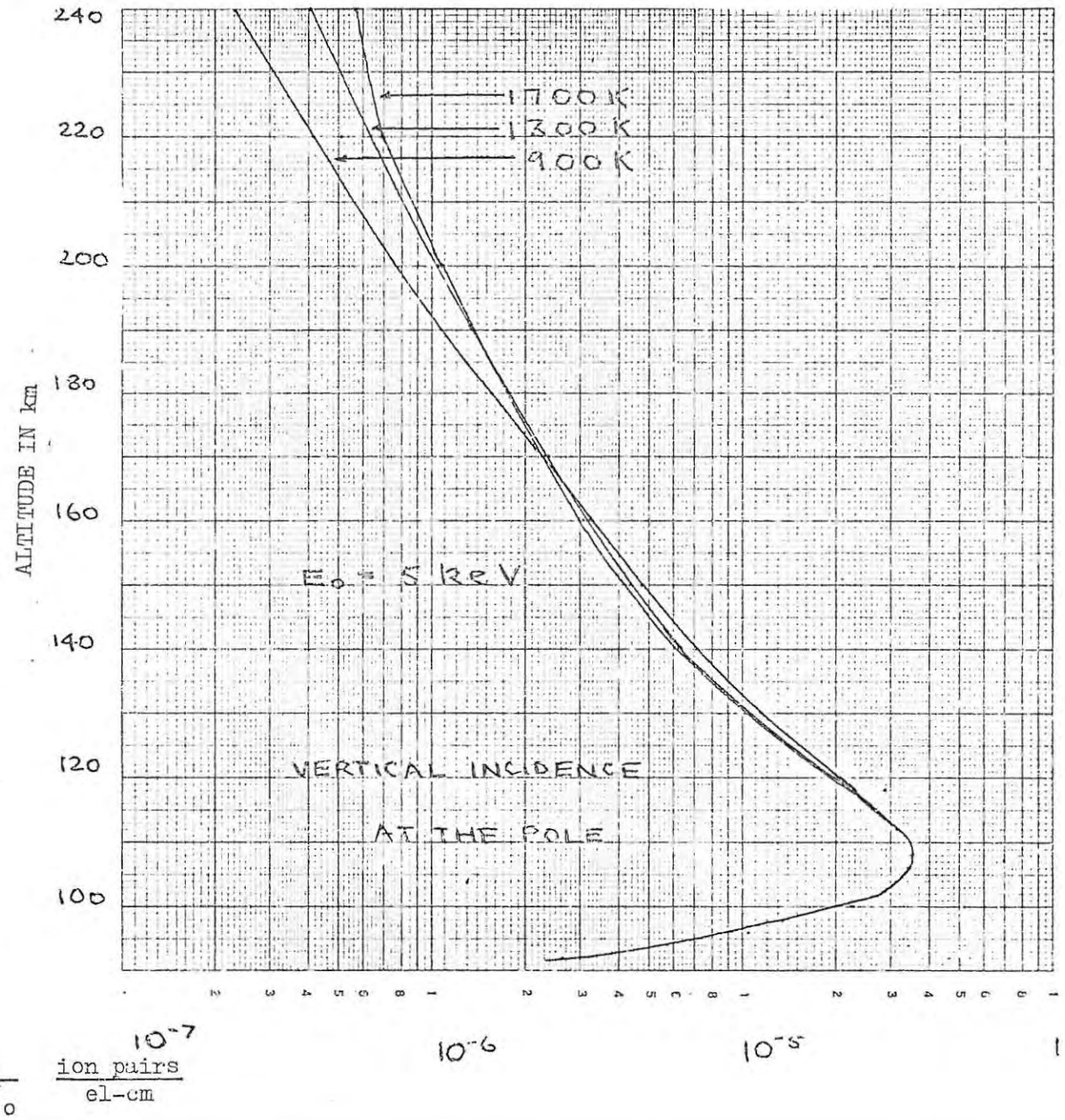

FIG. 8-2

VARIATION OF $Q/\pi J_o$ WITH T_{exo}.

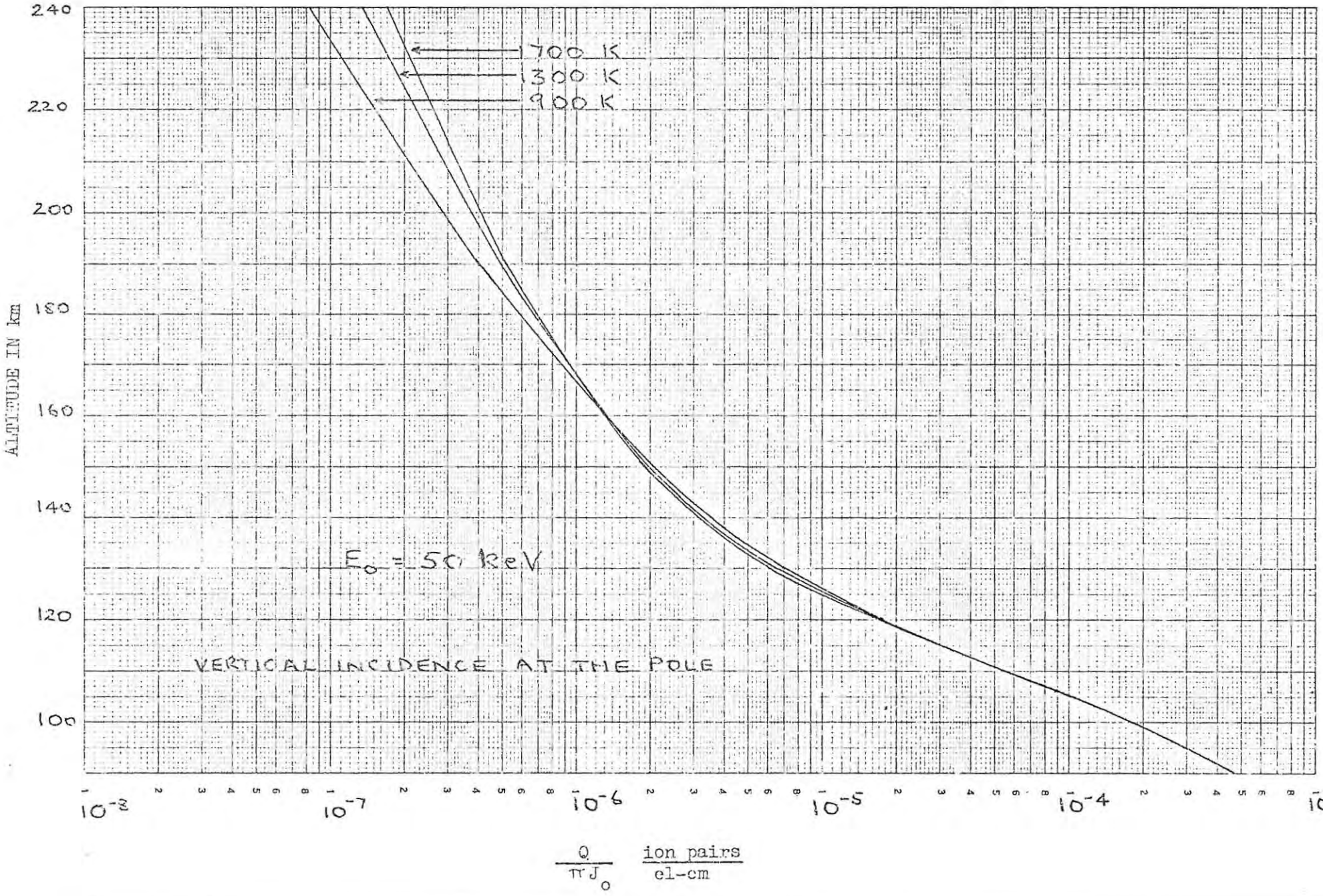

FIG. 8-5

The modification of the shape is similar to that of monoenergetic electrons i.e. more energy is lost at greater altitudes in a "hotter" model atmosphere than would be the case for a cooler model atmosphere. It is interesting to note that the cross-over region in all cases falls between 160 and 190 km. All the profiles converge at 120 km when differences became negligible (a result of using the same model atmosphere below 120 km).

As for the monoenergetic case we find that we cannot ignore the effect of temperature variations on the ionization rate profile in the F region (see Table 8-1).

The influence of dip angle on the ionization rate profiles is shown in Figs 8-4 and 8-5. It is interesting to note that the dip angle exerts only a small amount of influence when the e-folding energy is high (E_o = 50 keV in fig 8-5). For low values of E_o, the dip angle cannot be ignored (Fig. 8-4).

It is of interest to note that decreasing the dip angle does not cause the peak altitude to shift nearly as much as was the case for monoenergetic electrons. When E_o = 2 keV the peak when I = -90^o is $\sim$ 118 km, shifting upwards to $\sim$ 127 km when I = -30^o an increase of 9 km compared with a shift of 20 km when E_i = 2 keV (Chapter 5). When E_o = 5 keV the peak only shifts upwards by about 3 km when I decreases from -90^o to -30^o; for E_i = 5 keV this shift is about 10 km.

Figs 8-6 to 8-9 show typical ionization rate profiles for Sanae for T_{exo} = 900 K, 1200 K and 1700 K for 2,5, 20, 50 and 100 keV).

It is hoped that these may be useful for anyone wishing to study electron precipitation effects at Sanae.

Table 8-1

$\frac{Q}{\pi J_o}$ variation with T_{exo} for different E_o values

E_o	Alt. (km)	900 K	1300 K	1700 K	%age increase from 900 K to 1700 K
2keV	280	8,39(-8)	1,88(-7)	2,41(-7)	187%
	240	2,41(-7)	4,24(-7)	4,84(-7)	101%
	200	8,06(-7)	1,07(-6)	1,10(-6)	36%
5 keV	280	8,01(-8)	1,79(-7)	2,30(-7)	187%
	240	2,30(-7)	4,06(-7)	4,65(-7)	102%
	200	7,75(-7)	1,04(-6)	1,08(-6)	39%
20 kev	280	4,75(-8)	1,07(-7)	1,37(-7)	188%
	240	1,37(-7)	2,42(-7)	2,77(-7)	102%
	200	4,64(-7)	6,27(-7)	6,50(-7)	40%
50 keV	280	2,92(-8)	6,54(-8)	8,40(-8)	188%
	240	8,41(-8)	1,49(-7)	1,70(-7)	102%
	200	2,85(-7)	3,87(-7)	4,02(-7)	41%
100 keV	280	1,93(-8)	4,34(-8)	5,58(-8)	189%
	240	5,58(-8)	9,88(-8)	1,13(-7)	103%
	200	1,90(-7)	2,58(-7)	2,67(-7)	41%

VARIATION OF $Q/\pi J_0$ WITH DIP ANGLE.

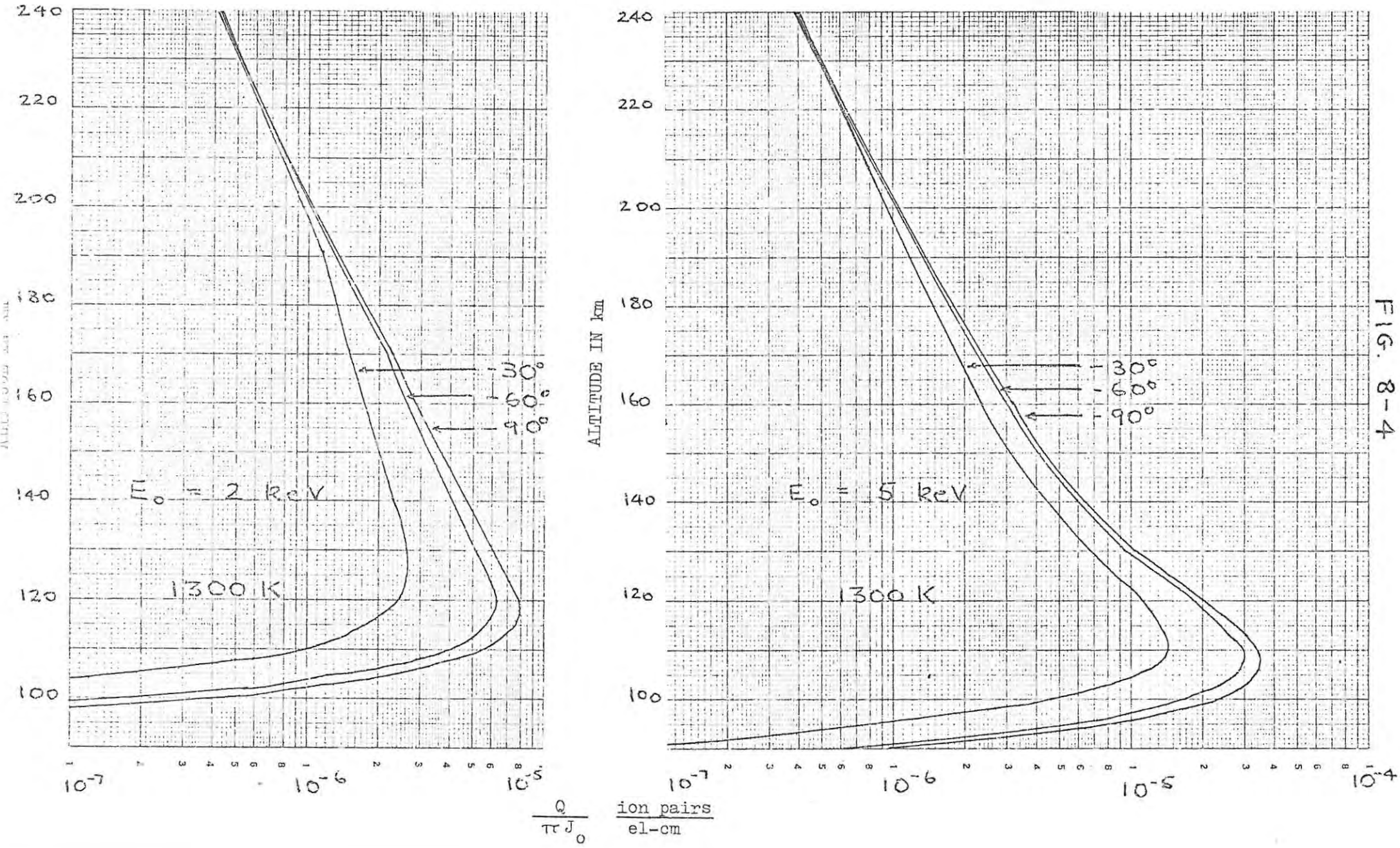

FIG. 8-4

VARIATION OF $Q/\pi J_o$ WITH DIP ANGLE.

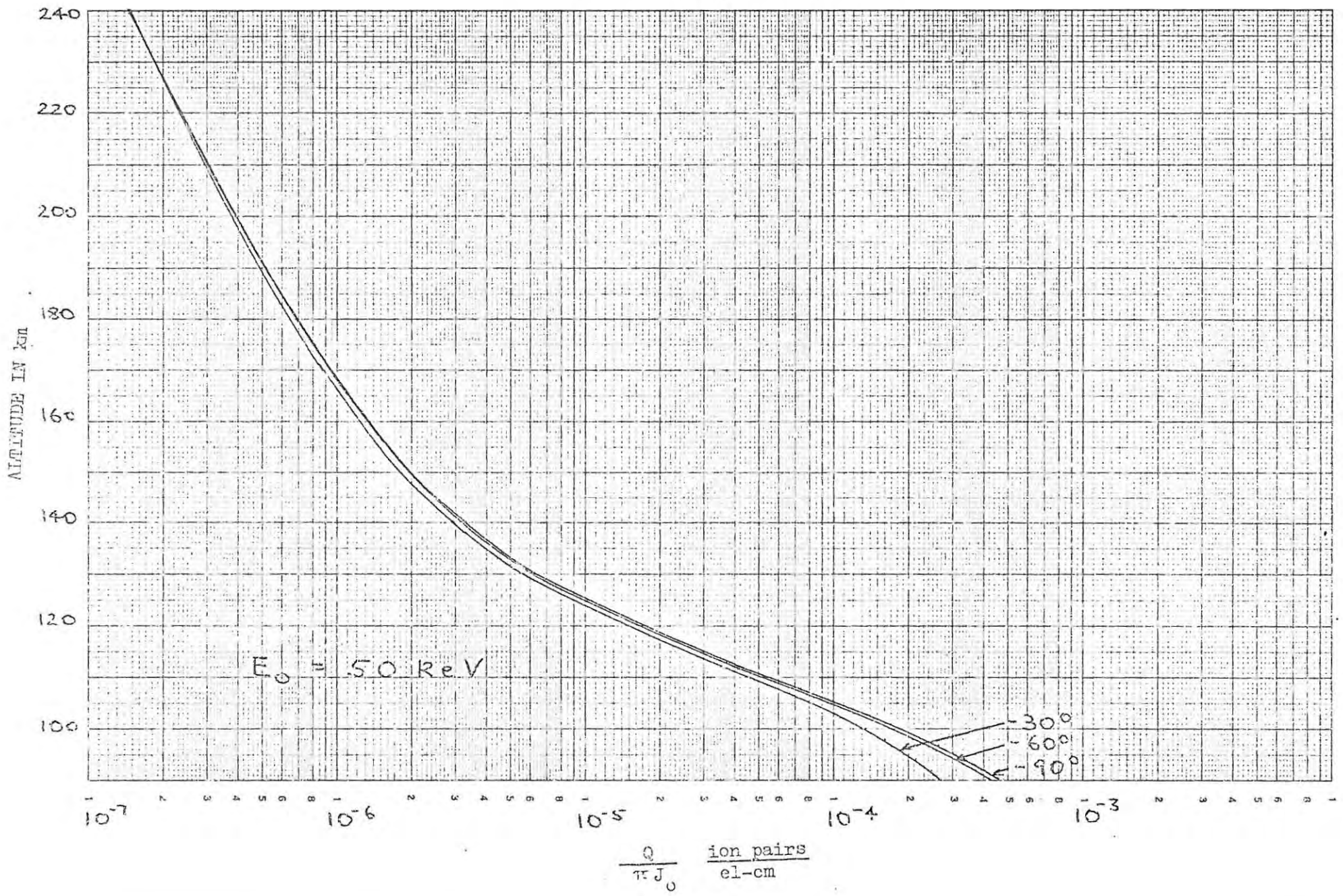

FIG. 8-5

VARIATION OF $Q/\pi J_o$ WITH T_{exo} AT SANAE.

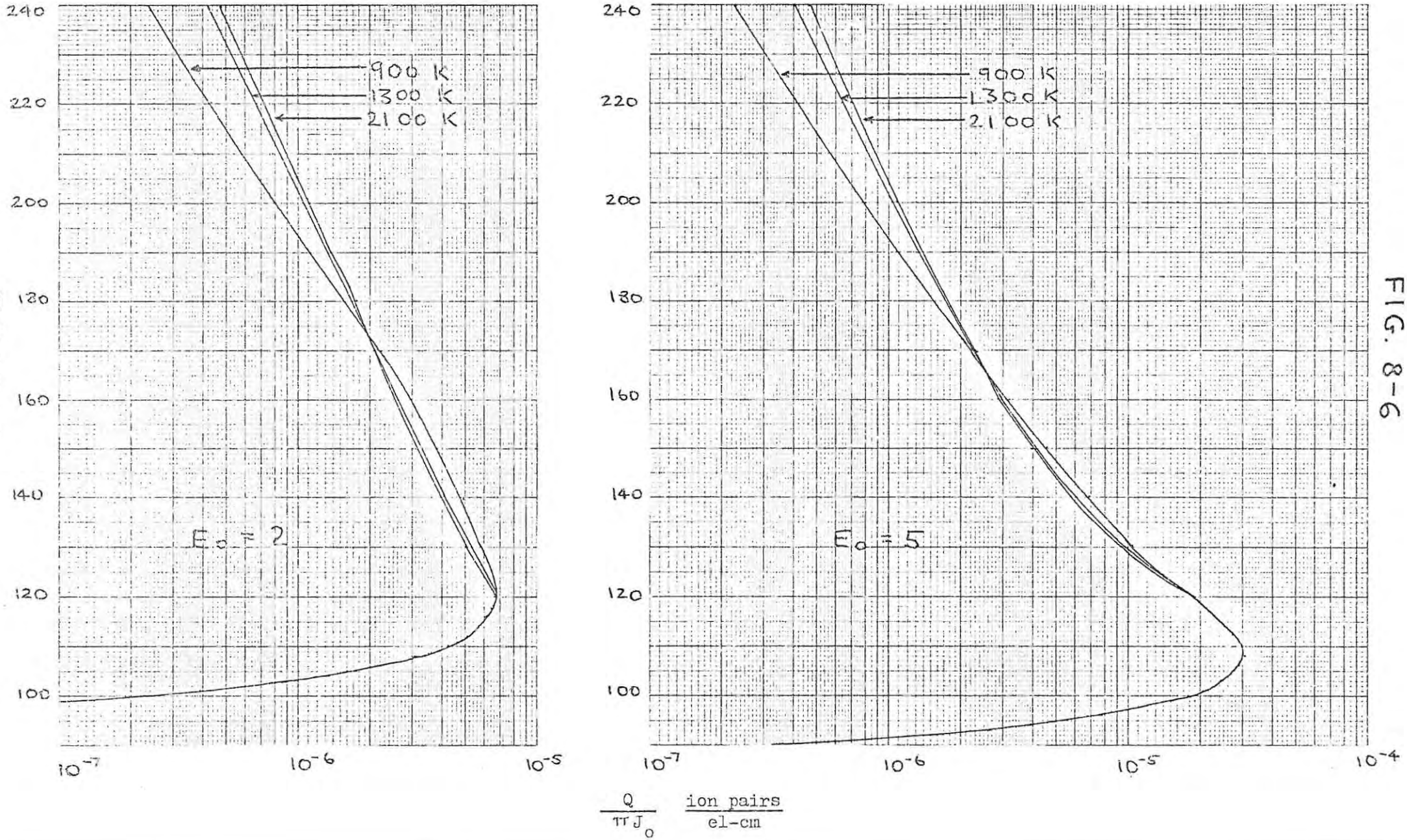

FIG. 8-6

VARIATION OF $Q/\pi J_o$ WITH T_{exo} AT SANAE.

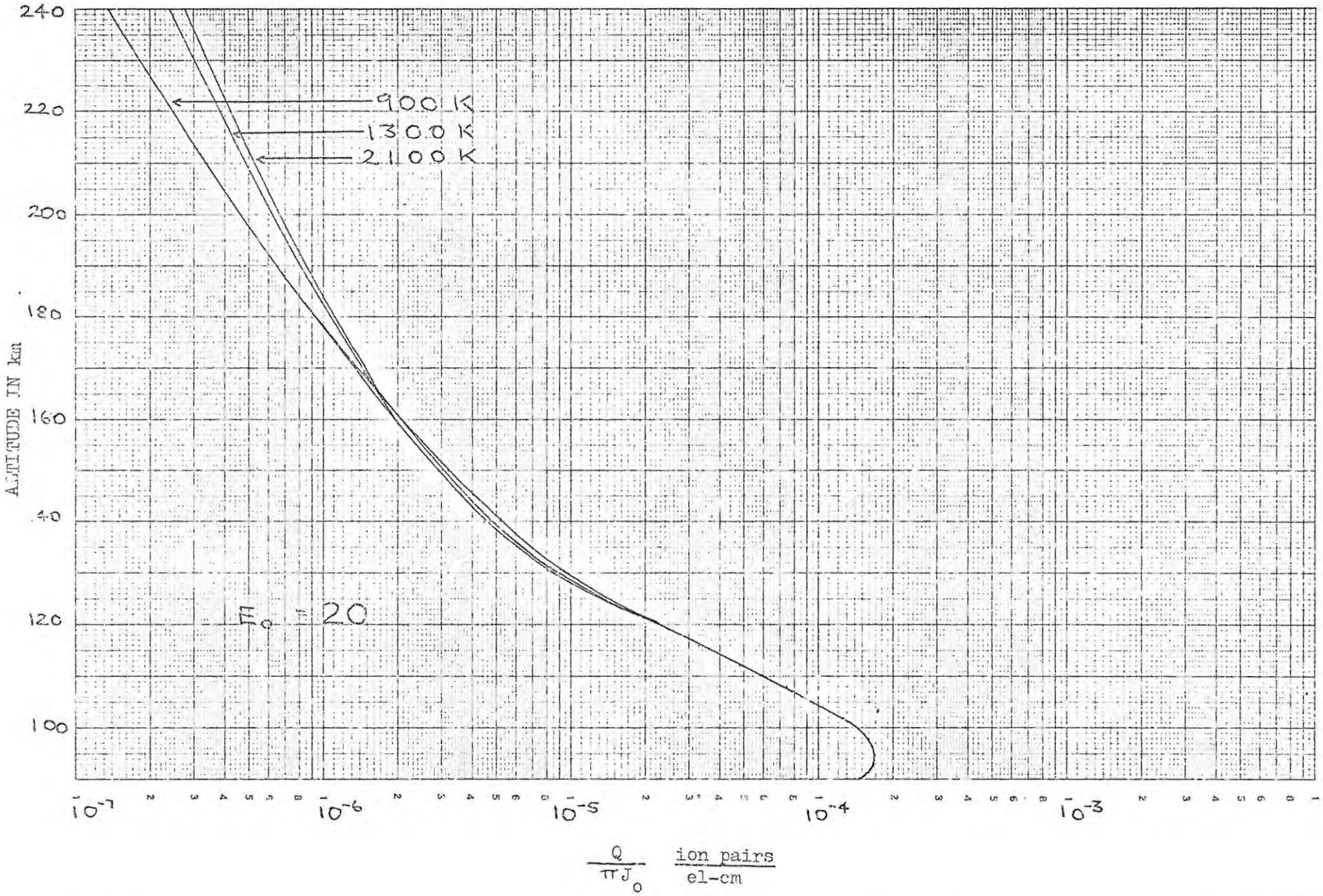

FIG. 8-7

VARIATION OF $Q/\pi J_o$ WITH T_{exo} AT SANAE.

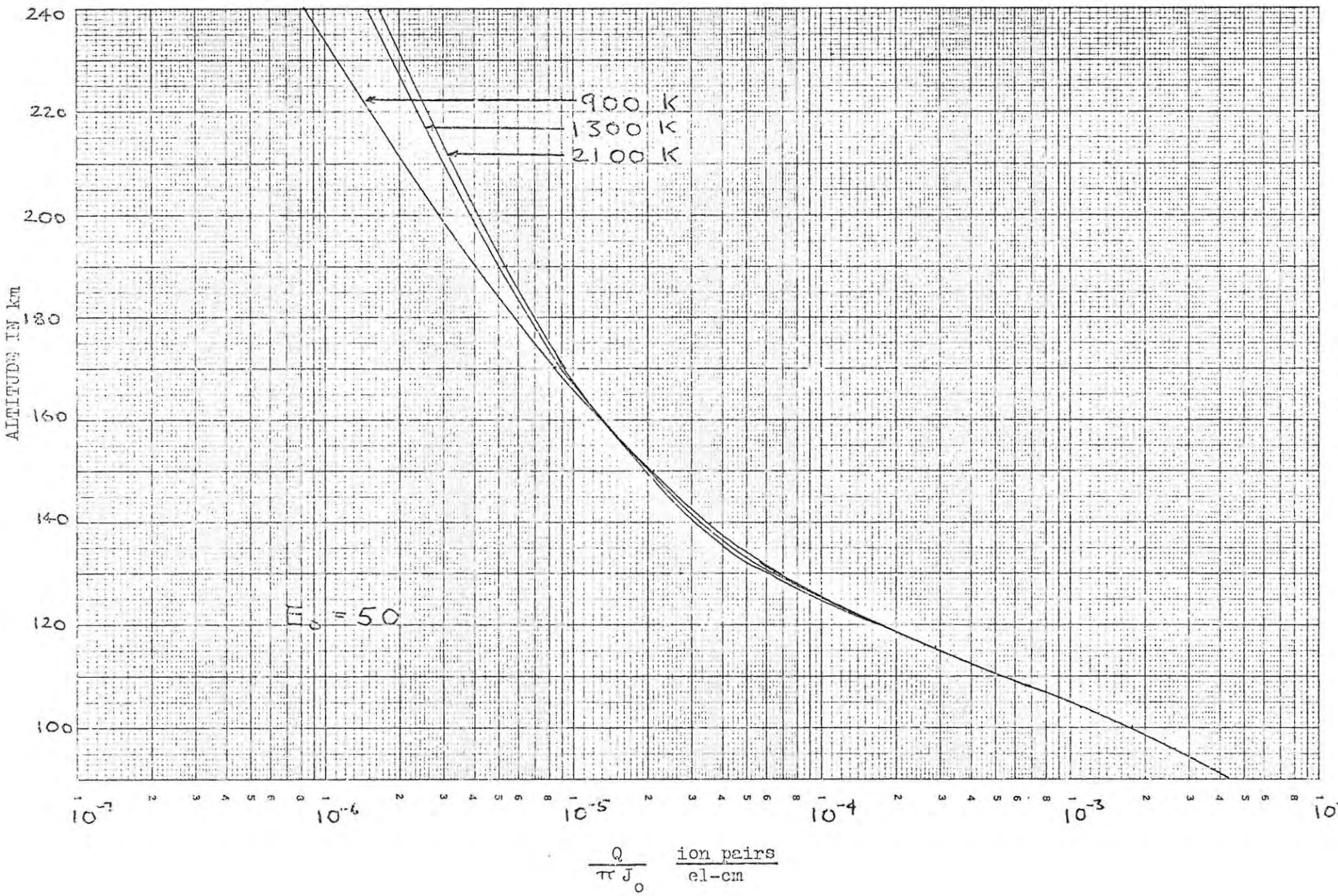

FIG. 8-8

VARIATION OF $Q/\pi J_o$ WITH T_{exo} AT SANAE.

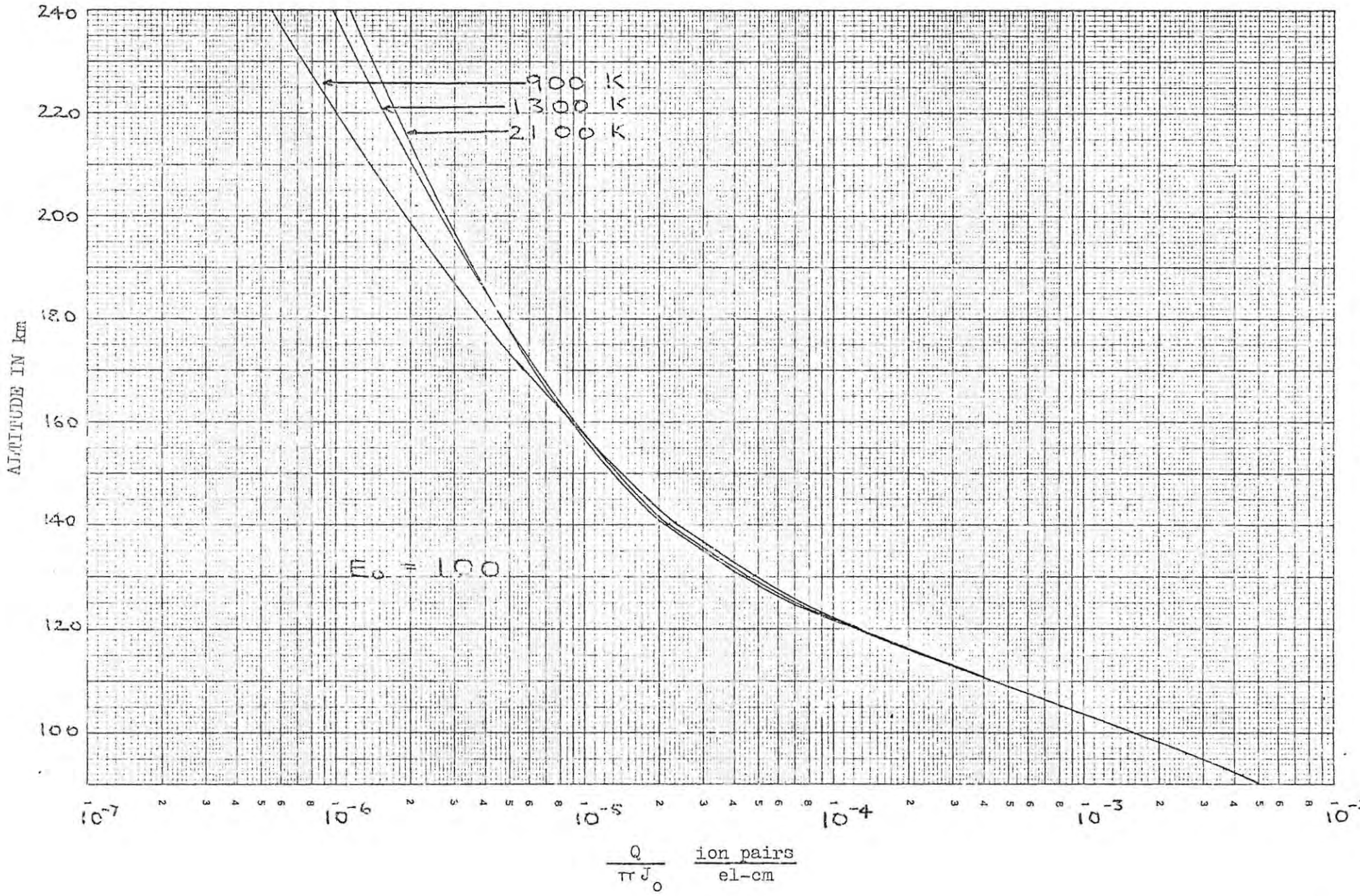

FIG. 8-9

Chapter 9. Conclusions

It is generally felt that the most important aspect in the study of electron precipitation effects in the ionosphere is the accurate determination of electron fluxes. Any large variation in these electron fluxes will outweigh any effect of the model atmosphere on the ionization rate profile. This is the reason why most authors have applied ionization rate profiles calculated in a fixed model atmosphere for any application e.g. Evans et al (1972). While it is obviously true that flux variations are very important the results shown in this thesis seem to indicate that variations in temperature should not be ignored in any calculations of likely ionospheric events caused by precipitated electrons. Baker, Pfister and Ulwick (1967) have reported electron temperatures of up to 3400 K in active auroras and there is undoubtedly some heating of the atmosphere by transfer of energy and this could markedly affect the profile.

The effect of changing the dip angle I of the magnetic field ought not to be ignored, especially when dealing with stations in the vicinity of the South Atlantic Geomagnetic Anomaly which has the effect of giving some high latitude stations mid-latitude dip angle values. This results in an upward shift of the peak and a decrease in the maximum ionization rate. For the investigation of F-region phenomena any dip angle variation may be ignored as it has very little influence in that region.

The results obtained in this thesis are realistic only as far as different parameters used are realistic. This would be especially true when using these results to describe an electron precipitation event.

The assumptions which are made in the AW18 program are:

1. the range-energy relation and the λ-function derived from results published by Berger et al (1970) for the energy range 2-20 keV is applicable throughout the energy range 1-1000 keV.

2. the average energy required to produce one ion pair is 35 eV and this holds throughout the energy range 1-1000 keV.

3. the exospheric temperature and the resulting model atmosphere are representative of conditions during an electron precipitation event. The influences of diurnal, seasonal $F_{10,7}$ solar flux and a_p variations

are calculated from a slightly modified method given by Jacchia (1965) (Appendix 4). These variations of T_{exo} do not include any increase in temperature which we might expect when energetic electrons are precipitated. While Jacchia's model atmosphere does include a small correction for latitude, there is not sufficient data available for high latitude stations in the Southern Hemisphere to be sure that these models would be representative of conditions there.

4. the pitch angle distribution throughout has been assumed to be IDH "at the top of the atmosphere". O'Brien (1971) points out that this may not necessarily be so.

5. the results in chapter 8 are calculated for an integral energy spectrum of the type

$$J_{>E} = J_o \, e^{-E/E_o}$$

O'Brien (1971) published rocket results showing that this may not always be the case. Other publications of a similar nature are those of Eather and Mende (1972) and Riedler (1968).

The next stage in obtaining realistic ionization rate profiles for different energy spectra would involve using actual flux distributions. This could be done by numerical integration and it seems likely that it would be a very profitable line for future research.

Summary

The aim of this thesis was to find a rapid computer program for calculating ionization rate profiles for monoenergetic electrons with an IDH pitch angle distribution, and to extend this to include calculations of profiles for an electron flux with a given energy spectrum. The method used is basically that of Rees (1963) but altered to give agreement with the results of Berger, Seltzer and Maeda (1970). The final method was chosen after a detailed comparitive study had been made of available literature.

The effect of different Jacchia/CIRA model atmospheres on the ionization rate profile was investigated and it was found that more ionization is produced in the F-region when the atmosphere is "hotter". The peak altitude and peak production rate varied in a regular manner when T_{exo} was changed.

The normalized ionization rate profiles for different energies and model atmospheres fell on the same curve which was found to be described by a relationship of the type

$$Q = (1 + 0{,}109X - 0{,}155X^2 + 0{,}078X^3) \exp(1 - X - e^{-X})$$ where X is the scaled height. This provides us with a "ready-reckoner" for calculating approximate ionization rate profiles.

Decreasing the dip angle of the magnetic field had the effect of increasing h_m and decreasing q_m/F in a regular manner. This effect of the dip angle played a most important part on ionization rate profiles for stations at different latitudes. The effect of latitude on the model atmosphere was very small and this had little influence on the profile.

Seasonal and diurnal changes at Sanae were found to have little influence on the ionization rate profile as did the geomagnetic activity index. Large variation of 10,7 cm solar flux had a marked influence on the ionization rate profiles.

Profiles were also calculated for a flux distribution of the type $J_{>E} = J_o e^{-E/E_o}$. The results of changing the e-folding energy, model atmosphere and dip angle were also investigated. In appearance the changes were similar to those for monoenergetic fluxes but the magnitudes were different. Profiles are also included in this thesis for different e-folding energies in different model atmospheres at Sanae.

References

Alfven, H.	1950	Cosmical Electrodynamics (Oxford Univ. Press. London).
Bailey, D.K.	1968	Rev. Geophysics 6, 289-346.
Baker, K.D., Pfister, W. and Ulwick J.C.	1967	Space Research VII 665-672.
Berger, M.J., Seltzer, S.M. and Maeda K.	1970	J.A.T.P. 32, 1015-1045.
Bethe, H.	1953	Phys. Rev. 89, 1256-1266.
Blamont J.E. and Chanin-Lory, M.L.	1965	Space Research V, 313-317.
Blunck, O. and Liesegang, S.	1950	Ziets. Phys. 128, 500-505.
Burch, J.L.	1968	J.G.R. 73, 3585-3591.
Cain, J.C. and Neilon, J.R.	1963	J.G.R. 68, 4689-4696.
Chamberlain, J.W.	1961	Physics of Aurora and Airglow (Academic Press. New York).
CIRA	1965	COSPAR International Reference Atmosphere. North-Holland, Amsterdam.
Christensen, A.B. and Karas, R.	1970	J.G.R. 75 4266-4278.
Eather, R.H. and Mende, S.B.	1972	J.G.R. 77, 660-673.
Evans, D.S.	1968	J.G.R. 73, 2315-2323.
Evans, D.S., Jacobsen, T., Maehlum, B.N., Skolvi, G. and Wedde, T.	1972	Plan. Space Science 20 233-252.
Freyer, G.J. (III)	1969	Bremstrahlung in the Lower Ionosphere. Penn. State Univ. (Ionosph. Res.) Sc. Report 336.
Galperin Yu.I and Tomny, V.V.	1968	Space Research VIII 130-138.
Gibson, Sr. Jean and Van Allen, J.A.	1970	Correlation of X-ray radiation (2-12 A^{o}) with Microwave Radiation (10,7 cms) from the Non-Flaring Sun. Univ. of Iowa Research Report 70:5.
Gledhill, J.A.	1970	An Ionospheric Event Apparently due to Electrons Precipitated from the Radiation Belt at L = 4. Paper read at IUCSTP Symposium, Leningrad, 1970.

Gledhill, J.A., and Torr, D.G.	1966	Space Research VI, 222-229.
Gledhill, J.A., Torr, D.G. and Torr, M.R.	1967	J.G.R. 72, 209-214.
Gledhill, J.A. and Van Rooyen, H.O.	1963	The South Atlantic Geomagnetic Anomaly and the Radiation Belts. Proc. 5th. Inst. Symp. on Space Technol. and Sci., Tokyo. 1003-1010, 1963.
Goudsmit, S. and Saunderson, J.L.	1940	Phys. Rev. 57, 24-29.
Grün, A.E.	1957	Z. Naturforschung 12a, 89-95.
Herman, J.R., and Chandra, S.	1969	Plan. Space Science 17, 815-840.
Hess, W.N., Trichel, M.C., Davis, T.N., Beggs, W.C., Kraft G.E., Stassinopoulos,E. and Maier, E.J.R.	1971	J.G.R. 76, 6067-6081.
Hultqvist, B.	1965	Space Research V, 91-117.
Ivanov-Kholodny, G.S.	1965	Space Research V, 19-42.
Jacchia, L.G.	1965	Smithsonian Contributions to Astrophysics. Vol. 8 no 9.
Jacchia, L.G. and Slowey, J.	1967	Space Research VII Vol. 2. 1077-1090.
Jacobs, K.G., Kist, R. and Rawer, K.	1969	Space Research IX, 246-255.
Kamiyama, H.	1966	Report of Ionosph. and Space Res. Japan. 20, 374-394.
Krassovsky, V.I., Truttse Yu. L. and Shefov, N.N.	1965	Space Research V, 43-48.
Lauter, E.A. and Knuth, R.	1965	Space Research V, 325
Maeda, K.	1965	J.A.T.P. 27 259-275.
Maehlum, B.	1967	J.G.R. 72 2287-2299.
Maehlum, B.	1968	J.G.R. 73 3459-3468.
Mott, N.F.	1929	Proc. Roy. Soc. A124 425.
Nesterov, G., Krivsky, L., and Letfus, V.	1964	Geomag. and Aeron. 4 822-824.
O'Brien, B.J.	1962a	J.G.R. 67 1227-1233.

O'Brien, B.J.	1971	J.A.T.P. 33 679-684.
O'Brien, B.J. and Taylor, H.	1964	J.G.R. 69, 45-63.
Oguti, T. and Marubashi, K.	1966	Report of Ionosph. and Space Res. Japan. 20 96-100.
Ondoh, T.	1966	Report of Ionosph. and Space Res. Japan. 20 79-83.
Rees, M.H.	1963	Plan. Space Science 11 1209-1218.
Rees, M.H.	1964b	Plan. Space Science 12 722-725
Reidler W.	1968	Space Research VIII 195-200.
Spencer, L.V.	1955	Phys. Rev. 98 1597-1615.
Spencer L.V.	1959a	NBS Monograph 1 U.S. Dept. of Commerce, Washington D.C.
STP Notes.	1969	No. 4.
Torr, D.G. and Torr, M.R.	1967a	Nature 216 1193-1194.
Torr, D.G. and Torr, M.R.	1967b	C.S.I.R. Res. Report. No. 263. Pretoria.
Torr, M.R. and Torr D.G.	1968a	Nature 217 45
Torr, M.R. and Torr D.G.	1968b	C.S.I.R. Res. Report No. 271, Pretoria.
Torr, D.G. and Torr, M.R.	1969a	Ann. Geophys. 25 571-575
Torr, M.R. and Torr, D.G.	1969b	J.A.T.P. 31 611-614
Torr, D.G. and Torr, M.R.	1970	J.A.T.P. 32 15-34.
Ulwick, J.C., Reidy, W.P. and Baker, K.D.	1967	Space Research VII 656-664
WDCA	1971	World Data Center A. Catalogue of Data. August 1971.
Yonezawa, T.	1965	Space Research V 49-60.

APPENDIX 1

Particle Fluxes by J.A. Gledhill

We consider a space in which particles are moving. Let us set up a cartesian co-ordinate system with a convenient origin and consider a point P, denoted by the vector $\vec{r}$ to the point (x; y; z). Consider an element of area δ A at P (Fig. 1) represented also by the vector $\vec{\delta A}$ perpendicular to it as shown, the orientation of the surface being arbitrary. We now confine our attention to particles of one species only, with energies lying in the range E to E + δ E, approaching δ A from directions which lie in the element of solid angle $\delta \Omega$, which is centred on the unit vector $\vec{u}$, which makes an angle Θ with $\vec{\delta A}$. Let δ N such particles cross the surface element δ A in time δ t.

Since the effective area of δ A as seen from the direction of arrival of the particles $\vec{-u}$ is δ A cos Θ , we may write

$$\delta N = j(\vec{r}, \vec{u}, E, t)\, \delta A \cos\Theta\, \delta\Omega\, \delta E\, \delta t \qquad (1)$$

where j $(\vec{r}, \vec{u}, E, t)$ is a distribution function which takes account of the dependence on the bracketed variables. Note that if cos Θ = 1, i.e. if δ A is perpendicular to $\vec{u}$, we could write

$$\frac{\delta N}{\delta A \delta\Omega\ \delta E\ \delta t} = j\,(\vec{r}, \vec{u}, E, t) \qquad (2)$$

so that j is the number of particles which cross δ A per unit area per unit solid angle per unit energy per unit time from the direction $\vec{u}$ when δ A is oriented perpendicular to this direction. j is called the directional flux density.

Consider now the case where we are dealing with electrically charged particles and there is a magnetic field $\vec{B}$. Set up cartesian axes at the point P as shown in Fig. 2, choosing the z axis to lie along the direction of $\vec{B}$. Now let δ A lie in the x y plane, so that it is perpendicular to $\vec{B}$. Now erect a unit sphere round P and let Θ, φ be the polar coordinates of the unit vector $\vec{u}$. Then the element of solid angle $\delta \Omega$ in our previous discussion becomes the solid angle between Θ and $\Theta + \delta\Theta$, φ and $\varphi + \delta\Theta$ and is given by

$$\delta\Omega = \sin\Theta \; \delta\Theta \; \delta\varphi \qquad (3)$$

We may substitute this in (1) and write

$$\delta N = j(\vec{r}, \Theta, \varphi, E, t) \, \delta A \cos\Theta \sin\Theta \, \delta\Theta \, \delta\varphi \, \delta E \, \delta t \qquad (4)$$

since $\vec{u}$ and $\delta\Omega$ are now related by (3). Note that Θ is now the pitch angle of the charged particles.

Isotropic case

If j is independent of φ (i.e. there is no "cyclotron bunching" (Roederer, 1970)), we can integrate (4) over φ to get

$$\delta N(\vec{r}, \Theta, E, t) = 2\pi \, j(\vec{r}, \Theta, E, t) \, \delta A \cos\Theta \sin\Theta \, \delta\Theta \, \delta E \, \delta t \qquad (5)$$

If j is also independent of Θ the flux is said to be isotropic at the point P and we may integrate over Θ :

$$\delta N(\vec{r}, E, t) = j(\vec{r}, E, t) \, 2\pi \, \delta A \, \delta E \, \delta t \int_0^{\pi} \sin\Theta \cos\Theta \, d\Theta$$

$$= 0$$

showing that the net flux through δA is zero, as we should expect since equal numbers of particles go through it upwards and downwards in δt.

If we are interested only in the downward flux through δA, we integrate only between $\Theta = 0$ and $\Theta = \pi/2$, obtaining:

$$\delta N'(\vec{r}, E, t) = j(\vec{r}, E, t) \, 2\pi \, \delta A \, \delta E \, \delta t \int_0^{\pi/2} \sin\Theta \cos\Theta \, d\Theta$$

$$= \pi \, j(\vec{r}, E, t) \, \delta A \, \delta E \, \delta t \qquad (6)$$

This is the case referred to as isotropic over the downward hemisphere or IDH. The number of particles travelling downward per unit area per unit energy per unit time (the differential downward flux density is

$$\frac{\delta N'(\vec{r}, E, t)}{\delta A \, \delta E \, \delta t} = \pi \, j(\vec{r}, E, t) \qquad (7)$$

where j is the (isotropic) directional flux density.

Omnidirectional flux

If we have a region of space in which there is an isotropic particle flux with directional flux density $j(\vec{r}, E, t)$, we may calculate the total flux into a sphere of radius ρ. Energy element of area δA of the surface of the sphere is crossed by a number of particles $\delta N'(\vec{r}, E, t)$ given by (6), coming from all directions but going inward into the sphere. Since the flux is isotropic the orientation of δA is immaterial and we have

$$\delta N''(\vec{r}, E, t) = \pi j(\vec{r}, E, t)\, \delta E\, \delta t\, 4\pi\rho^2$$

$$= 4\pi^2 \rho^2 j(\vec{r}, E, t)\, \delta E\, \delta t \qquad (8)$$

for the total number of particles in the energy range δE which would be counted in time δt by an omnidirectional spherical counter of radius ρ at the point P. We can write (8) in the form

$$\delta N''(\vec{r}, E, t) = 4\pi(\pi\rho^2)\, j(\vec{r}, E, t)\, \delta E\, \delta t$$

$$= (\pi\rho^2)\, J(\vec{r}, E, t)\, \delta E\, \delta t$$

So that the counting rate per unit time per unit energy of a spherical omnidirectional counter of unit cross sectional area ($\pi\rho^2 = 1$) at P would be

$$\frac{\delta N''(\vec{r}, E, t)}{\delta E\ \delta t} = J(\vec{r}, E, t) \qquad (9)$$

which defines the differential omnidirectional flux density $J(\vec{r}, E, t)$.

Energy integration

Clearly, since E is an independent variable, we can integrate any of the equations such as (1), (4), (6) or (9) with respect to energy over a convenient range (commonly $> E_o$, where E_o is the counter threshold) to get the corresponding expressions for the integral directional, IDH and omnidirectional flux densities $j_{>E_o}$, $J_{>E_o}$, etc.

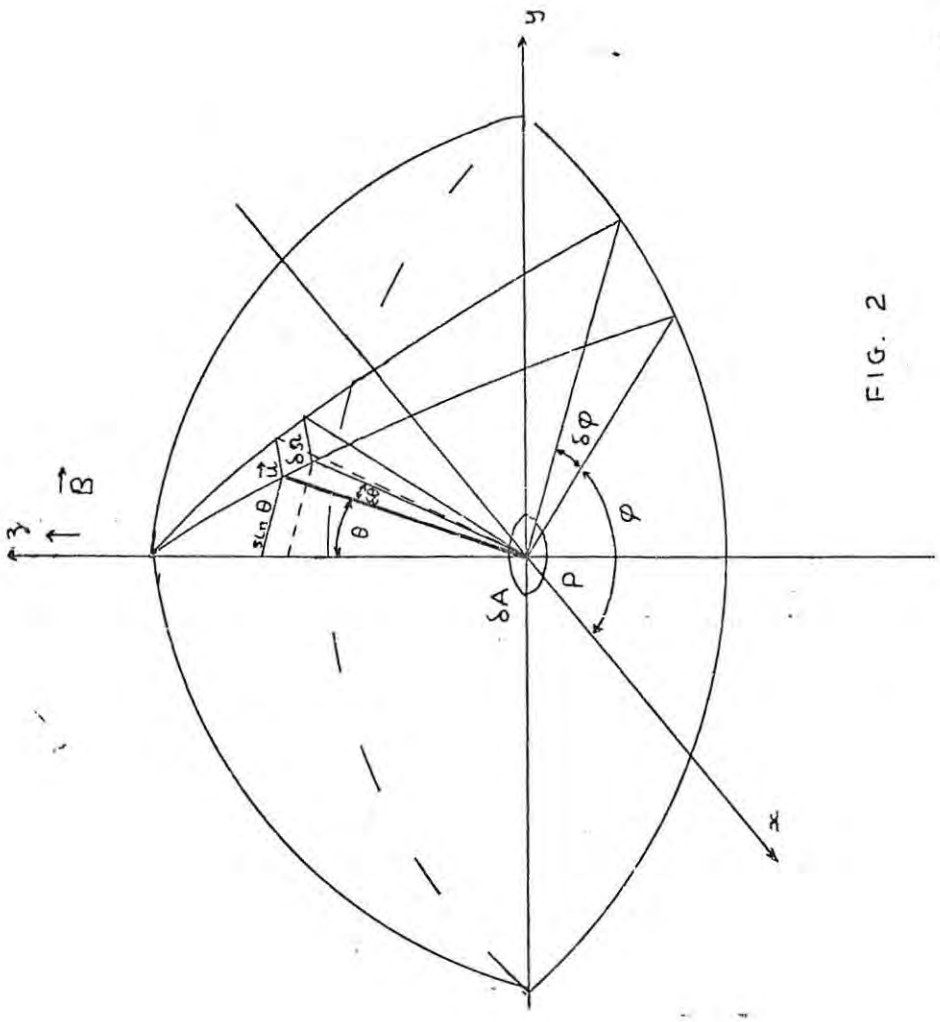

FIG. 2

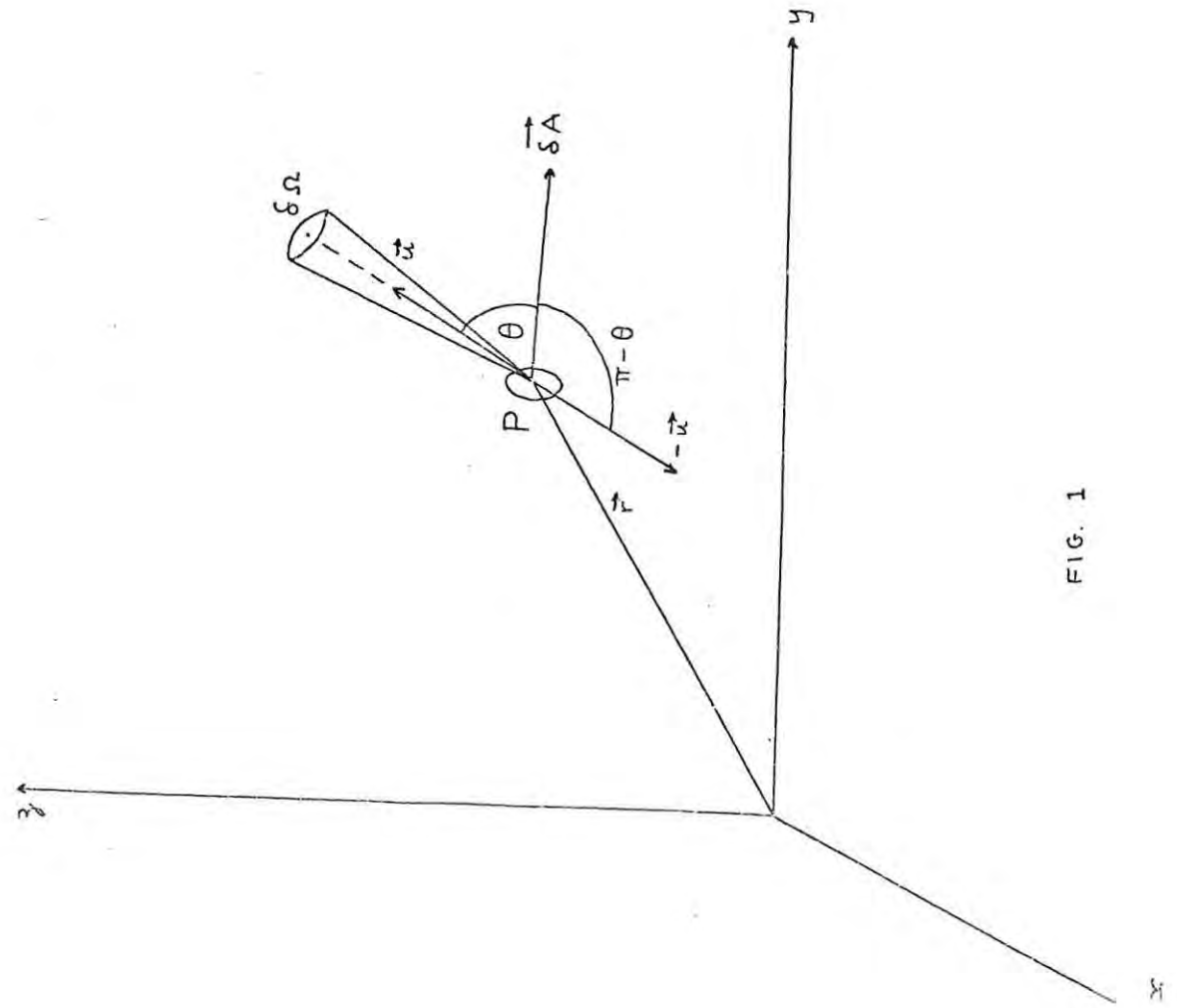

FIG. 1

APPENDIX 2

Consider two altitude levels h_{n-1} and h_n (with respective mass densities $D(h_{n-1})$ and $D(h_n)$) as shown. We wish to find the average density within the lamination.

We assume an exponential distribution of the mass density with height within the lamination although this is not true for the atmosphere as a whole.

We therefore have $D(h_n) = D(h_{n-1}) \exp\left[-\gamma(h_n - h_{n-1})\right]$ if ds is the element of path length in km and we regard dh/ds constant with the lamination.

$$\bar{D} \overset{\text{def}}{=} \frac{\int D\,ds}{\int ds} \approx \frac{\int D\,dh}{\int dh}$$

$$= \frac{1}{\Delta h} \int_{h_{n-1}}^{h_n} D(h_{n-1})\, e^{-\gamma(h_n - h_{n-1})}\,dh$$

$$= \frac{D(h_{n-1})}{h_n - h_{n-1}} \int_{h_{n-1}}^{h_n} e^{-\gamma(h_n - h_{n-1})}\,dh$$

$$= \frac{D(h_n) - D(h_{n-1})}{(h_n - h_{n-1})\gamma}$$

but $\log_e \frac{D(h_{n-1})}{D(h_n)} = -\gamma(h_n - h_{n-1})$

$$\therefore \quad \bar{D} = \frac{D(h_{n-1}) - D(h_n)}{\log_e D(h_{n-1})/D(h_n)}$$

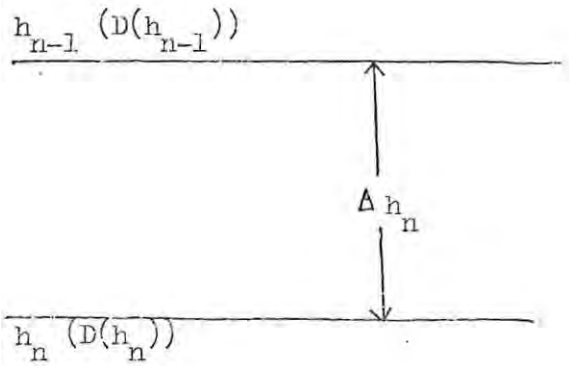

APPENDIX 3

AW18

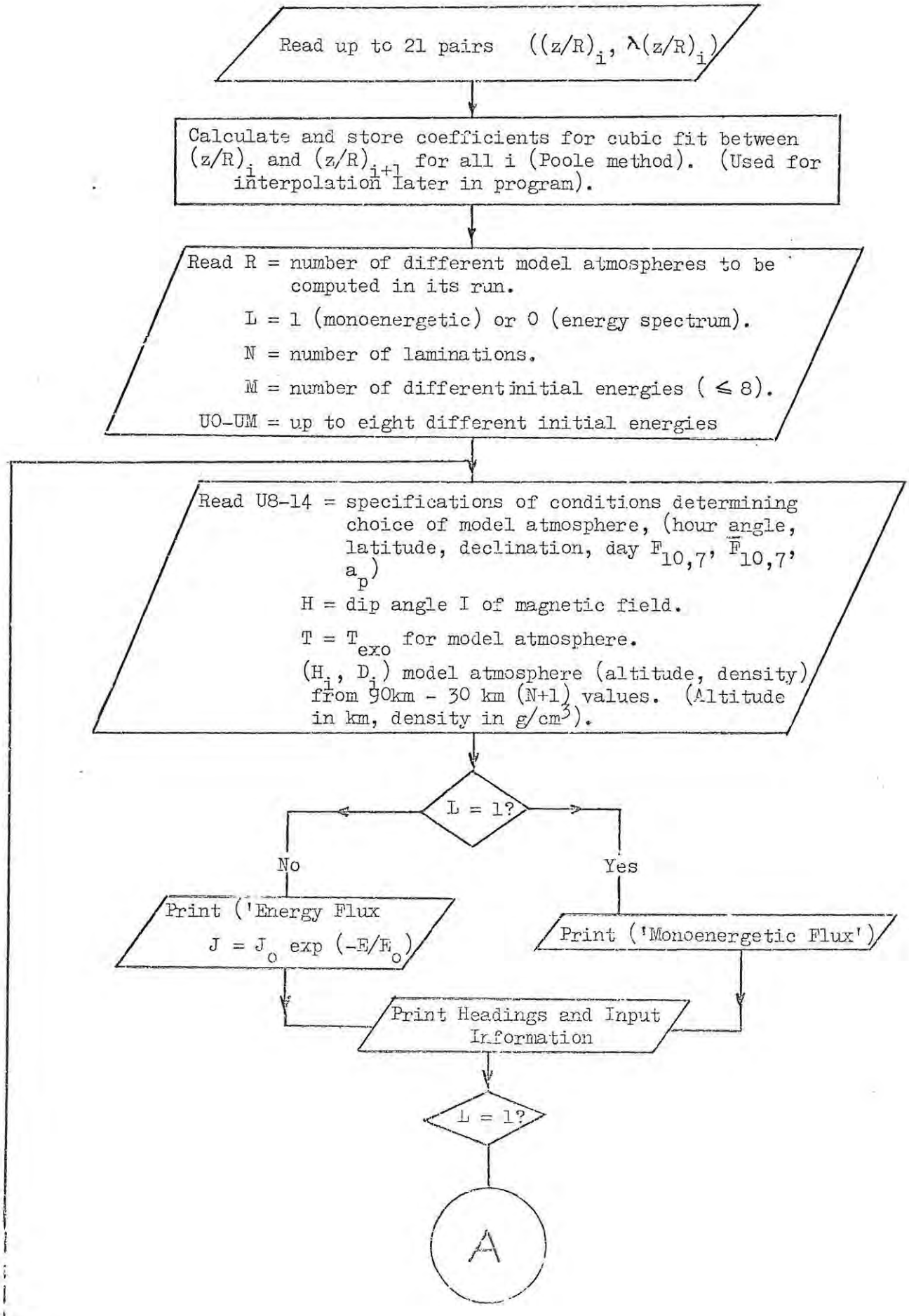

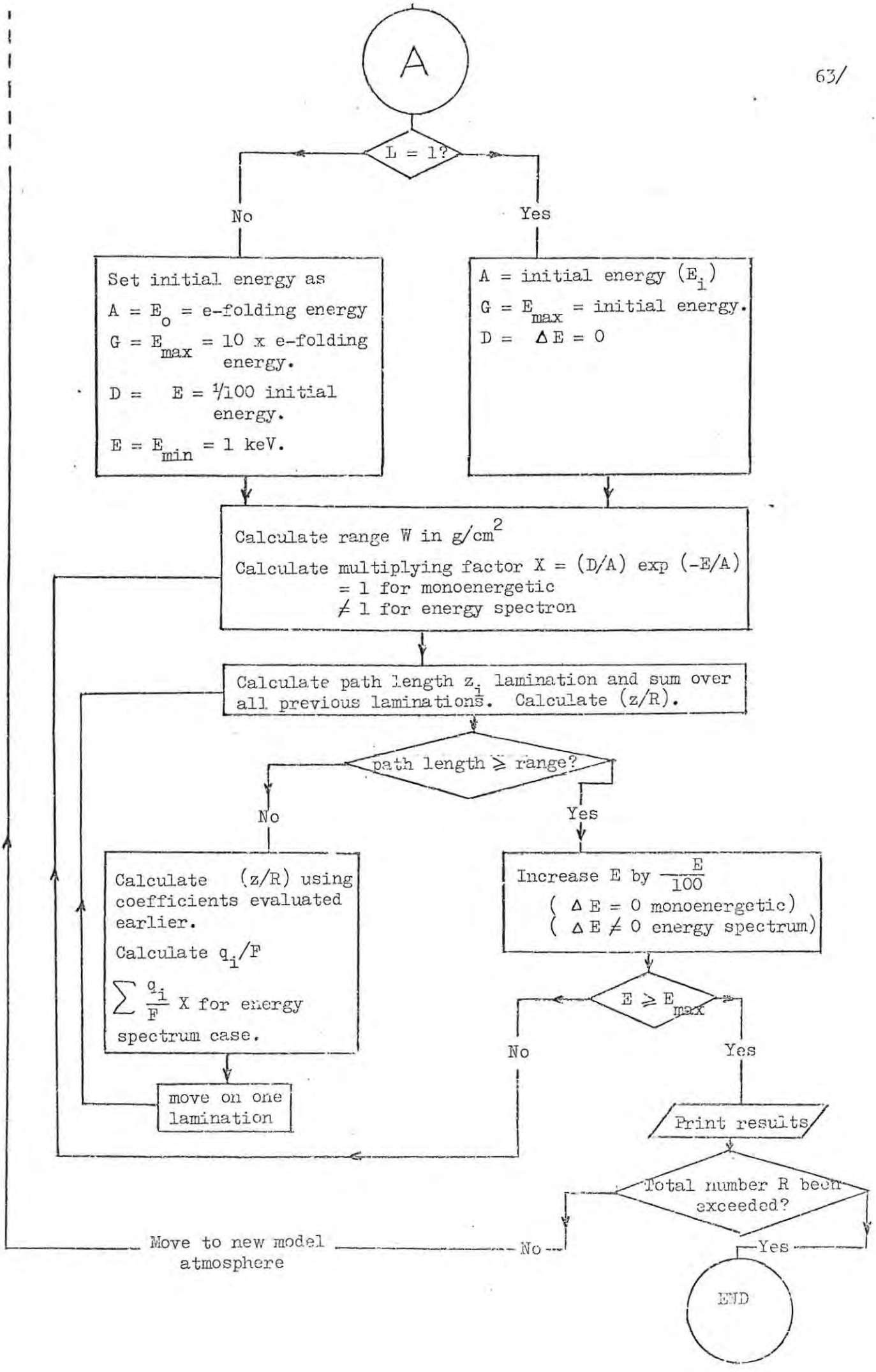
A
L = 1?
No
Yes
Set initial energy as
A = E_o = e-folding energy
G = E_max = 10 x e-folding energy.
D = E = 1/100 initial energy.
E = E_min = 1 keV.
A = initial energy (E_i)
G = E_max = initial energy.
D = ΔE = 0
Calculate range W in g/cm^2
Calculate multiplying factor X = (D/A) exp (-E/A)
= 1 for monoenergetic
≠ 1 for energy spectron
Calculate path length z_i lamination and sum over all previous laminations. Calculate (z/R).
path length ≥ range?
No
Yes
Calculate (z/R) using coefficients evaluated earlier.
Calculate q_i/F
Σ q_i/F X for energy spectrum case.
move on one lamination
Increase E by E/100
(ΔE = 0 monoenergetic)
(ΔE ≠ 0 energy spectrum)
E ≥ E_max
No
Yes
Print results
Total number R been exceeded?
No
Yes
Move to new model atmosphere
END

APPENDIX 4

Program Jacchia Atm (for calculating T_{exo}) (taken from a section of Howard William's Program) eqn numbers refer to equation in Jacchia (1965).

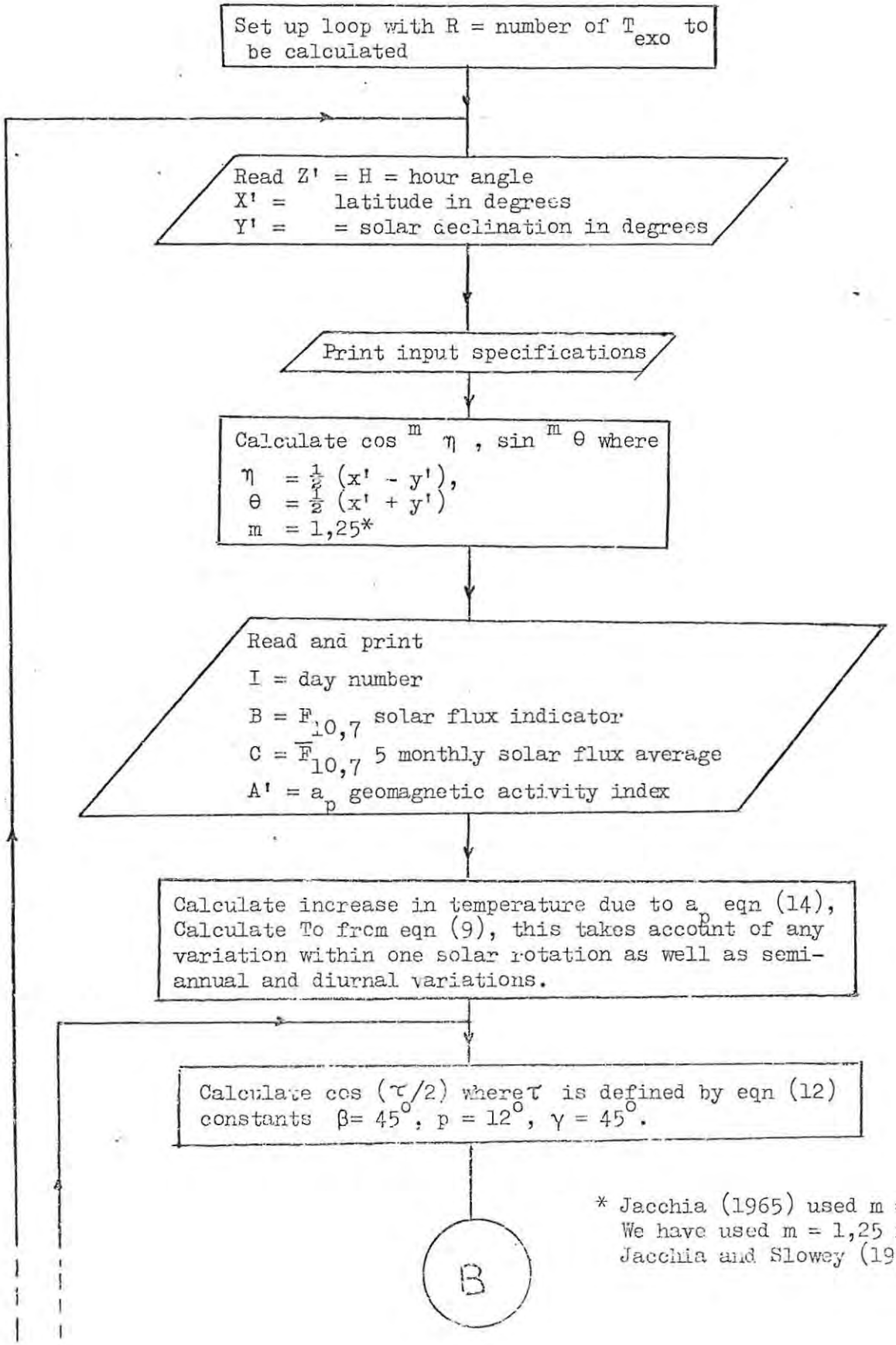

* Jacchia (1965) used m = 2,5. We have used m = 1,25 from Jacchia and Slowey (1967).

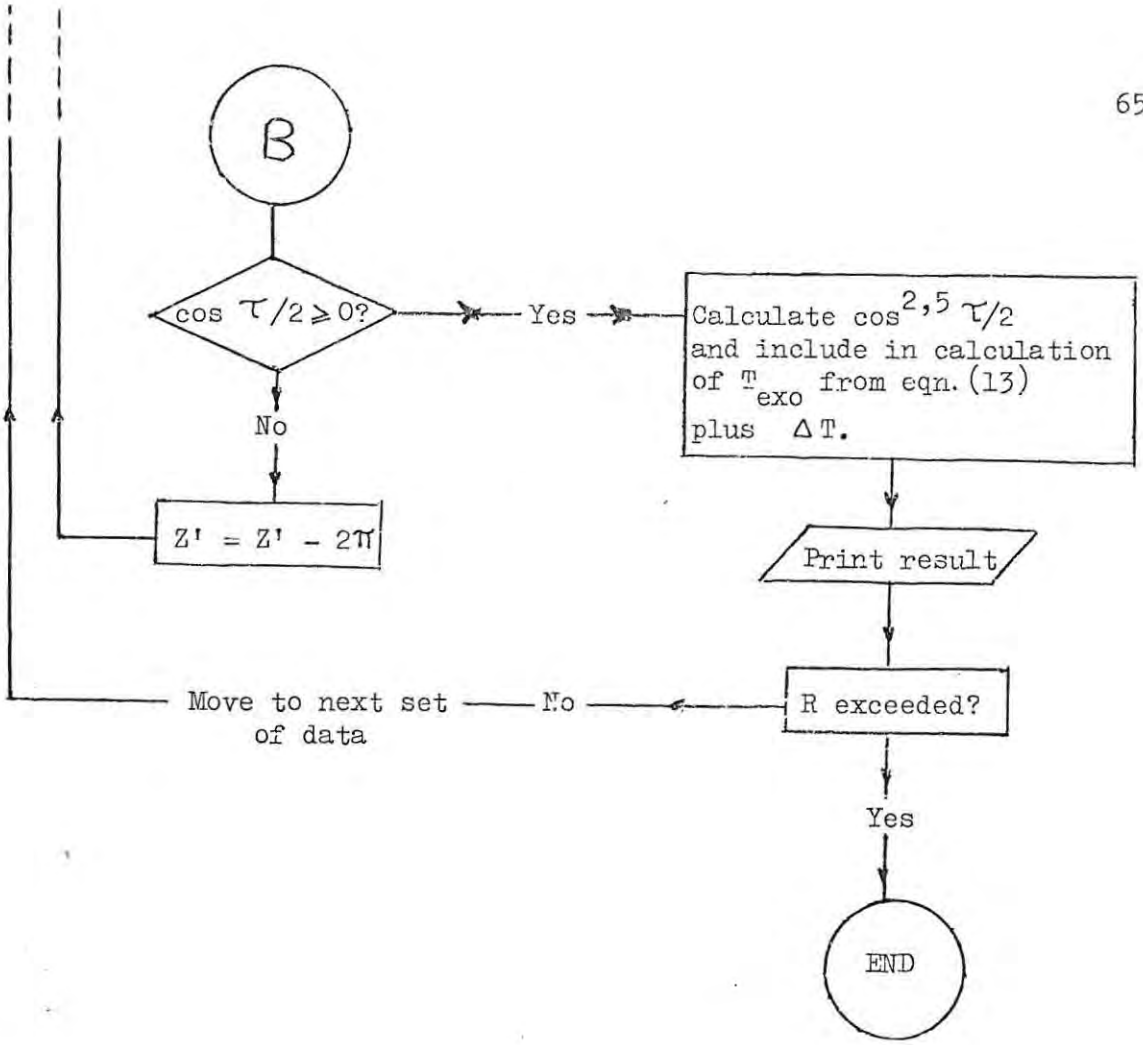
B
cos τ/2 ≥ 0?
Yes
Calculate cos^2,5 τ/2 and include in calculation of T_exo from eqn. (13) plus ΔT.
No
Z' = Z' - 2π
Print result
R exceeded?
No
Move to next set of data
Yes
END

APPENDIX 5

INTERATM

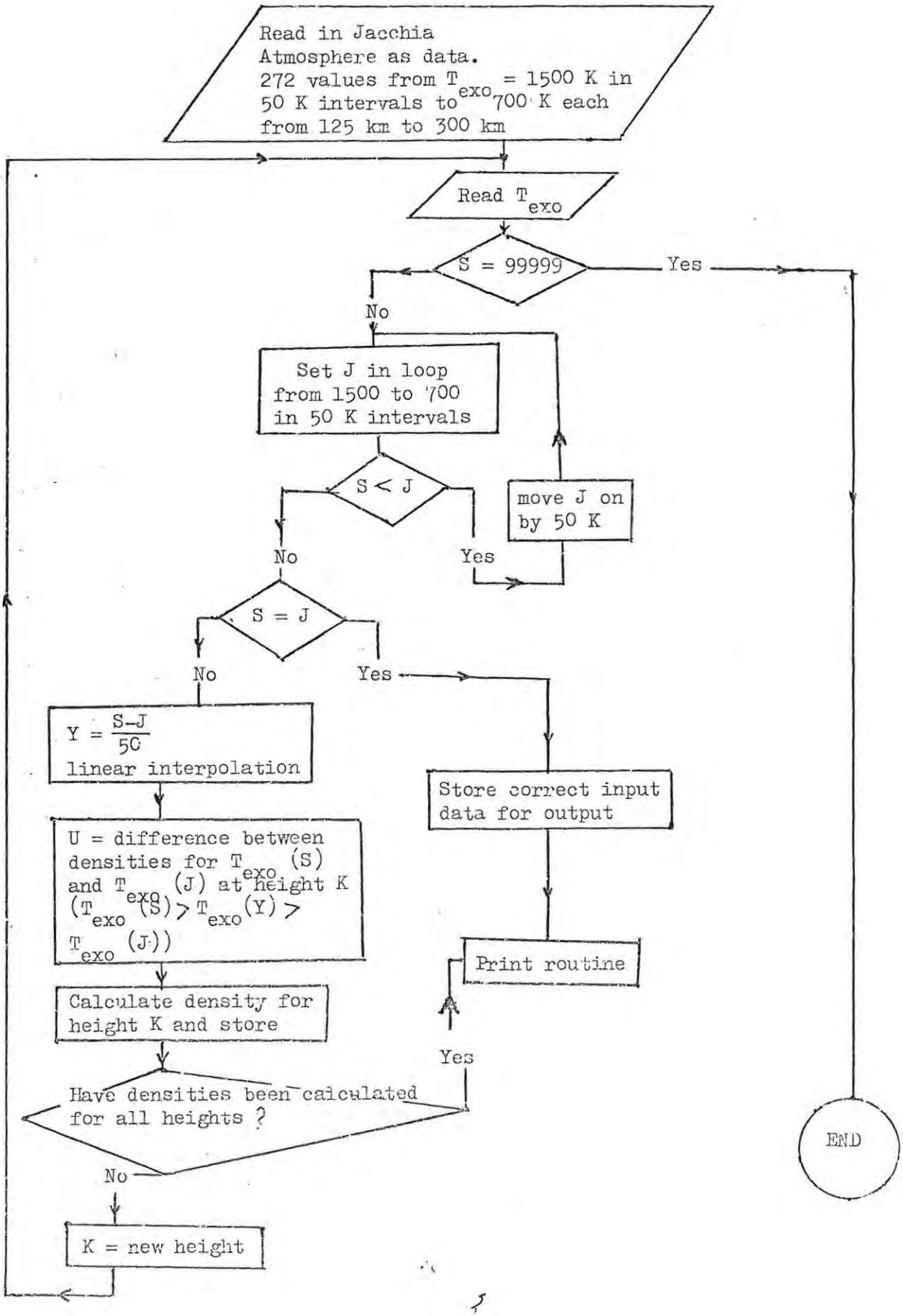

APPENDIX 6

Program MAXHQ

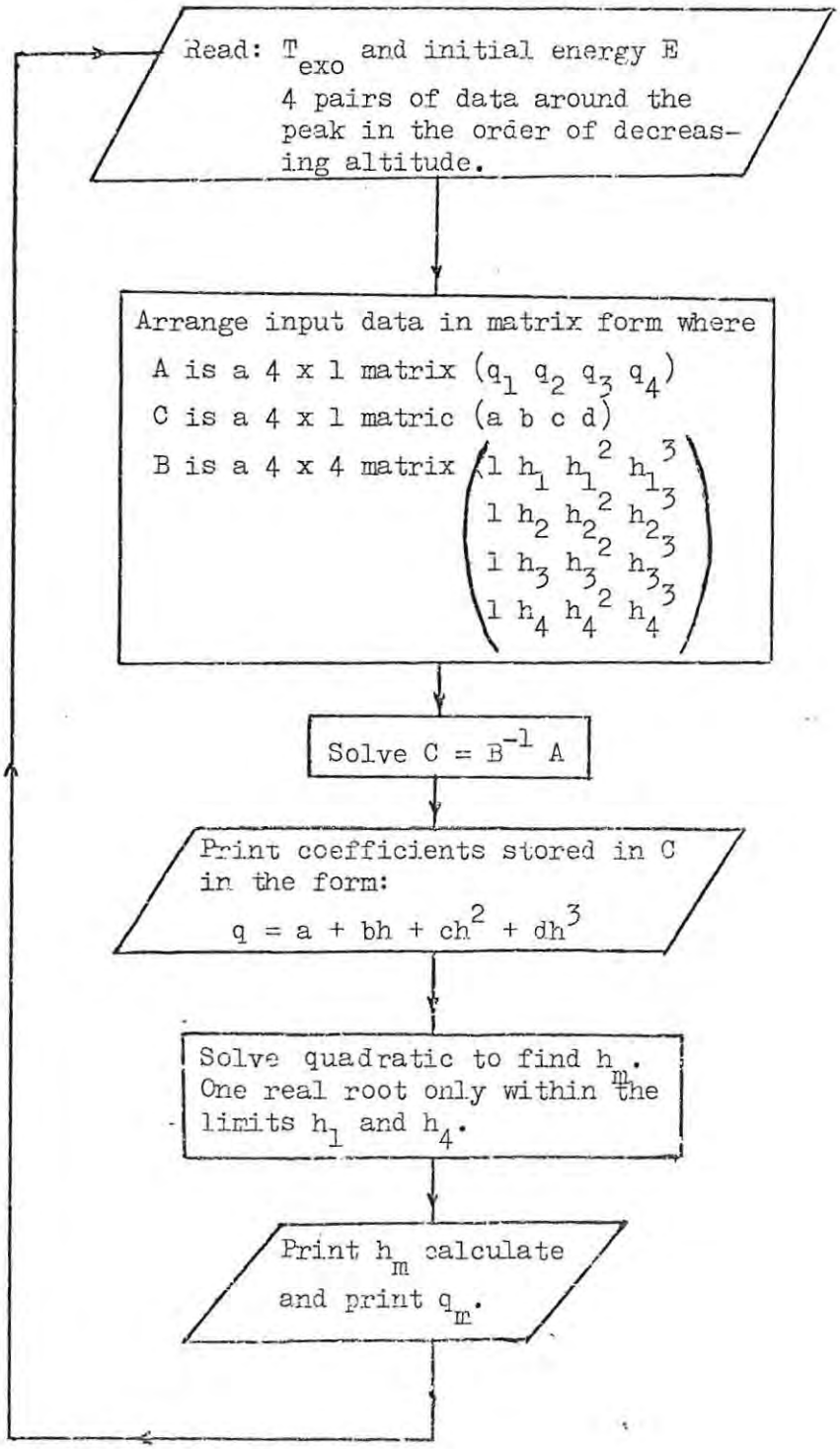

```
EQ=YQ-AQXQXQXQ-BQXQXQ-CQXQ
JUMP20,Q=N-1
14)REPEAT
Q=N
L=1
JUMP8
20)READ(R)                          END OF λ INTERPOLATION
READ(L)                             NUMBER OF DIFFERENT MODEL ATMOSPHERES
READ(N)                             L=1 (MONOENERGETIC) L=0 ENERGY SPECTRUM
READ(M)                             N = NUMBER OF LAMINATIONS
S=0                                 NUMBER OF INITIAL ENERGIES (≤8)
O=N
J=1(1)M
READ(UJ)
REPEAT
J=1(1)R
I=8(1)14
READ(UI)                            MODEL ATMOSPHERE SPECIFICATIONS
REPEAT
READ(H)                             DIP ANGLE I
READ(T)                             Texo
I=S(1)O
17)   READ(HI)                      ALTITUDE } MODEL ATMOSPHERE
READ(DI)                            DENSITY  }
REPEAT
K=1(1)M
E=UK
Y=H
JUMP45,L=1
SPACE46
PRINT('ENERGY FLUX J=J0 EXP(-E/E0)')
JUMP46
45)SPACE51
PRINT('MOMO ENERGETIC FLUX')
46)NEWLINE
SPACE50
PRINT('LAMBDA IDH UNIVERSAL')
NEWLINE
SPACE39
PRINT('RANGE: R=4.17&-6 EXP(1.74LOG(E))  (BSM IDH)')
NEWLINE
SPACE45
PRINT('JACCHIA/CIRA MODEL ATMOSPHERE')
PRINT('    T EXO:')
PRINT(T)4,0
NEWLINE
PRINT('HOUR ANGLE:')
PRINT(U8)3,0
PRINT('DEGREES    LATITUDE:')
PRINT(U9)2,2
PRINT('DEGREES    DECLINATION:')
PRINT(U10)2,2
PRINT('DEGREES    DAY:')
PRINT(U11)3,0
PRINT('    F10.8:')
PRINT(U12)3,1
NEWLINE
PRINT('    BARF10.8:')
PRINT(U13)3,1
PRINT('             AP: ')
PRINT(U14)2,0
NEWLINE2
SPACE18
```

```
PRINT(N)2,0
PRINT('LAMINATIONS      REF. ALTITUDE  300 KM      B AT 100  KM')
PRINT('    DIP AT GROUND')
PRINT(Y)2,2
PRINT('DEGREES')
      Y=%MOD(Y)
Y=(£Y)/180
Y=1/[%SIN(Y)]
NEWLINE
SPACE18
JUMP42,L=1
PRINT('  E-FOLDING ENERGY  ')
PRINT(E)2,1
A=E                              ! E-FOLDING ENERGY
G=10E                            ! E MAX
E'=1                                     ! E MIN
D=E'/100
E=E'+ 0.5D                               ! E
JUMP41
42)PRINT('INITIAL ENERGY')
PRINT(E)2,0
A=E
G=E
D=0
41)PRINT('KEV')
98)NEWLINE3
SPACE17
PRINT('ALTITUDE                Q/F              ENERGY LOSS(EV/CM)')
PRINT('      £Q/F=Q/J0(BAILEY)')
NEWLINE2
I=0(1)N
E(I+21)=0
REPEAT
10)W=4.17&-6%EXP(1.74%LOG(E))      RANGE-ENERGY RELATION (IDH)
X=(D/A)%EXP(-E/A)
JUMP48,X#0
X=1
48)F=0
I=N
11)JUMP12,I#N
ZI=0
VI=0
JUMP66,I=N
12)U=H(I+1)-HI
JUMP4,I=0
V=YU
U'=[D(I+1)-DI]/[%LOG(D(I+1)/DI)]
13)ZI=100000U'V
F=F+ZI
Z=F/W
JUMP4,F>W
Q=%INTPT(Z/.05)
VI=AQZZZ+BQZZ+CQZ+EQ
VI=(EVIDI)/(.035W)
E(I+21)=VIX+E(I+21)
66)I=I-1
JUMP12
4)D=E/100
E=E+D
JUMP50,E>=G
JUMP10
50)I=N(-1)0
15)SPACE20
```

```
AUTO=  LD↑
FI#XMAE#COMP↑
AUTO=  LD↑
GO21↑
LIST
RUN
DUMP ON (ED,PROGRAM DUMP)
SEND TO(ED,ICLA-DEFAULT.TUCKERS)
PROGRAM(AW18)
INPUT1=CR0
OUTPUT1=LP0
MAIN 600
CHAPTER0
H->42
D->42
Z->42
V->42
W->42
U->13
X->21
Y->20
F->20
G->20
A->20
B->20
C->20
E->75
L=0
I=0
1)READ(XI)                                  3/R
JUMP2,XI=99999
READ(YI)                                    λ(3/R)
I=I+1
JUMP1
2)N=I-2                                     START OF λ INTERPOLATION - POOLE PROGRAM
P=N-2
Q=0(1)P
JUMP5,Q#0
J=Q
JUMP6
5)J=Q+1
JUMP6,X(J+1)#XJ
16)HALT
6)FJ=[Y(J+1)-YJ]/[X(J+1)-XJ]
JUMP5,J=0
7)C'=X(Q/2)-XQ
JUMP5,J=0
C'=X(Q+2)-XQ
JUMP20,C'=0
A'=[F(Q+1)-FQ]/C'
B'=[FQ(X(Q+2)+X(Q+1))-F(Q+1)(XQ+X(Q+1))]/C'
JUMP3,Q#0
8)GQ=2A'XQ+B'
JUMP3,L#1
Q=N-1
JUMP9
27)HALT
3)G(Q+1)=2A'X(Q+1)+B'
9)D'=X(G+1)-XQ
D'=D'D'
AQ=[GQ+G(Q+1)-2FQ]/D'
BQ=-[(G(Q+1)+2GQ)X(Q+1)+(GQ+2G(Q+1))XQ-3(XQ+X(Q+1))FQ]/D'
CQ=[GQX(Q+1)(2XQ+X(Q+1))+G(Q+1)XQ(XQ+2X(Q+1))-6XQX(Q+1)FQ]/D'
```

```
PRINT(HI)3,0
SPACE10
PRINT(E(I+21))0,4
SPACE10
PRINT(35E(I+21))0,4
SPACE10
PRINT(E(I+21)£)0,4
NEWLINE
REPEAT
REPEAT
REPEAT
51)END
CLOSE
****
```

q/F ion pairs / el-cm

35 q/F eV / el-cm

q/Jo ion pairs / el-cm

A TYPICAL SET OF DATA

```
0  1.3  0.05  1.28  0.1  1.26  0.15  1.24  0.2  1.21  0.25  1.18  0.3  1.14
0.35  1.10  0.4  1.05  0.45  0.98  0.5  0.91  0.55  0.84  0.6  0.75
0.65  0.66  0.7  0.57  0.75  0.48  0.8  0.39  0.85  0.31  0.9  0.24
0.95  0.18  1.0  0.12  99999
4  0  42
5  2  5  20  50  100
0  -70.3  0  80  150  150  11
-62.6
900
90  3.01828-9  91  2.4954&-9  92  2.1395&-9  93  1.7121&-9  94  1.4252&-9
95  1.1896&-9  96  9.9474&-10  97  8.3368&-10  98  7.0129&-10  99  5.9135&-10
100  4.9925&-10  101  4.1727&-10  102  3.4991&-10  103  2.9509&-10
104  2.4960&-10  105  2.1219&-10  106  1.8117&-10  108  1.3324&-10
110  9.9147&-11  112  7.1432&-11  114  5.2905&-11  116  4.0119&-11
118  3.1134&-11  120  2.461&-11
125  .1656&-10  130  .8506&-11  135  .6258&-11  140  .4010&-11  145  .3110&-11
150  .2210&-11  155  .1773&-11  160  .1336&-11  165  .1097&-11  170  .8575&-12
175  .7158&-12  180  .5741&-12  190  .3964&-12  200  .2803&-12  220  .1477&-12
240  .8210&-13  260  .4752&-13  280  .2843&-13  300  .1749&-13
```